Prévision des niveaux d'eau dans l'estuaire et le golfe du Saint-Laurent en fonction des changements climatiques

Rapport final

Projet X011.1

Zhigang Xu, Chargé de projet et chercheur principal

et

Denis Lefaivre, chercheur associé

Institut des Sciences de la Mer
Université du Québec à Rimouski

Réalisé pour le compte du ministère des Transports du Québec

Le 31 janvier 2015

La présente étude a été réalisée à la demande du ministère des Transports du Québec et a été financée par la Direction de la recherche et de l'environnement dans le cadre du Plan d'action 2006-2012 sur les changements climatiques du gouvernement du Québec, Action 23C – volet érosion côtière. Les opinions exprimées dans le présent rapport n'engagent que la responsabilité de leurs auteurs et ne reflètent pas nécessairement les positions du ministère des Transports du Québec.

Équipe et Collaborateurs

- Zhigang Xu, Ph. D., professeur associé, Institut des sciences de la mer, Université du Québec à Rimouski et chercheur scientifique, Pêches et Océans Canada, Institut Maurice-Lamontagne.
- Denis Lefaivre, Ph. D., professeur associé, Institut des sciences de la mer, Université du Québec à Rimouski et chercheur scientifique, Pêches et Océans Canada, Institut Maurice-Lamontagne.
- Jean-Pierre Savard, M. Sc., spécialiste Impacts climatiques et Adaptation, Ouranos (collaborateur)

Référence suggérée

Xu, Z. et D. Lefaivre. Prévision des niveaux d'eau dans l'estuaire et le golfe du Saint-Laurent en fonction des changements climatiques. Rapport interne au Ministère des Transports du Québec, janvier 2015, 86 pp.

CHARGÉ DE PROJET AU MINISTÈRE DES TRANSPORTS DU QUÉBEC

Michel Michaud, géog., M.ATDR,

Chargé de projet, Conseiller en recherche

Service de la coordination de la recherche et de l'innovation

Direction de l'environnement et de la recherche

Ministère des Transports du Québec

930, chemin Ste-Foy, 6e étage

Québec (Québec) G1S 4X9

Téléphone : 418 644-0986 poste 4161

Télécopieur : 418 643-0345

Courriel : michel.michaud@mtq.gouv.qc.ca

COMITÉ DE SUIVI DU PROJET

- Michel Michaud, chargé de projet, direction de l’environnement et de la recherche, MTQ
- Christian Poirier, Ing. M. Sc., Chef du module hydraulique, Direction des structures, MTQ
- Daniel Lavallée, Ing., Service de la conception, MTQ
- Yann Ropars, Ing. M. Sc., Consultant
- Jean-Pierre Savard, M. Sc.. Océanographe, Ouranos

Table des matières

Résumé

Une base de données composée des séries temporelles de longue durée des valeurs d'onde de tempête, des marées et des niveaux d'eau totaux est par la présente, livrée au ministère des Transports du Québec pour un ensemble de points d'intérêt dans l'estuaire et le golfe du Saint-Laurent. Les ondes de tempête ont été produites d'une part par un champ réaliste de forçage atmosphérique et aussi par quelques champs stochastiques climatiques. Le forçage réaliste est fourni par MERRA, soit l'analyse atmosphérique rétrospective de l'ère actuelle pour la recherche et les applications produite par la NASA qui couvre la période de 1979 à 2011. Le forçage stochastique climatique a été produit par le Centre canadien de la modélisation et de l'analyse climatique sous la famille de solutions MRCC, Modèle régional canadien du climat, et par le modèle pour la recherche interdisciplinaire sur le climat, version 4 (MIROC4h), qui couvre différentes périodes depuis 1950 jusqu'à aussi loin que 2100. Cette base de données sera très utile pour des études statistiques pour évaluer les risques et les impacts liés aux impacts des niveaux d'eau sur la région côtière et les infrastructures de transport maritime. Les séries temporelles sont disponibles au MTQ sur demande en s'adressant au chef du module hydraulique.

Ce rapport décrit également une nouvelle méthode, la technique de la fonction de Green pour toutes sources (ASGF, All-Source Green Fonction), qui rend possible la simulation des ondes de tempête pour de longues périodes et avec des champs multiples de forçage. Un exemple est également donné sur la façon d'utiliser statistiquement les séries temporelles de niveau d'eau avec la théorie des valeurs extrêmes de Gumble pour permettre de valider les changements dans les périodes de tempête de retour des ondes de tempête.

Préface

Préoccupé par les impacts possibles des changements climatiques sur les infrastructures portuaires et côtières, le ministère des Transports du Québec (MTQ) a financé un projet de recherche sur la modélisation des ondes de tempête et des niveaux d'eau totaux sur un horizon climatique pour un ensemble de points de leur intérêt. Les livrables du projet sont les séries temporelles d'ondes de tempêtes, passées et futures, pour la période 1950 à 2100, ainsi que les prédictions de marée pour la même période. Ces séries sont d'intérêt parce qu'elles fournissent une base de données pour des études statistiques pour évaluer les impacts dus au changement climatique.

Ce rapport décrit comment ces séries temporelles de niveau d'eau sont produites. Nous présentons à la suite du rapportune documentation en appui au rapport. Il s'agit de textes qui ont été acceptés pour publication mais sujet à des révisions mineures. Les détails d'une nouvelle méthode utilisée pour produire efficacement de longues séries temporelles d'onde de tempête sont présentés en 2.1 et en 2.2 par Z. Xu. La nouvelle méthode, appelée la technique de la fonction de Green pour toutes sources (ASGF, All-Source Green Fonction), permet de produire des séries longues d'un siècle. Une méthode statistique d'analyse des séries temporelles de niveau d'eau est illustrée en 2.3 par Z. Xu, J.-P. Savard et D. Lefaivre. Il y a plusieurs façons d'effectuer une analyse statistique des séries temporelles. Notre approche consiste à utiliser l'analyse des valeurs extrêmes de Gumbel (EVA) pour ces séries temporelles, pour identifier s'il y a des changements dans les périodes de retour des ondes de tempête pour le prochain siècle. Cette documentation en appui au rapport permet aux lecteurs de ce rapport (et à leurs auteurs) une manière commode de référer l'un à l'autre.

Zhigang Xu
Institut Maurice-Lamontagne
Pêches et Océans Canada
et
Institut des sciences de la mer
Université du Québec à Rimouski

zhigang.xu@dfo-mpo.gc.ca

Denis Lefaivre
Institut Maurice-Lamontagne
Pêches et Océans Canada
et
Institut des sciences de la mer
Université du Québec à Rimouski

denis.lefaivre@dfo-mpo.gc.ca

1 Modélisation des ondes de tempête dans l'estuaire et le golfe du Saint-Laurent en reproduction historique et en fonction des changements climatiques

Zhigang Xu et Denis Lefaivre

Pêches et Océans Canada, Institut Maurice-Lamontagne.

et

Institut des Sciences de la mer
Université du Québec à Rimouski

Le 31 janvier 2015

1.1 Introduction

C'est le chapitre principal de ce rapport. Les autres chapitres sont auxiliaires à celui-ci pour décrire succinctement comment produire le calcul d'onde de tempête pour des séries temporelles sur de longues périodes à un ensemble de points d'intérêt (POI). Dans la section 1.2, nous allons d'abord décrire les champs atmosphériques utilisés pour calculer les ondes de tempête. A la section 1.3, nous décrirons ensuite comment produire les simulations d'ondes de tempête avec ces forçages sur une période d'un siècle, et comment produire les simulations de marées. A la section 1.4, nous présenterons l'utilisation des références verticales et comment intégrer les marées aux ondes de tempête pour obtenir les niveaux d'eau totaux dans le référentiel vertical voulu. Il y a deux annexes à ce chapitre, qui donnent plus de détails sur certains aspects. La position des POI identifiés par le MTQ est illustrée à la figure 1-1 et reprise dans le tableau 1-2 de l'annexe B du présent chapitre.

Ajouter les numéros de station selon la liste du Tableau 1.2

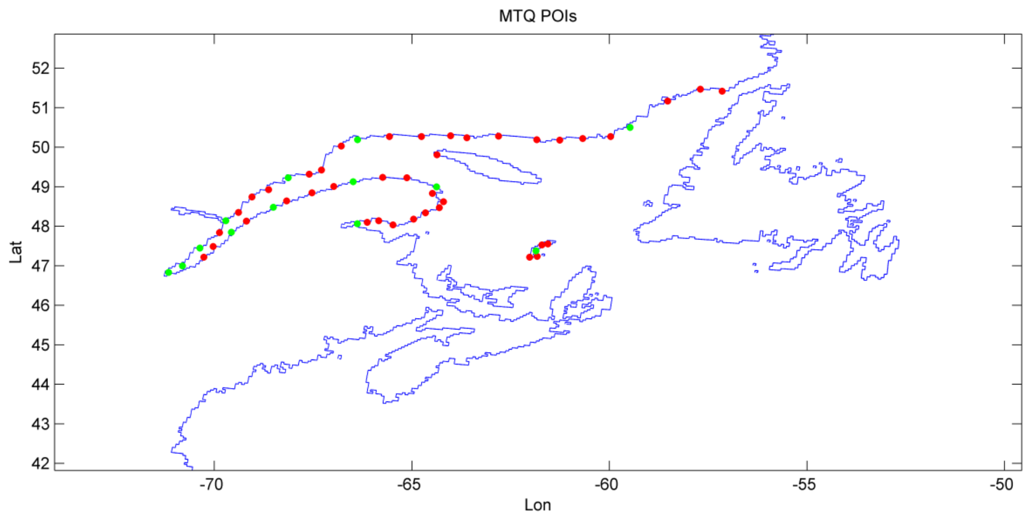

Figure 1-1 Les points d'intérêt (POI) identifiés par le MTQ. Les points verts indiquent où des observations sont disponibles et utilisées.

1.2 Le forçage atmosphérique

Nous utilisons les résultats d'un modèle atmosphérique comme forçage pour entraîner notre modèle d'onde de tempête. Plus précisément, nous utilisons la pression atmosphérique au niveau de la mer et les composantes U et V du vent à 10 mètres au-dessus du niveau moyen des mers comme champ de forçage, (voir les équations 2-2 et 2-3 du chapitre 2). Le champ de forçage peut être classé comme réaliste ou stochastique, selon les résultats du modèle atmosphérique utilisé. Par réaliste, nous voulons dire que nous reproduisons un état passé. Par stochastique, nous entendons que le champ atmosphérique ne reproduit pas le passé mais conserve ses attributs statistiques tels que la fréquence et l'intensité des tempêtes sans qu'elles ne se produisent précisément au même moment que dans la réalité. Les résultats d'un modèle atmosphérique en réanalyse comme MERRA et GEM sont réalistes car ils assimilent les observations passées. Ils peuvent en effet bien prévoir la météorologie pour les prochains jours. Les résultats d'un modèle climatique sont stochastiques. Une fois lancé, un modèle climatique n'assimile pas d'observations même si sa période de calcul couvre le passé et où des observations sont disponibles. Les résultats de modèles stochastiques sont utiles parce qu'ils fournissent une base pour des analyses statistiques des résultats. Plus grand est le nombre de modèles stochastiques utilisés, plus robustes sont les analyses statistiques qui en découlent. C'est pourquoi un ensemble de résultats de modèles climatiques multi-membres est souhaitable.

Pour notre champ de forçage réaliste, nous avons choisi les résultats du modèle atmosphérique MERRA. L'acronyme MERRA représente Modern-Era Retrospective Analysis for Research and Applications, soit l'analyse atmosphérique rétrospective de l'ère actuelle pour la recherche et les applications. Cette analyse est produite sous la gouverne de la NASA et est disponible au site web suivant : http://gmao.gsfc.nasa.gov/merra/. C'est un ensemble de données de réaanalyse atmosphérique qui utilise le système d'assimilation de données globales de la NASA et d'une variété de systèmes d'observation autour du globe. Il est destiné à fournir à la communauté scientifique et publique un ensemble global de données à la pointe de la recherche. Sa résolution temporelle est d'une heure avec une résolution spatiale est de 0,5 degrés. Son domaine temporel couvre les années 1979 à nos jours. En raison des différentes étapes de téléchargement de données et de leur traitement, nous utilisons les données jusqu'au 31 décembre 2011 pour ce projet.

Pour le forçage stochastique du climat, nous utilisons les résultats de quatre modèles climatiques. Ils sont présentés au tableau 1-1 La famille des modèles MRCC proviennent du Modèle Régional Canadien du Climat. Ce sont des solutions régionales. Le domaine du MRCC est présenté à la figure 1-2.

Nom	**Résolution spatiale et couverture**	**Résolution temporelle et période**	**Source**	**Réaliste ou stochastique**
MERRA	0.50 deg. en latitude, 0.67 deg. en longitude, global	Horaire, du 25 juillet 1971 à nos jours	NASA/JPL	Réaliste
MRCC/AEV	45 km (~0.4 deg), régional	Aux 3 heures, 1961-2100	EC[1] et OURANOS[2]	Stochastique
MRCC/AHJ	45 km (~0.4 deg), régional	Aux 3 heures, 1961-2100	EC et OURANOS	Stochastique
MRCC/AJL	45 km (~0.4 deg), régional	Horaire, 1961-2070	EC and OURANOS	Stochastique
MIROC4H	0.56 deg, global	Aux 3 heures, 1950-2035	Japon	Stochastique

Tableau 1-1 Caractéristiques des modèles atmosphériques utilisés comme forçage atmosphérique pour le calcul des ondes de tempête.

[1] EC: Environnement Canada
[2] OURANOS: Consortium sur la climatologie régionale et l'adaptation aux changements climatiques

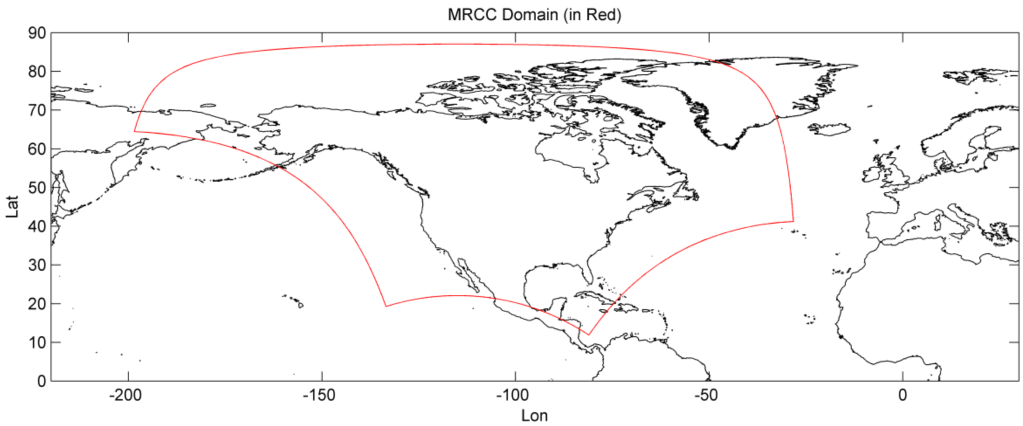

Figure 1-2 Le contour en rouge indique le domaine du modèle climatique MRCC.

1.3 La modélisation des ondes de tempête et des marées

1.3.1 Reproduction historique des ondes de tempête

D'un modèle global des ondes de tempête, Xu (2014b) a écrit une relation linéaire simple et précise mais très efficace entre le forçage global en entrée et la réponse en niveau d'eau local, tel qu'indiqué dans l'équation 3-14, reprise ici en Eq. 1-1 par commodité,

$$\boldsymbol{\eta} = \mathbf{C}\,\mathbf{s} \qquad (1\text{-}1)$$

où **C** est une matrice qui représente en données d'entrée le forçage atmosphérique global, **s** est un vecteur de paramètres spécifiés inhérents à la physique du modèle d'onde de tempête, $\boldsymbol{\eta}$ représente la réponse en série temporelle des niveaux d'eau à un POI. Cette relation linéaire simple est issue d'un modèle numérique traditionnel beaucoup plus complexe tel que décrit par l'équation (2-1), et est basée sur la technique de la fonction de Green pour toutes sources (ASGF, All-Source Green Fonction) (Xu, 2007; Xu 2011) . Le résultat de l'équation (1-1) est identique à la sortie de l'Eq. (2-1) aux POI à toutes fins pratiques, mais le premier est des millions de fois plus efficace que le second. Il existe plusieurs facteurs qui contribuent à une telle amélioration de l'efficacité, tel que décrit dans Xu 2014a et Xu 2014b. La principale raison est que l'équation (1-1) calcule la réponse en un seul point alors que l'Eq. (2-1) calcule la réponse à tous les points de la grille du modèle, même si le résultat n'est pas d'intérêt pour nous. Les liens dynamiques entre les POI et le reste de l'océan global ont été pré-calculés, et imbriqués dans la matrice **C** et le vecteur **s**. Une telle augmentation d'efficacité rend possible la simulation d'ondes de tempête sur un siècle.

En introduisant un terme d'erreur pour tenir compte du bruit dans le calcul et des imperfections du modèle d'onde de tempête, Xu 2014b, Eq. (3-15), a repris l'équation linéaire précédente pour en faire un modèle de régression, Eq. (1-2),

$$\boldsymbol{\eta} = \mathbf{C}\,\mathbf{s} + \boldsymbol{\varepsilon} \qquad (1\text{-}2)$$

dans lequel $\boldsymbol{\varepsilon}$ représente le terme d'erreur. Le vecteur **s** doit maintenant être considéré comme un vecteur contenant les paramètres de régression à être déterminé par l'ajustement optimal entre les données et le modèle. Ce modèle de régression linéaire nous fournit un outil pour effectuer des simulations d'ondes de tempête avec assimilation de données d'observation.

Xu (2014b) a donné un exemple où les deux solutions ont été comparées soit sans assimilation de données selon l'Eq. (1-1) et avec assimilation de données selon l'Eq. (1-2) à un cas réel d'onde de tempête survenue en décembre 2010. L'inadéquation entre les observations et les résultats du modèle sans assimilation de données est 0.18 tel qu'évalué par le paramètre γ^2 défini par l'Eq. (2-96). L'inadéquation entre les observations et les résultats du modèle avec assimilation de données n'est plus que de 0.05. Xu et al (2014) a démontré comment l'équation (1-2) a été utilisée pour assimiler de longues séries de données autant en reproduction historique qu'en prévision climatologique des ondes de tempête à Sept-Îles dans le golfe du Saint-Laurent. A la figure (4-5) est présentée la série temporelle de la reproduction historique 1979-2011 avec assimilation de données et de la prévision climatologique de 1950 à 2100. Toutes les séries temporelles des ondes de tempête produites dans le cadre de ce projet pour les autres POI ont été générées de la même manière.

L'équation Eq. (1-2) implique que des données d'observation sont nécessaires pour contraindre le vecteur des paramètres de régression ε. Cependant, comme illustré à la figue (1-1), il n'y a pas d'observations à tous les POI. Il n'y a pas d'observations aux points indiqués en rouge. Pour résoudre ce problème, nous avons eu recours à un modèle d'onde de tempête non linéaire, dont les équations sont décrites à l'annexe A du présent chapitre, pour produire des résultats pour une année complète utilisés comme "données" tel que requis par le modèle de régression. Le domaine du modèle non linéaire couvre l'ensemble du golfe du Saint-Laurent. Les conditions frontières aux limites océaniques, soit au détroit de Cabot et au détroit de Belle-Île ont été calculées à l'aide de la méthode ASGF. Nous avons utilisé le modèle non linéaire pour fournir les «données» au modèle linéaire, parce que généralement le premier est réputé donner de meilleures solutions que le deuxième. Cependant, pour exécuter le premier cela demande beaucoup plus de temps de calcul que d'exécuter le modèle linéaire. En conséquence, nous utilisons les résultats des modèles non-linéaire et linéaire ensemble pour produire des séries temporelles de niveau d'eau en reproduction historique sur de longues périodes.

1.3.2 Simulation des ondes de tempête en changement climatique

Avec l'assimilation des données, nous avons non seulement la reproduction historique des ondes de tempête, mais avons aussi obtenu le vecteur des paramètres de régression le plus adéquat pour la modélisation avec le forçage atmosphérique futur. Celui-ci correspond aux les quatre champs de forçages climatiques stochastiques énumérés dans le tableau 1-1. Les détails sur la méthode d'utilisation de ces forçages avec le modèle de régression de l'équation 1-2 pour effectuer une prévision climatologique sont documentés au chapitre 4, où le membre MRCC/AHJ est utilisé à titre d'exemple pour démontrer comment la série temporelle des ondes de tempête peut être générée de manière très efficace pour la période allant jusqu'à l'an 2100. Ce chapitre traite également des biais systématiques dans les ondes de tempête en raison d'un forçage climatique trop fort et propose un moyen de corriger ces biais à l'aide de la méthode d'analyse des valeurs extrêmes (EVA).

1.3.3 Modélisation des marées

La modélisation des marées est basée sur l'analyse harmonique. Pour les stations où il y a des observations, nous appliquons l'analyse harmonique des données pour obtenir un ensemble de constantes harmoniques de marée, puis nous les utilisons pour produire des séries temporelles de marée pour la période de 1979 à 2011. Pour les POI où il n'y a pas d'observation, nous prenons une station qui est tout près de la position désirée. S'il n'y en a pas, nous avons recours aux résultats d'un modèle de marée non linéaire pour l'ensemble du golfe du Saint-Laurent (Saucier et al 2000; 2003) pour obtenir une année complète de données, puis nous utilisons l'analyse harmonique sur cette série temporelle (tel qu'indiqué au Tableau 1-2). Le modèle est entraîné par les marées aux frontières ouvertes des détroits de Cabot et de Belle-Isle, et par le débit d'eau douce à Québec. Le niveau d'eau horaire à tous les points de la grille de 5 km pour 2006 a été utilisé.

1.4 Repère vertical et niveau d'eau total

Avec l'utilisation des séries temporelles des niveaux d'eau, il faut être conscient qu'on doit tenir compte de trois références verticales. Elles sont représentées à la Figure 1-3.

- CGVD28: Niveau moyen des mers dans le référentiel géodésique canadien de référence altimétrique 1928, qui est la référence verticale adoptée par le gouvernement du Canada pour les applications terrestres (topographiques)[3].
- Le zéro des cartes, ZC: C'est le niveau le plus bas de la marée basse, défini comme la moyenne sur 19 ans des plus faibles marées annuelles prédites, telles que présentées dans les Tables de Marées du Service hydrographique du Canada. Il fournit une référence verticale pour la profondeur indiquée sur les cartes marines et la hauteur des marées [4]. Le zéro des cartes, ZC, peut être défini en référence au système CGVD28. Chaque station marégraphique a sa propre valeur du ZC, comme indiqué à la 7e colonne du tableau 1-2 du présent chapitre. Il y a quelques stations où les valeurs du ZC sont en rouge, ce qui signifie que ces valeurs sont interpolées à partir des stations à proximité.
- Niveau moyen des mers, Z0: C'est le niveau moyen de l'eau de la prédiction de marée sur la période d'observation disponible, référencé au zéro des cartes. Chaque station a sa propre valeur de Z0, tel qu'affiché au Tableau 1-2.

Les valeurs d'ondes de tempête sont fournies par rapport au niveau moyen des mers ($z = 0$, sur la figure 1-3). Les prédictions de marée sont données par rapport au zéro des cartes locales. Le niveau d'eau total, soit la somme des ondes de tempête et des marées est également donné par rapport au zéro des cartes locales. Pour transférer les données de marées et les niveaux d'eau totaux dans le référentiel du CGVD28, il faut simplement ajouter l'écart avec le ZC indiqué à la 7[e] colonne du Tableau 1-2. Pour transférer les données des ondes de tempête seules dans le référentiel du CGVD28, il faut utiliser l'équation suivante:

$$\eta_{CGVD28} = \eta + Z0 + CD \qquad (1\text{-}3)$$

où η_{cgvd28} est l'onde de tempête dans le référentiel CGVD28, η est l'onde de tempête au niveau moyen des mers, Z0 et CD ont été définis plus haut.

[3] http://www.rncan.gc.ca/sciences-terre/geomatique/systemes-reference-geodesique/9053

[4] http://waterlevels.gc.ca/eng/info/verticaldatums

Finalement, pour les stations où la différence entre le CGVD28 et les niveaux de référence: zéro des cartes et ligne des hautes eaux, n'est pas connue, une interpolation linéaire entre les stations voisines a été effectuée.

La station Baie-des-Moutons n'a pu être référencée au CGVD28 faute de voisins immédiats. Il n'y a donc pas de résultats pour cette station.

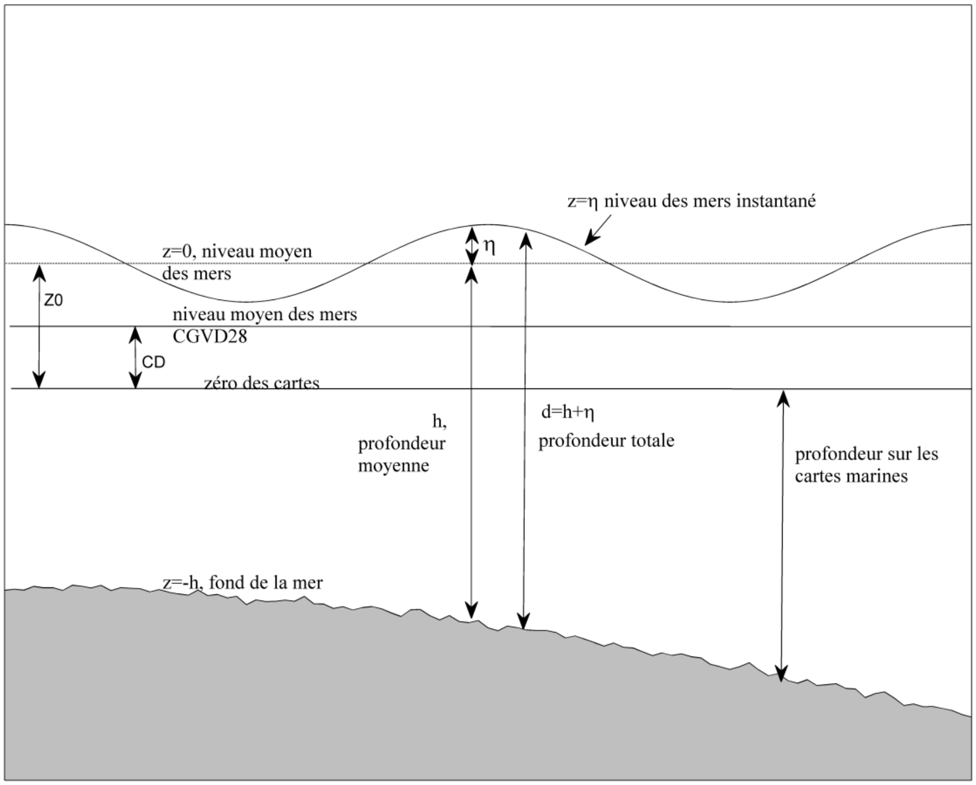

Figure 1-3. Représentation schématique des références verticales utilisées.

1.5 Livrables

Le tableau 1-2 donne la liste des 60 stations où on peut suivre les liens vers les livrables. La troisième colonne du tableau contient les liens vers la série temporelle correspondante à la station de la reproduction historique réaliste (marées, les ondes de tempête et les niveaux d'eau totaux). La dernière colonne contient les liens vers la série temporelle stochastique climatique. Certaines stations ont été remplacés par la station la plus proche en raison d'absence d'observations, tel qu'indiqué dans la dernière section du tableau. Dans l'avant dernière colonne du tableau, le «oui» en noir indique qu'il y a un an d'observations, le «oui» en rouge signifie qu'il y a une courte série d’observations, et le "mo" en rouge indique que nous avons utilisé les résultats du modèle opérationnel de marée. Au tableau 1-2, les valeurs de ZC et de LHE en rouge indiquent qu'elles ont interpolées à partir des stations à proximité.

Les ondes de tempête climatologiques stochastiques ont été entraînées par trois forçages climatiques, MRCC-AHJ, MRCC_AEV et MIROC4H. Les forçages du MRCC couvrent la période 1961-2100 et le MIROC4H couvre la période 1950-2035. Les solutions réalistes proviennent du forçage MERRA et couvrent la période 1979-2011.

En cliquant sur un des liens, votre navigateur Web ouvre un fichier texte. Pour éviter que le même enregistrement s’étende sur deux lignes de votre écran, vous pourriez avoir besoin d'ajuster la taille de la police. Chaque fichier contient un en-tête suivi des données. L'en-tête contient l’information sur la station et indique le contenu des colonnes du champ de données. Un exemple d’en-tête est présenté ci-dessous.

```
% Station Name: Sept-Iles; Station ID: 2780
% Longitude and Latitude (deg.): -66.38, 50.19
% Start and End Times (UTC): 1979-07-28 00:00:00,  2011-12-31 23:00:00
% Number of Records: 284280
% Missing Data Flag: NaN
% Time System: UTC (GMT); Water Level Units: meters
% Authors: Zhigang Xu and Denis Lefaivre (ISMER/UQAR)
% Email: zhigang.xu@dfo-mpo.gc.ca
%        denis.lefaivre@dfo-mpo.gc.ca
%
% Data Column Heading Symbols:
%     Y = year; M = month; D = day; H = hour
%     OTotal = Observed Total Water Level (m, CD)
%            (m, CD): in meters and referenced to Chart Datum
%     Tide = Tides(m, CD)
%     Resid = Residual Water Level (OTotal-Tide) (m)
%     Nlin  = Surge Simulated by A Non-Linear Model
%             (where there is no observation)
%
%     DASurge = Data Assimilative Surges (m)
%     STotal = Simulated Total Water Level (Tide+DASurge, m, CD)
%
%---- Data Start from here ----
% Y   M  D  H   OTotal   Tide     Resid    Nlin    DASurge   STotal
1979  7 28  0      NaN   1.3003      NaN      NaN   0.1429   1.4432
1979  7 28  1      NaN   0.8695      NaN      NaN   0.1245   0.9940
1979  7 28  2      NaN   0.5864      NaN      NaN   0.1133   0.6997
```

1.6 Remerciements

Le ministère des Transports du Québec a financé cette étude. Nous avons également bénéficié des collaborations avec des membres du consortium Ouranos. Le libre accès aux données MERRA produites par la NASA est également très apprécié. Les auteurs tiennent également à remercier sincèrement l'appui de Pêches et Océans Canada et de l'UQAR / ISMER, en particulier le Service hydrographique du Canada, en la personne de M. André Godin. Nos remerciements vont également à messieurs Michel Beaulieu et Alain D'Astous pour leur aide à différentes étapes du projet.

1.7 Annexe A: Le système d'équations de Navier–Stokes qui gouvernent les ondes de tempêtes

Nous utilisons les équations suivantes pour modéliser les ondes de tempête:

$$\frac{\partial \eta}{\partial t} = -\frac{\partial ud}{\partial x} - \frac{\partial vd}{\partial y} \tag{1-4}$$

$$\frac{\partial ud}{\partial t} = -gd\frac{\partial(\eta+\eta_a)}{\partial x} + fvd + \tau_x^s - \tau_x^b - \frac{\partial uud}{\partial x} - \frac{\partial vud}{\partial y} \tag{1-5}$$

$$\frac{\partial vd}{\partial t} = -gd\frac{\partial(\eta+\eta_a)}{\partial y} - fud + \tau_y^s - \tau_y^b - \frac{\partial uvd}{\partial x} - \frac{\partial vvd}{\partial y} \tag{1-6}$$

où

η			perturbation de surface de la mer par rapport au niveau moyen des mers.	
(u,v)			la valeur moyenne sur la colonne d'eau des composantes de vitesse dans les directions est et nord.	
d	=	$h+\eta$	la profondeur totale de l'eau, où h est la hauteur d'eau mesurée du fond marin au niveau moyen des mers. Voir la figure 1-3.	(1-7)
(τ_x^b, τ_y^b)	=	$\kappa(u,v)$	le coefficient de friction au fond, où κ est soit quadrique ou linéaire, (voir la ligne suivante).	(1-8)
κ	=	$\begin{cases} \dfrac{g\mathcal{N}^2\sqrt{u^2+v^2}}{h^{1/3}} \\ \dfrac{g\mathcal{N}^2\lvert w\rvert}{h^{1/3}} \end{cases}$	le coefficient de friction quadrique au fond, où $\mathcal{N}$ est la rugosité de Manning; le coefficient de friction linéaire au fond, et $\lvert w\rvert$ est une vitesse de courant minimale estimée, avec comme valeur de 0.1m / s pour un courant de marée typique.	(1-9)
η_a	=	$\dfrac{P_{air}}{\rho g}$	le forçage induit par la pression atmosphérique (connu également sous le nom d'effet baromètre inverse).	(1-10)
(τ_x^s, τ_y^s)	=	$C_d\sqrt{U^2+V^2}(U,V)$	Stress du vent au niveau moyen des mers, où (U, V) sont les composantes de la vitesse du vent dans les directions est et nord, à 10 mètres au-dessus du niveau moyen des mers, où Cd est le coefficient de traînée (voir Eq. 2-4).	(1-11)
g			l'accélération terrestre.	
f	=	$2\Omega\sin\phi$	le paramètre de coriolis, où Ω est la période de rotation de la terre et ϕ la latitude.	(1-12)
(x,y)	=	$R(\lambda\cos\phi, \phi)$	la longueur de l'arc le long des cercles de latitude et de longitude avec R = 6371 km pour le rayon moyen de la Terre (rayon volumétrique de la terre, Moritz 2000), et λ la longitude.	(1-13)
t			le temps.	

Les unités du système international (SI) sont utilisées dans le système ci-dessus (avec la longueur en mètre, la masse en kilogramme et le temps en seconde).

1.8 Annexe B: Liste des stations et des séries temporelles

Station #	No Station SHC	Nom de la station	Lat. (deg)	Long. (deg)	Z0 en ZC (m)	ZC en CGVD28 (m)	Observations	Onde de tempête climatique
		Rive-sud et Gaspésie						
1	3250	Québec (Lauzon)	46.830	-71.160	2.56	-1.96	yes	yes
2	3100	Saint-François I.O.	47.000	-70.810	2.87	-2.52	yes	yes
3	3170	Saint-Jean-Port-Joli	47.220	-70.270	2.97	-2.69	yes	yes
4	3160	Pointe-aux-Orignaux	47.490	-70.030	3.27	-3.01	yes	yes
5	3130	Rivière-du-Loup	47.850	-69.570	2.60	-2.64	yes	yes
6	3005	Trois-Pistoles	48.130	-69.190	2.37	-2.39	yes	yes
7	2985	Rimouski	48.480	-68.510	2.25	-2.28	yes	yes
8	2975	I.M.L.	48.640	-68.170	2.11	-2.16	yes	yes
9	2955	Matane	48.850	-67.530	1.97	-1.97	yes	yes
10	2945	Gros-Méchins	49.010	-66.980	1.76	-1.78	yes	yes
11	2935	Sainte-Anne-des-Monts	49.130	-66.490	1.65	-1.66	yes	yes
12	2920	Mont-Louis	49.240	-65.740	1.46	-1.42	yes	yes
13	2350	Grande-Vallée	49.230	-65.130	1.29	-1.22	yes	yes
14	2330	Rivière-au-Renard	49.000	-64.380	1.01	-0.99	yes	yes
15	2320	Gaspé	48.833	-64.483	0.96	-0.91	yes	yes
16	2309	Mal-Bay	48.620	-64.200	0.86	-0.76	yes	yes
17	2295	Anse-à-Beaufils	48.472	-64.308	0.62	-0.71	mo	yes
18	2269	Chandler	48.342	-64.657	0.69	-0.76	mo	yes
19	2250	Port Daniel	48.180	-64.960	0.86	-0.73	yes	yes
20	2230	Havre-de-Beaubassin	48.038	-65.481	1.05	-0.94	yes	yes
21	2215	Pointe Howatson	48.140	-65.840	1.16	-1.15	yes	yes
22	2200	Carleton	48.100	-66.130	1.15	-1.13	yes	yes
23	2165	Dalhousie	48.067	-66.383	1.59	-1.48	yes	yes
		Rive-nord et Haute-Côte-Nord						
24	3057	Saint-Joseph-de-la-Rive	47.450	-70.370	3.36	-3.37	yes	yes
25	3030	Saint-Siméon	47.840	-69.870	2.88	-2.89	yes	yes
26	3425	Tadoussac	48.140	-69.710	2.31	-2.39	yes	yes
27	2900	Les Escoumins	48.350	-69.390	2.23	-2.27	yes	yes
28	2880	Forestville	48.740	-69.050	2.17	-2.15	yes	yes
29	2860	Betsiamites	48.930	-68.630	2.23	-2.00	mo	yes
30	2840	Baie-Comeau	49.230	-68.130	1.78	-1.81	yes	yes
31	2826	Godbout	49.320	-67.600	1.83	-1.76	yes	yes
32	2815	Baie-Trinité	49.423	-67.290	1.89	-1.67	mo	yes
33	2790	Port-Cartier	50.030	-66.790	1.51	-1.48	yes	yes
34	2780	Sept-Iles	50.190	-66.380	1.56	-1.46	yes	yes
35	NaN	Rivière-Pigou	50.270	-65.570	0.84	-1.29	mo	yes
36	2750	Rivière-au-tonnerre	50.270	-64.760	1.25	-1.11	yes	yes
		Basse-Côte-Nord						

37	2470	Mingan	50.290	-64.020	1.13	-1.03	yes	yes
38	2480	Havre St-Pierre	50.240	-63.610	0.96	-0.87	yes	yes
39	2490	Baie Johan-Beetz	50.280	-62.810	0.93	-0.91	yes	yes
40	2510	Natashquan	50.190	-61.840	0.84	-0.97	yes	yes
41	2518	Kegashka	50.180	-61.260	0.96	-1.00	yes	yes
42	2530	Gethsémani	50.220	-60.680	0.97	-1.03	yes	yes
43		Étamamiou	50.270	-59.970	1.21	-1.09	mo	yes
44	2550	Harrington Harbour	50.500	-59.480	1.03	-1.16	yes	yes
45	2564	St-Augustin	51.170	-58.530	1.06	-1.13	yes	yes
46	2579	Riv. St-Paul	51.471	-57.702	1.32	-0.97	mo	yes
47	2588	Blanc-Sablon	51.420	-57.150	1.01	-1.01	yes	yes
		Anticosti						
48	2360	Port Ménier	49.810	-64.370	1.02	-0.97	yes	yes
		Iles-de-la-Madeleine						
49	1970	Cap-aux-Meules	47.380	-61.860	0.83	-0.77	yes	yes
50	1964	Havre-Aubert	47.240	-61.830	0.69	-0.62	yes	yes
51	1985	Grande-Entrée	47.556	-61.559	0.63	-0.65	mo	yes
52	1989	Pointe-aux-Loups	47.530	-61.710	0.40	-0.59	mo	yes
53	1960	Millerand	47.220	-62.020	0.51	-0.51	mo	yes
		Stations Replaced by the Nearby Ones						
54		L'Îsle de l'est	47.620	-61.400	Remplacée par Grande Entrée, St# 51			yes
55		Bonaventure	48.030	-65.480	Remplacée par Havre-de-Beaubassin, St# 20			yes
56		Newport	48.280	-64.720	Remplacée par Chandler, St#18			yes
57		Pointe St-Pierre	48.630	-64.170	Remplacée par Mal-Bay, St#16			yes
58		Cap d'Espoir	48.417	-64.333	Remplacée par Anse-à-Beaufils, St# 17			yes
59		Islets Caribou	49.500	-67.220	Remplacée par Baie-Trinité, St# 32			yes
60		Ile Eskimo (Riv. St-Paul)	51.420	-58.300	remplacée Riv. St-Paul, St. # 46			yes

Tableau 1-2 La liste des stations et des liens vers les livrables. La troisième colonne du tableau contient les liens vers la série temporelle correspondante à la station de la reproduction historique réaliste (marées, les ondes de tempête et les niveaux d'eau totaux). La dernière colonne contient les liens vers la série temporelle stochastique climatique. Certaines stations ont été remplacées par la station la plus proche en raison d'absence d'observations, tel qu'indiqué dans la dernière section du tableau. Dans l'avant dernière colonne du tableau, le «yes» en noir indique qu'il y a un an d'observations, le «yes» en rouge signifie qu'il y a une courte série d'observations, et le "mo" en rouge indique que nous avons utilisé les résultats du modèle opérationnel de marée. Les valeurs du ZC en rouge dans le tableau indiquent qu'elles ont été interpolées d'une station voisine.

1.9 Références

Saucier, F.J., and J. Chassé, 2000. Tidal circulation and buoyancy effects in the St. Lawrence Estuary. Atmosphere-Ocean, 38(4): 505-556.

Saucier, F.J., F. Roy, D. Gilbert, P. Pellerin and H. Ritchie, 2003. Modeling the formation and circulation processes of water masses and sea ice in the Gulf of St. Lawrence, Canada. Journal of Geophysical Research, 108(C8): 3269.

Takashi Sakamoto, Yoshiki Komuro, Teruyuki Nishimura, Masayoshi Ishii, Hiroaki Tatebe, Hideo Shiogama, Akira Hasegawa; Takahiro Toyoda, Masato Mori, Tatsuo Suzuki, Yukiko Imada, Toru Nozawa; Kumiko Takata, Takashi Mochizuki; Koji Ogochi, Seita Emori; Hiroyasu Hasumi, Masahide Kimoto, 2012. MIROC4h—A New High-Resolution Atmosphere-Ocean Coupled General Circulation Model *Journal of the Meteorological Society of Japan*, Vol. 90, No. 3, pp. 325–359, 2012 325**.**

Xu, Z. 2014a. The All-Source Green's Function (ASGF) and its Applications to Storm Surge Modelling. Part II: From the ASGF Convolution to Forcing Data Compression and a Regression Model. Chapitre 2 de ce rapport.

Xu, Z. 2014b. The All-Source Green's Function (ASGF) and its Applications to Storm Surge Modelling. Part II: From the ASGF Convolution to Forcing Data Compression and a Regression Model. Chapitre 3 de ce rapport.

Xu, Z, J-P Savard, and D. Lefaivre 2014. Data Assimilative Hindcast and Climatological Forecast of Storm Surges at Sept-Iles with an ASGF Regression Model. Chapitre 4 de ce rapport.

2 Documentation en appui au rapport

Cette documentation comprend trois textes qui ont été acceptés pour publication dans deux journaux scientifiques différents, avec révision en cours. Les références complètes seront disponibles auprès des auteurs.

2.1 The All-Source Green's Function (ASGF) and its Applications to Storm Surge Modelling. Part I: From the Governing Equations to the ASGF Convolution

Zhigang Xu

Maurice Lamontagne Institute
Fisheries and Oceans Canada, Mont-Joli, Quebec

and

Institut des Sciences de la Mer
Université du Québec à Rimouski

(This section is adapted from a manuscript submitted to Ocean Dynamics on 2014/Oct/30 and accepted on 2015/Jan/19 subjected to revisions.)

2.1.0 Abstract

A new method to model storm surges is proposed. Without compromising modelling quality, the new method is thousands of times faster than the traditional method within the linear dynamics frame. The new method is also free of artificial open water boundary conditions. What supports this tremendous enhancement of modelling efficiency is the All-Source Green's Function (ASGF), which is the pre-calculated connection between a point of interest (POI) and the rest of the world ocean. Once it is calculated, it can be repeatedly used to fast produce the storm surge time series at the POI. With the ASGF, the storm surge modelling can be simplified as a convolution of a matrix with an atmospheric forcing field. The simplification will facilitate some other mathematical operations to further enhance the computational efficiency and to finally lead to a scheme for data assimilation.

Mathematical derivations from the depth averaged linear shallow water equations to the ASGF convolution and physical interpretation of the ASGF are presented in the paper along with

the algorithms and Matlab functions. Also presented are the results of testing the new method with a real storm surge event.

Keywords: ASGF, Convolution, Storm Surge

2.1.1 Introduction

This paper presents a new method for modelling storm surges within the linear and depth averaged shallow water dynamics system. The method is called the ASGF method. The acronym ASGF stands for the All-Source Green's Function, implying that all the model grid points can be the source points, in contrast to the traditional Green's function where only one or a few grid points are specified as the source points. The ASGF was first proposed by Xu (2007) to instantaneously predict tsunami arrivals at a point of interest (POI) from an arbitrary tsunami source in terms of both arrival times and wave amplitudes (also see Xu 2011). The ASGF can be used as a very efficient tool to model storm surges and tides as well, but its application to storm surge modelling will be focused on in this paper.

As it will be seen in the next section, the ASGF can be numerically derived from a storm surge model. All the numerical features that the storm surge model has will be passed on to the ASGF. The solution obtained via the ASGF method at a POI will be practically the same[5] to the solution obtained for the same point by running the surge model traditionally. However, as the realistic case in Section 2.1.5 shows, the ASGF method can compute 1555 times faster. This is because it cuts down computations for the solutions at millions of grid points which are not of interest. It targets its computations just at one or a few points where we need to know the solutions. The traditional modelling method has to map out the solutions at all the grid points no matter if they are needed or not. With such an enormous computational speed enhancement, some very long term simulations become feasible. For example, it is desirable to hydrodynamically convert some of the existing century long climate model solutions to storm

[5] Precisely speaking, within the length of the convolution kernel, the solutions by the traditional method and by the ASGF method are identical. After the length of the convolution kernel, the differences of the solutions by the two methods are negligible because of the frictions, if the length of the kernel is chosen appropriately. For the study reported here, the length of the convolution kernel is 72 hours.

surge time series for risk assessment due to climate change. It may not be possible to perform such a long term simulation with a traditional modelling approach, whereas using the ASGF method it can be achieved in a few minutes.

Besides its fast speed feature, another feature of the ASGF method is that it accounts for the influences of global forcing and global ocean geometry, and there are no more artificial open water boundary issues. This is because the ASGF can be prepared with the global ocean. Theoretically speaking, something that happens in any parts of the world's oceans will eventually affect the solution at a POI, significantly or insignificantly. This point will be better seen in Section 2.1.4. Putting aside the significance issue of the global influences, just for the sake of getting rid of the artificial open water boundaries, it is better off to include the entire world ocean as the domain to calculate the ASGF. It does not take long to calculate an ASGF with global coverage. As reported in Section 2.1.4, to pre-calculate a 72 hour long ASGF with the world ocean discretized in 5 minutes longitudes and latitudes, it only takes about 40 minutes in the author's laptop[6]. Once it is pre-calculated, it can be repeatedly used for any events.

The ASGF, like any other types of Green's functions, works only when the dynamics system in question is linear. However, the linear dynamics often provides the first order approximations, especially for storm surges, tides and tsunamis in deep water. Besides, when it comes to data assimilation, the missing nonlinearity effects may be quite much compensated by the best fit between the observations and the linear model parameters. This will be indeed the case for Sept-Iles, a test POI for this study, which will be reported in Part II of this study. For a place where nonlinear effect is expected to be strong, one may set up a local non-linear model but setting its open water boundaries at places where the non-linearity may expected to be weak. In this case, the ASGF method can be used to provide the nonlinear model with open water boundary conditions, in terms of the barotropic components, by supplying the time series of sea surface elevations and water mass transports along the open water boundaries. This topic will be explored in a future paper.

[6] Dell Precision M6600, with a processor of Intel Core i7-2960XM CPU 2.70GHz and solid state drive of OCZ Vertex3 SSD 2.5"480GB.

2.1.2 Linear and Depth Average Shallow Water Equations in Matrix Form

The following depth averaged linear shallow water equations, written in matrix form, are chosen to model storm surges,

$$\frac{\partial}{\partial t}\begin{bmatrix}\eta\\ u\\ v\end{bmatrix}=-\begin{bmatrix}0 & \frac{\partial}{\partial x} & \frac{\partial\cos\phi}{\cos\phi\,\partial y}\\ gh\frac{\partial}{\partial x} & \frac{\kappa}{h} & -f\\ gh\frac{\partial}{\partial y} & f & \frac{\kappa}{h}\end{bmatrix}\begin{bmatrix}\eta\\ u\\ v\end{bmatrix}-\begin{bmatrix}0 & 0 & 0\\ gh\frac{\partial}{\partial x} & 1 & 0\\ gh\frac{\partial}{\partial y} & 0 & 1\end{bmatrix}\begin{bmatrix}\eta_a\\ \tau_x\\ \tau_y\end{bmatrix} \tag{2-1}$$

where t is the time variable, x and y are the arc lengths along circles of latitude and longitude related with the longitude λ, latitude ϕ and the Earth's mean radius R (taken as 6371 km) by $x = R\lambda\cos\phi$ and $y = R\phi$; $\frac{\partial}{\partial x}=\frac{\partial}{R\cos\phi\,\partial\lambda}$, and $\frac{\partial}{\partial y}=\frac{\partial}{R\partial\phi}$; η, u and v are the sea surface elevation, and the mass fluxes in longitudinal and latitudinal directions; f and g are the Coriolis parameter, gravity acceleration; and h and κ are the water depth and bottom frictional coefficient. Note that the partial operator in the matrix affects all the factors that come to its right, e.g., the multiplication of $\frac{\partial\cos\phi}{\cos\phi\,\partial y}$ with v should be understood as $\frac{\partial(v\cos\phi)}{\cos\phi\partial y}$. To avoid the polar singularity, a rotated spherical coordinate system is used, the pole of which is rotated to (40W, 80N), a point on Greenland.

The second term on the RHS of eq. (2-1) contains the forces due to the atmospheric pressures and the wind stresses. The air pressures at the mean sea level, p_a, enter into the momentum equation as the inverse barometer η_a

$$\eta_a = -\frac{p_a}{\rho g} \tag{2-2}$$

where ρ is the sea water density, taken as $1025 kg/m^3$. The wind stresses τ_x and τ_y are obtained by converting the wind velocity components, U_{10} and V_{10}, at the 10 m above the sea level with

$$(\tau_x, \tau_y) = \frac{\rho_a}{\rho} C_d \sqrt{({u_{10}}^2 + {v_{10}}^2)}(u_{10}, v_{10}) \quad (2\text{-}3)$$

where ρ_a refers to the air density, taken as $1.25kg/m^3$, and C_d is the drag coefficient C_d specified by

$$C_d = \begin{cases} 1.6\times10^{-3}, & (\sqrt{U_{10}^2 + V_{10}^2} \le 7ms^{-1}) \\ 2.8\times10^{-3}, & \text{(otherwise)} \end{cases} \quad (2\text{-}4)$$

The formula for the drag coefficient was modified from Csanady (1982). The second line of the above equation is the modification by trial and error in fitting our model solutions to an observed storm surge.

At the sea bottom, a linear frictional stress, $\kappa(u,v)/h$, is used, by following Heaps (1969). However, Heaps used a constant $\kappa = 0.0024m/s$, whereas here a spatially varying κ is adopted by following Ding *et al.* (2004) and Tan (1992) such that it is inversely proportional to cubic root of water depth. This results in κ ranging from 4.5×10^{-4}m/s to 4.6×10^{-3}m/s in the world ocean. This is an attempt to reflect a general fact that there is less bottom friction in deep water than in shallow water. For more details, see Xu (2011).

The world ocean is taken as the model domain and the GEBCO08 (General Bathymetric Chart of the Ocean, http://www.gebco.net) is used for the bathymetry of the model. An advantage of using the global ocean as the model domain is that the model is free of artificial open water boundaries; all the lateral boundary conditions are zero normal flow conditions to the true coasts, i.e.,

$$u = 0, \quad \text{at the west and east coasts,} \quad (2\text{-}5)$$

$$v = 0, \quad \text{at the south and north coasts.} \quad (2\text{-}6)$$

Eq. (2-1) contains differential operators in space and in time. Xu (2011) gave details on how to replace the continuous differential operators with discretized difference operators, by using the central difference in space and the Sielecki's (1968) explicit-implicit scheme in time. For this study, the same central difference scheme in space is still used, but time wise the Leendertse's (1967) alternative directional implicit (ADI) scheme is adopted instead. An advantage of using the ADI scheme is that its time step is not restricted by the CFL condition anymore. Appendix A gives the ADI scheme in matrices.

Whatever a valid difference scheme we prefer, we can always end up with the following canonical form:

$$\begin{bmatrix} \boldsymbol{\eta} \\ \mathbf{u} \\ \mathbf{v} \end{bmatrix}^{(k+1)} = \mathbf{A}\begin{bmatrix} \boldsymbol{\eta} \\ \mathbf{u} \\ \mathbf{v} \end{bmatrix}^{(k)} + \mathbf{B}\begin{bmatrix} \boldsymbol{\eta}_{\mathbf{a}} \\ \boldsymbol{\tau}_{\mathbf{x}} \\ \boldsymbol{\tau}_{\mathbf{y}} \end{bmatrix}^{(k)} \qquad (k = 0, 1, 2, \cdots) \tag{2-7}$$

where k is 0-based time stepping index, the bold letters are the discretized versions of their continuous counterparts in Eq. (2-1). The matrix $\mathbf{A}$ updates the state vector $[\boldsymbol{\eta}\;\mathbf{u}\;\mathbf{v}]^{\mathrm{T}}$ from the current time step to the next. The initial value of the state vector can be assumed as zero for storm surge problem. The matrix $\mathbf{B}$ maps the atmospheric forcing into momentum to change the state vector. Introducing $\mathbf{x}$ to denote the state vector and $\mathbf{f}$ to denote the forcing vector $\mathbf{B}\,[\boldsymbol{\eta}_{\mathbf{a}}\;\boldsymbol{\tau}_{\mathbf{x}}\;\boldsymbol{\tau}_{\mathbf{y}}]^{\mathrm{T}}$,

$$\mathbf{x} \equiv \begin{bmatrix} \boldsymbol{\eta} & \mathbf{u} & \mathbf{v} \end{bmatrix}^{\mathrm{T}}, \qquad \mathbf{f} \equiv \mathbf{B}\begin{bmatrix} \boldsymbol{\eta}_{\mathbf{a}} & \boldsymbol{\tau}_{\mathbf{x}} & \boldsymbol{\tau}_{\mathbf{y}} \end{bmatrix}^{\mathrm{T}} \tag{2-8}$$

we can present eq. (2-7) in a compact form,

$$\mathbf{x}^{(k+1)} = \mathbf{A}\mathbf{x}^{(k)} + \mathbf{f}^{(k)}, \qquad (k = 0, 1, 2, \cdots) \tag{2-9}$$

where the superscripts with parentheses refer to time steps.

2.1.3 Storm Surge Solution and the All-Source Green's Function (ASGF)

The solution to Eq. (2-9) can be expressed in terms of initial conditions and the external forces as

$$\mathbf{x}^{(k+1)} = \mathbf{A}^{k+1}\mathbf{x}^{(0)} + \sum_{i=0}^{\mathrm{k}} \mathbf{A}^{i}\mathbf{f}^{(k-i)}, \quad (k = 0, 1, 2, \cdots) \tag{2-10}$$

where the superscripts without parenthesis refers to powers of the matrix. At first glance, the solution may appear impractical, since it requires powers of the matrix $\mathbf{A}$, whereas powers of a large size matrix are too expensive to compute. This would be indeed the case if we had to know solutions at all the grid points. However in reality, we need *not* to know solutions at every grid points. We only need to know solutions at a few POIs. In this case, we will only need to calculate a few rows of the matrix powers, instead of the entire matrix powers. Without loss of generality, let us assume that we have only one POI, say at the *nth* grid point, where the solution is wanted. In other words, only the *nth* component of the solution vector $\mathbf{x}$ is interested. In this case, as we can see from Eq. (2-10), all is needed is the *nth* row of each of the powers of $\mathbf{A}$. Introducing a new notation

$$\mathbf{r}_i \equiv \mathbf{A}^i(n,:). \qquad (2\text{-}11)$$

to represent the *nth* row of the *ith* power of $\mathbf{A}$, we can then write

$$\eta^{(k+1)} = \mathbf{r}_{k+1}\mathbf{x}^{(0)} + \sum_{i=0}^{\mathrm{k}} \mathbf{r}_i \mathbf{f}^{(k-i)}, \quad (k = 0, 1, 2, \cdots, k_{max}). \qquad (2\text{-}12)$$

where $\eta \equiv \mathbf{x}(n)$ to explicitly indicate that the nth component of the solution vector is a sea surface elevation, which is interested in this paper (but the velocities at a POI can be interested too). The row vector $\mathbf{r}_i$ can be calculated iteratively,

$$\mathbf{r}_{i+1} \quad = \quad \mathbf{r}_i\mathbf{A}, \qquad (\text{i=0,1,2,}\cdots, i_{max}), \qquad (2\text{-}13)$$

$$\mathbf{r}_0(j) \quad = \quad \begin{cases} 0, & j \text{ for all the grid points except for the } nth \\ 1, & j = n. \end{cases} \qquad (2\text{-}14)$$

As we can see, each iteration involves a multiplication of a row vector times a matrix, which can be performed very economically.

In the above, for simple presentation it is assumed that the matrix $\mathbf{A}$ is available. Xu (2011) gives an expression for $\mathbf{A}$ in terms of the global difference operators with the Sielecki's (1968) explicit-implicit scheme. However when the numerical scheme that discretizes the governing equations is more complicated, the matrix $\mathbf{A}$ may only be expressed as a product of several factor matrices. This is the case with the ADI scheme adopted by this study. In this case, we can still calculate the row vector $\mathbf{r}_i$ but in a slightly different way. Appendix A shows how we can still have the same canonical form can be derived with the ADI scheme. Appendix B shows how to calculate the row vector $\mathbf{r}_i$ defined above when the matrix $\mathbf{A}$ comes only in its factorization. Collecting all the row vectors, $\mathbf{r}_{i+1}$ (i=0,1,2,$\cdots, i_{max}$), into two matrices,

$$\mathbf{G_i} = [\mathbf{r}_1\ ; \mathbf{r}_2; \cdots; \mathbf{r}_{i_{max}}; \mathbf{r}_{i_{max}+1}]. \qquad (2\text{-}15)$$

$$\mathbf{G_c} = [\mathbf{r}_0\ ; \mathbf{r}_1\ ; \mathbf{r}_2; \cdots; \mathbf{r}_{i_{max}}\ ]. \qquad (2\text{-}16)$$

Then Eq. (2-12) can be written concisely as

$$\boldsymbol{\eta} = \mathbf{G_i x}^{(0)} + \mathbf{G_c} * \mathbf{f} \qquad (2\text{-}17)$$

where is $\boldsymbol{\eta} = [\eta^{(1)}\ \eta^{(2)}\ \eta^{(3)} \cdots \eta^{(k_{maxx}+1)}]^T$, a column vector containing the solution time series at a POI. The second term is a convolution, defined as

$$(\mathbf{G_c} * \mathbf{f})^{(k+1)} \equiv \sum_{i=0}^{k} \mathbf{G_c}(i+1,:)\mathbf{f}^{(k-i)}, \quad (k = 0, 1, 2, \cdots, k_{max}) \qquad (2\text{-}18)$$

where the notation '$*$' stands for a convolution operation. Eq. (2-17) shows that the solution is contributed by the two parts. The first term on the RHS is a contribution by the initial condition and the second term is a contribution by the external forcing. The forcing vector $\mathbf{f}$ changes with time. A convolution is needed because different instances of $\mathbf{f}$ produce different responses and these responses have to be added in the right order of time.

The contents of $\mathbf{G_i}$ and $\mathbf{G_c}$ are mostly the same. The same set of row vectors $\mathbf{r}_i$ ($i = 1, 2, 3, \cdots, i_{max}$) appear in both $\mathbf{G_i}$ and $\mathbf{G_c}$ but with their position shifted by 1; only $\mathbf{r}_0$ and $\mathbf{r}_{i_{max}+1}$ appear in one of the matrices. $\mathbf{G_i}$ is appropriate for a free wave problem like tsunamis, whereas $\mathbf{G_c}$ is good for a forced wave problem like storm surges. Both of them can be used as the definition of the all-source Green's function (ASGF). In the following text, when there is no ambiguity, their subscripts may be dropped off. The ASGF is an internal property of the dynamic system. It can be pre-calculated. Once it is calculated, it can be repeatedly used for any events such as tsunamis or storm surges.

A tsunami problem is an initial value problem, since there is no external forcing after the onset of a tsunami. Thus for a pure initial value problem like tsunamis, we have

$$\boldsymbol{\eta} = \mathbf{G_i x}^{(0)}. \qquad (2\text{-}19)$$

A single matrix times a column vector can be performed in no time. This means that we can *instantaneously* produce a tsunami arrival time series at a destination point. This of course also needs a reliable initial condition $\mathbf{x}^{(0)}$ (the so-called source function in tsunami literature). Xu and Song (2013) demonstrated the potential for fast tsunami predictions by combing the ASGF method and the GPS-derived source function (based on the ground movement of the coastal GPS-stations detected by the satellites) with the 2011 Tohoku tsunami as an illustrating case.

For a storm surge problem, the forcing field $\mathbf{f}$ will not be a zero field. It will vary with time and occupies the whole domain. After the forcing spins up the ocean, the convolution term will be a dominant term whereas the effect of the initial condition will be negligible due to friction. Therefore, for a forced wave problem like a storm surge, we can drop off the initial condition term and simply write

$$\boldsymbol{\eta} = \mathbf{G_c} * \mathbf{f} \; . \qquad (2\text{-}20)$$

The i_{max} in Eq. (2-13) and the k_{max} in Eq. (2-12) are both time stepping indices and all are associated with the same Δt inherited from the storm surge model of Eq. (2-9). However they do not have to be the same. Usually i_{max} is much less than k_{max}. The $k_{max} \times \Delta t$ is the duration of the simulation, say a few months or a few years. The $i_{max} \times \Delta t$ represents a time beyond which the row vector $\mathbf{r}_i$ for $i > i_{max}$ becomes negligibly small due to frictional effect. For example, Figure 2-3 shows how a component of $\mathbf{r}$ decays to almost to zero after a day. As we will see in Part II of this study (Xu, 2014), even with all the components of $\mathbf{r}$ taken into account, it is sufficient to set i_{max} such that $i_{max} \times \Delta t = 72\ hours$. In short, the index i_{max} is the length of convolution kernel, whereas the index k_{max} is the length of simulation. The value of Δt is set internally by the storm surge model for stability or accuracy of the solution. It is usually on an order of seconds or minutes. However we may not wish to output the solution at such a fine time step. We can choose a much larger time step, say an hour, to output the solutions. An hourly time series of the output is very common in storm surge modelling. The difference between the two types of time steps, the surge model internal time step and solution output time step, can be taken as advantage to greatly reduce the size of $\mathbf{G}$; see Appendix C for details.

Recall from the second part of Eq. (2-8), the forcing vector $\mathbf{f}$ is defined as

$$\mathbf{f} \equiv \mathbf{B}\begin{bmatrix} \boldsymbol{\eta}_\mathbf{a} & \boldsymbol{\tau}_\mathbf{x} & \boldsymbol{\tau}_\mathbf{y} \end{bmatrix}^{\mathrm{T}} . \qquad (2\text{-}21)$$

The column vector on the RHS is interpolated from an atmospheric model grid, i.e.,

$$\begin{bmatrix} \boldsymbol{\eta}_\mathbf{a} & \boldsymbol{\tau}_\mathbf{x} & \boldsymbol{\tau}_\mathbf{y} \end{bmatrix}^{\mathrm{T}} = \mathbf{L}\begin{bmatrix} \tilde{\boldsymbol{\eta}}_\mathbf{a} & \tilde{\boldsymbol{\tau}}_x & \tilde{\boldsymbol{\tau}}_y \end{bmatrix}^{\mathrm{T}} \qquad (2\text{-}22)$$

where the variables with tildes are defined on an atmospheric model grid, and $\mathbf{L}$ is the interpolation matrix. Usually the spatial resolution of an atmospheric model is much coarser than a surge model. This means that the column vector on the RHS will be much shorter than the one on the LHS of Eq. (2-22) and the interpolation matrix $\mathbf{L}$ will be tall and thin. For the realistic test case shown in Section 2.1.5, the length of the column vector on the LHS of Eq. (2-22) is 32,377,503 and the length of column vector on the RHS is 408,622. Thus it is very worthwhile to substitute Eqs. (2-21) and (2-22) into (2-20) to greatly reduce the number of columns of the convolution matrix. The substitution results in

$$\boldsymbol{\eta} = \mathbf{G_{cL}} * \tilde{\mathbf{f}} \qquad (2\text{-}23)$$

with

$$\mathbf{G_{cL}} \equiv \mathbf{G_c B L}\,, \qquad (2\text{-}24)$$

$$\tilde{\mathbf{f}} \equiv \left[\tilde{\boldsymbol{\eta}}_\mathbf{a}\ \tilde{\boldsymbol{\tau}}_\mathbf{x}\ \tilde{\boldsymbol{\tau}}_\mathbf{y}\right]^\mathrm{T}. \qquad (2\text{-}25)$$

Now $\mathbf{G_{cL}}$ is a new convolution matrix, whose number of columns are much less than that of $\mathbf{G_c}$ For the example case just mentioned, the number of its columns of $\mathbf{G_{cL}}$ is 408,622, a reduction by 31,968,881 from that of $\mathbf{G_c}$. This is a huge reduction. Thus Eq. (2-23) should be actually used for a real storm surge simulation. See Appendix C for how this idea is implemented in Matlab.

2.1.4 Interpretations of the ASGF

The matrix $\mathbf{G}$ (either $\mathbf{G_i}$ or $\mathbf{G_c}$) can be interpreted with physical meanings, which may shed light on what is going on behind the mathematics. Figure 2-1 should remind us of a concept often seen in text books: the dependence intervals for 1-dimensional wave solution. It tells how the wave solution at a point of interest, *x*, depends only on the conditions within the interval of $[x-ct, x+ct]$ where c is the wave speed, which is constant in this simple case. The dependence interval grows with the time at the same rate as the wave speed *c*.

Wave solutions at a point on the real ocean surface have a domain of dependence too. However, this seems to have received little attention in practice, perhaps owing to the fact that it is hard to visualize this domain from solutions obtained with a conventional modelling approach.

Now with the matrix **G**, we can not only see the domain of dependence but also know weights of the dependence. Each row of **G** contains the domains of dependences at a particular time. Figure 2-2 shows the domains of dependence of the wave solutions at Sept-Iles at 4 different times. Panel (a) shows the domain of dependence at *t=6* hours: the solution at Sept-Iles depends only on the conditions within the colorful region. The condition outside of the region has no effects on the solutions yet; they take longer time to affect the solutions. Panels a, b, c and d together illustrate how the domain of dependence grows with time at the same rate as the wave speeds. The wave speeds in a real ocean are spatially varying, largely controlled by the local water depths. As shown in panel (d), the domain of dependence has covered the entire world ocean in 48 hours. This means that anything that happens in the world ocean can all affect the wave solution at Sept-Iles within 2 days, significantly or insignificantly. The colour spectrum indicates the weights of the dependences, which can be positive or negative. A negative weight means a positive impulse will cause a negative response, and vice-versa. We may refer domains and weights of dependence collectively as a field of dependence. Values of the weights are largely affected by the resolution of the model grid. The finer the grid spacing is, the smaller the weights will be. The weights shown in the figure are for a model grid spacing of 5 minutes in longitude and latitude. The field of dependence may also be termed as the connections between the POI and the rest of the world ocean, which may sound more intuitive to a broad audience.

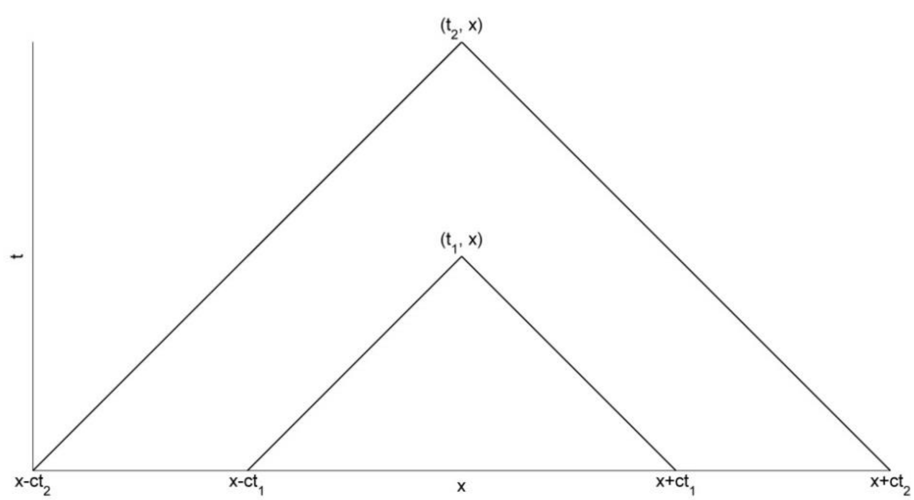

Figure 2-1 One-dimensional wave solution at a point x depends on the initial condition only within the interval [x-ct, x+ct]. The interval of dependence grows at the same rate as the wave speed *c*.

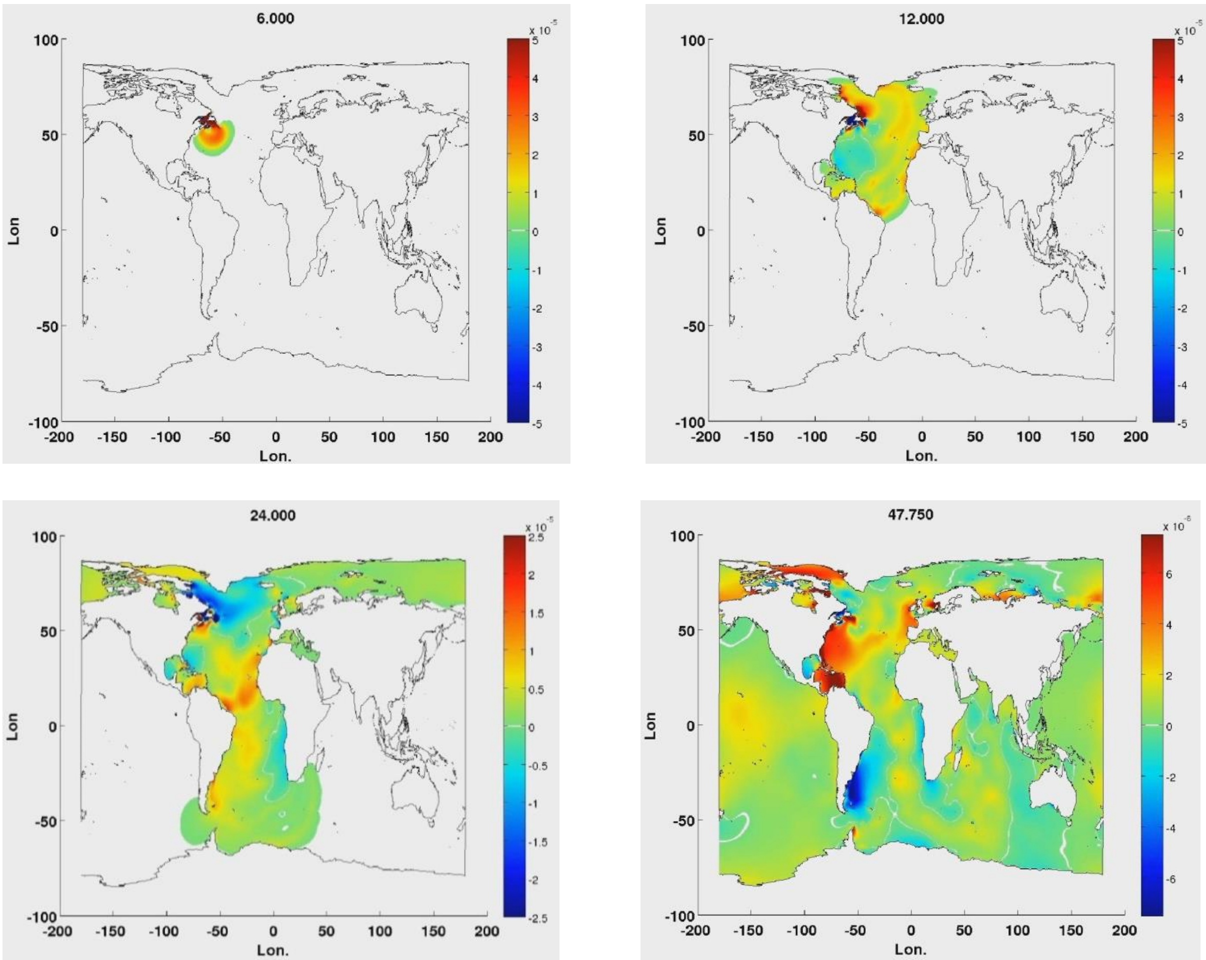

Figure 2-2. Domains of dependence of wave solutions at Sept-Iles of Estuary of Gulf of St. Lawrence at t=6, 12, 24 and 48 (47.75 precisely) hours as shown by panels a, b, c, and d. The color spectrum indicates weights of the dependence. Note that the longitudes and latitudes shown above are not natural ones. They are rotated longitudes and latitudes used by the model. The pole of the natural spherical coordinates is rotated out of water to a place at Greenland (40W, 80N) to avoid the polar singularity in the water.

The columns of $\mathbf{G}$ contain Green's functions. Each column is a response time series to an impulse placed at a grid point. There are as many such Green's functions as there are number of grid points. Hence the name of "all-source Green's function": all the model grid points are allowed to be the source points. Figure 2-3 illustrates one of the Green's functions, the response to an air pressure impulse placed at Sept-Iles.

Thus, $\mathbf{G}$ contains a complete set of information on the linear dynamics system. Its rows contain the information how the POI is connected to the rest of the world (i.e., the fields of dependence); its columns contain all the Green's functions to the delta-forcings at the grid points. The matrix G, or to say the ASGF, is an internal property of the linear dynamics system. It is independent of external forcing. It can be calculated before events. Once it is pre-calculated, it can be repeatedly used to fast produce responses to tsunami or storm surge events. It can be also used to model tides (which will be the topic of another paper). All the time consuming computations (such as due to the small time steps) have been absorbed at the stage of calculation for $\mathbf{G}$. To calculate a $\mathbf{G}$ matrix of 72 hour long and covering the world ocean with a grid spacing of 5 minute, it only takes about 40 minutes on the author's laptop.

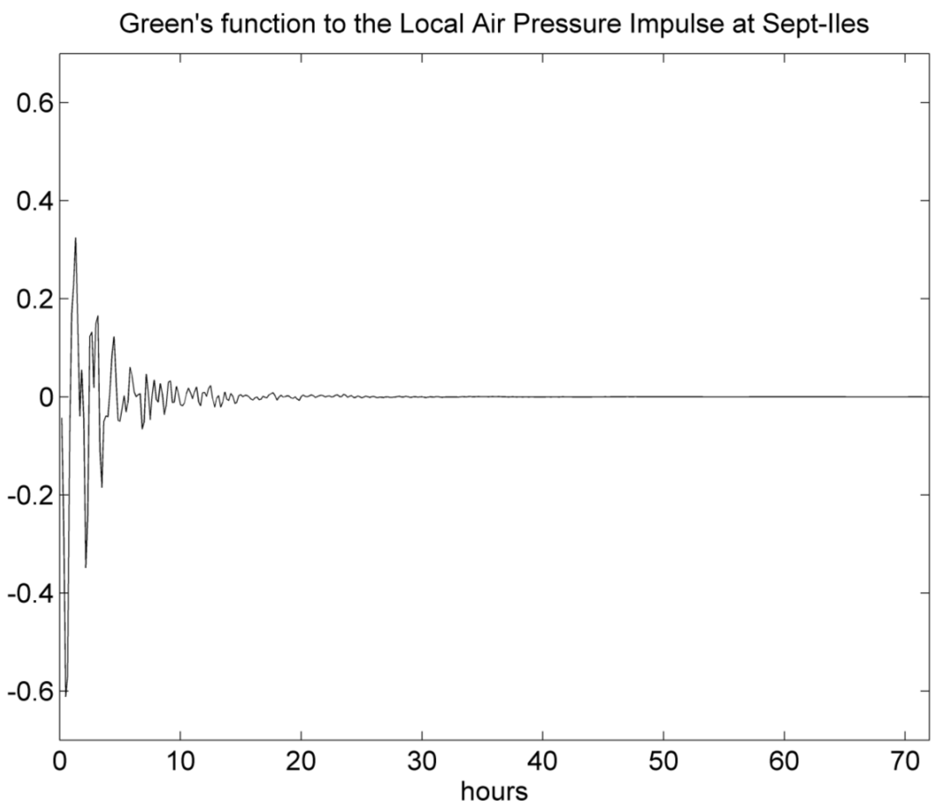

Figure 2-3 Each column of G is a Green's function to an impulse placed at a grid point. There are as many such Green's functions as the model grid points. Shown here is one of the Green's functions, corresponding to an air pressure impulse placed at Sept-Iles.

2.1.5 Test with a Real Storm Surge Event

Through the ASGF, a storm surge model has been reduced to a convolution as expressed by Eq. (2-20). It is time to test it with a real event. Between December 6 and 7, 2010, there was a big storm moving over the Estuary of Gulf of St. Lawrence. Shown in panel (a) of Figure 2-4 is a snapshot of air pressures at the mean sea level, based on the MERRA data (see below). The storm in the air caused a big surge in the water, which in turn damaged coastal high ways and many residential properties. Shown in panels (b) and (c) are examples of the damages. For the test, the tidal gauge at Sept-Iles, operated by Canadian hydrographic Service (CHS), is chosen as the POI. Panel (b) of Figure 2-4 shows its location. The ASGF matrix $\mathbf{G}$ for this POI has been calculated and illustrated in Figure 2-2.

For the test, the MERRA data is chosen to supply the atmospheric forcing. The acronym MERRA stands for **M**odern-**E**ra **R**etrospective **A**nalysis for **R**esearch and **A**pplications. It is produced by NASA and available in http://gmao.gsfc.nasa.gov/merra/. It is a re-analyzed dataset, utilizing the NASA global data assimilation system and a variety of global observing systems. It is meant to provide the science and applications communities with state-of-the-art global dataset. Its temporal resolution is hourly and spatial resolution is 0.50 degrees in latitude and 0.67 degrees in longitude. It covers the period from 1979 to present. It is adopted for this study because its solutions are highly realistic, has hourly temporal resolution (which is high), and covers the whole globe. At any hour, the MERRA data gives a forcing vector of 408,622 elements consisting of the points of air pressures and wind stresses in the global ocean.

The Matlab function `conv_FG` in Appendix D implements Eq. (2-20) in Matlab. It requires the forcing vectors at different instants arranged into forcing matrix $\mathbf{F}$ (see Eq. (2-52) in the appendix). With both $\mathbf{G}$ and $\mathbf{F}$ prepared, we can simply plug them into this function to quickly produce the simulations. The simulation period is extended beyond the days of the event to include the whole month of December of 2010. The MERRA data of the whole month plus 72 hours proceeding December 1, 2010 are pulled out to form a series of forcing vectors. To extend the forcing field backwards to include the last 72 hours from November is a way to deal with the unknown initial condition. After the computation, the first 72 hours of the time series will be discarded. This way, the unknown initial condition is actually pushed backwards three days before December 1 to let them to have a sufficient time to decay.

Shown in Figure 2-10 is a comparison between the observation and the simulation. As we can see, the observed surge that peaked at zero hours on December 7 is well captured by the simulation. The overall agreement between the observations and the simulations for the whole month also looks good. The γ^2 as defined below quantitatively measures the overall misfits

$$\gamma^2 = \frac{\text{sum of squares of misfits}}{\text{sum of sqaures of observations}} \quad . \tag{2-26}$$

The smaller this ratio is, the better the agreement. The value of the γ^2 for the non-data assimilative simulation is 0.18. In other words, 82% of the observed variance is accounted for by the simulation. The effects of global forcing and global ocean geometry have all been accounted in the time series.

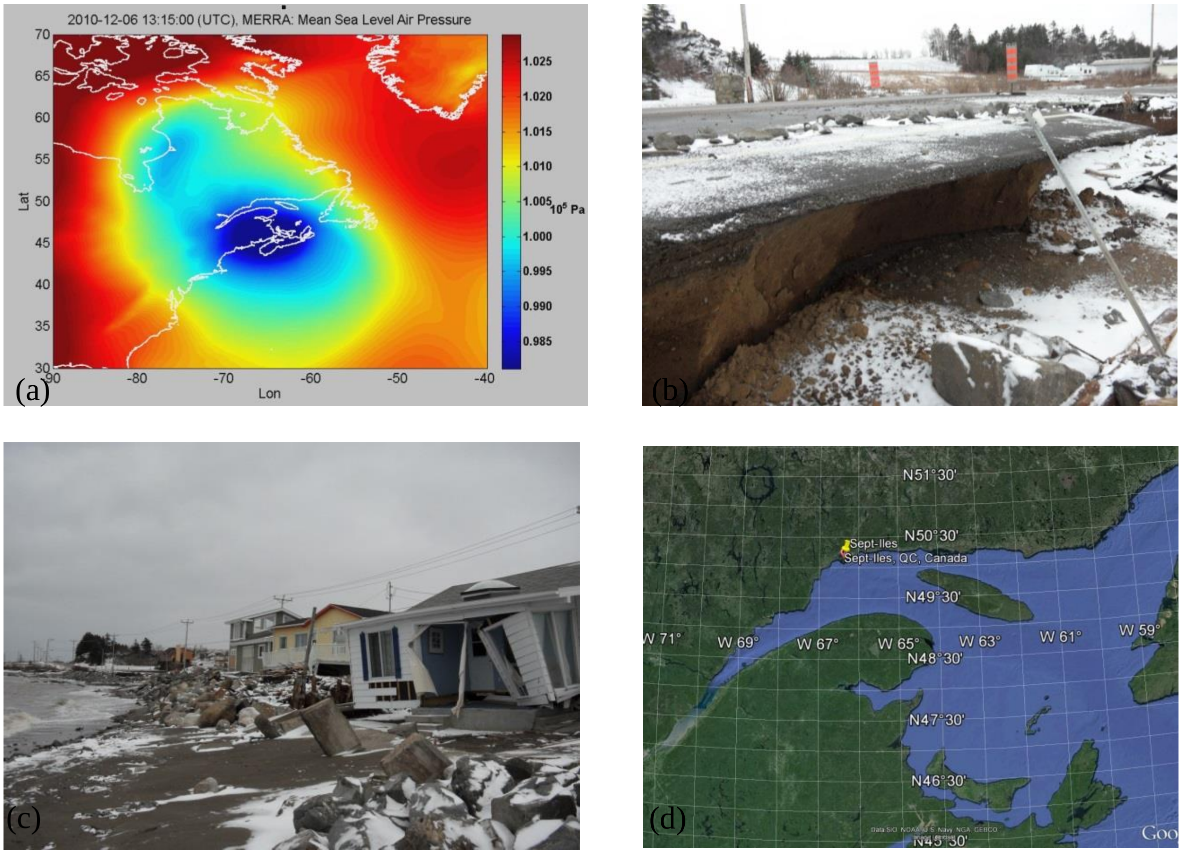

Figure 2-4 Panel (a) is a snapshot of the air pressure at the mean sea level. The storm caused a big surge in the water, which damaged the coastal highway and residential properties as shown in Panels b and c. Sept-Iles is chosen as a point of interest to simulate the storm surge; its location is shown in panel (d). Note that the longitudes and latitudes shown in panel (a) are not the same as those on panel (d). The former are based on the rotated spherical coordinates used by the model.

To produce the whole month of the time series shown in Figure 2-10, it only takes 45 seconds, of which 33 seconds were used to retrieve the forcing data from the disk. It takes only 12 seconds for the function `conv_FG` to finish the convolution calculation. In contrast, to produce the same time series with the conventional modelling approach (i.e., by running the model as Eq. (2-9)), it will take 19.45 hours. The ASGF method is 1555 times faster! Part II of this study (Xu, 2014b) will show that when the $\mathbf{G}$ matrix is further applied with the singular value decomposition (SVD) and the forcing field is compressed accordingly, this simulation can go even much faster, at a speed of 0.5 seconds of computer time for a 10-year hourly simulation. Such an extremely fast simulation speed will make it possible to run some very long simulations. There exist some climate model solutions for next hundred years. With the new method we can easily convert these century long climate model solutions to the time series of storm surges at set of POIs. Using this new approach, Xu et al (2014) computed storm surge time series for Sept-Iles with a climate forcing field spanning years from 1961 to 2100.

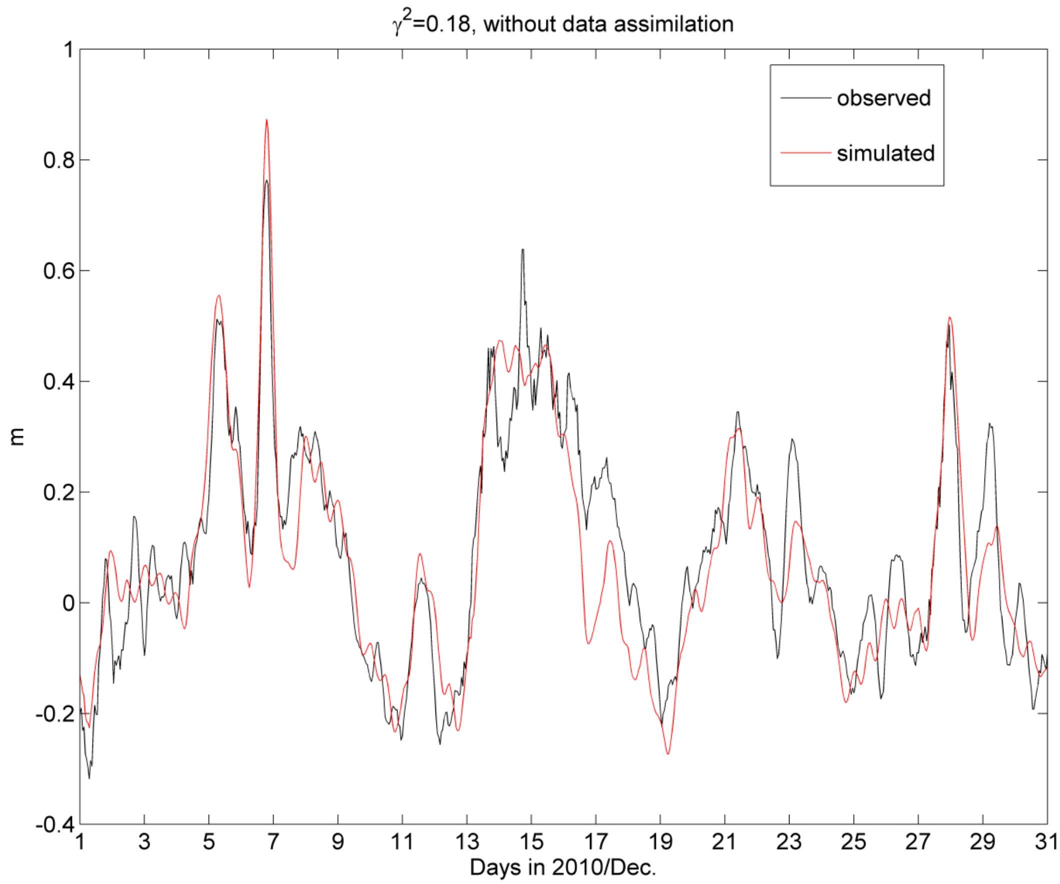

Figure 2-5 Comparisons of the simulations (in red) of storm surges against the observations (in black) at Sept-Iles for the month of December 2010. The value of γ^2 shown in the title measures how much the overall misfit is between the observations and the simulations. There are 744 hourly data points in each time series.

2.1.6 Summary and Discussions

Starting from the depth averaged linear shallow water equations, this paper first works out algorithms to calculate the ASGF for two situations: one situation is where the dynamics matrix $\mathbf{A}$ is available as a single matrix, resulting from using a simple discretizing numerical scheme such as Sielecki's (1968) explicit-implicit scheme; another situation is where the dynamic matrix $\mathbf{A}$ only can be presented as a product of several factor matrices, and it is not feasible to multiply out the product. The second situation arises from using more advanced discretizing scheme such as ADI. Appendix A and B present the ADI scheme in matrix and the corresponding ASGF algorithm. Appendix C presents two Matlab functions on how to calculate the ASGF matrices for a free wave problem, $\mathbf{G_i}$, and for a forced wave problem, $\mathbf{G_c}$. The latter needs to be calculated differently from the former so that the relatively slow variation of the atmospheric forcing field can be taken as an advantage to reduce the size of $\mathbf{G_c}$.

The ASGF is then interpreted the in two ways: the rows of the ASGF matrix contain the information how the POI is connected with the rest of the world ocean at different times (more precisely, the field of dependence); the columns of the matrix contain all the Green's functions corresponding to the impulse forces at all the grid points. The ASGF method is then tested with a real storm surge case. The simulation it produces accounts for 82% of the observed variance, without resorting to data assimilation technique. This means that all the pieces associated with the ASGF method have been put together correctly and the new method works as it should. To produce the same simulation time series shown in Figure 2-10, the new method works 1555 times faster than the traditional method.

Eq. (2-7) is a canonical form shared essentially by all linear storm surge models, although they may not be written in matrix form. Different models differ only in the content of $\mathbf{A}$. To run a traditional storm surge model is essentially the same as to iteratively solve Eq. (2-7). Two features are common to all traditional storm surge models: they all have to map out solutions at every grid points even though only solutions at few grid points are interested; they all have to bear small time steps, for the sake of stability or accuracy, even though hourly output is common in storm surge simulations. These two features imply intensive computations. Consequently, it is rare to see a global storm surge model. Most seen are regional models. A regional model may imply a less computational load; however it trades for another challenge, which is the artificial open water boundary condition issue.

The ASGF method proposed in this paper goes a level above the traditional modelling approach. Instead of using Eq. (2-7) to run for individual events, the algorithm of Eqs. (2-13) and (2-14), which is derived from Eq. (2-7), are used to run for the all-source Green's functions (ASGF). The ASGF only needs to be calculated once and for all. Once it is calculated, it can be repeatedly used for any events. Each time a convolution of the ASGF matrix with a forcing field will give a fast response to an event. As far as the linear dynamics is valid, the ASGF method has all the merits of traditional storm surge modelling, but can make the modelling thousands of times faster. It also accounts for the influences of global forcing fields and of the global ocean geometry. It gets rid of the open water boundary condition issue completely, since it can affordably embrace the whole world ocean as its domain.

In the terminology of system and control theory, the ASGF is a system of multiple inputs and single output (MISO). The multiple inputs are a global forcing field, $\mathbf{f}$, defined on model grid points, the single-output is a response time series, $\boldsymbol{\eta}$, at a POI. The ASGF, which comes as a numerical matrix $\mathbf{G}$, is the kernel of the MISO system. With the same $\mathbf{G}$ but a different type of forcing $\mathbf{f}$, the system becomes a different model: when $\mathbf{f}$ is an atmospheric forcing field, the system is a storm surge model; when $\mathbf{f}$ is an astronomic forcing field, the system is a tide model; when $\mathbf{f}$ is tectonic (via a so-called tsunami source function) the system is a tsunami model. The system has been tested with a real tsunami case and a real storm surge case. Its testing with tidal observations will be reported in the near future.

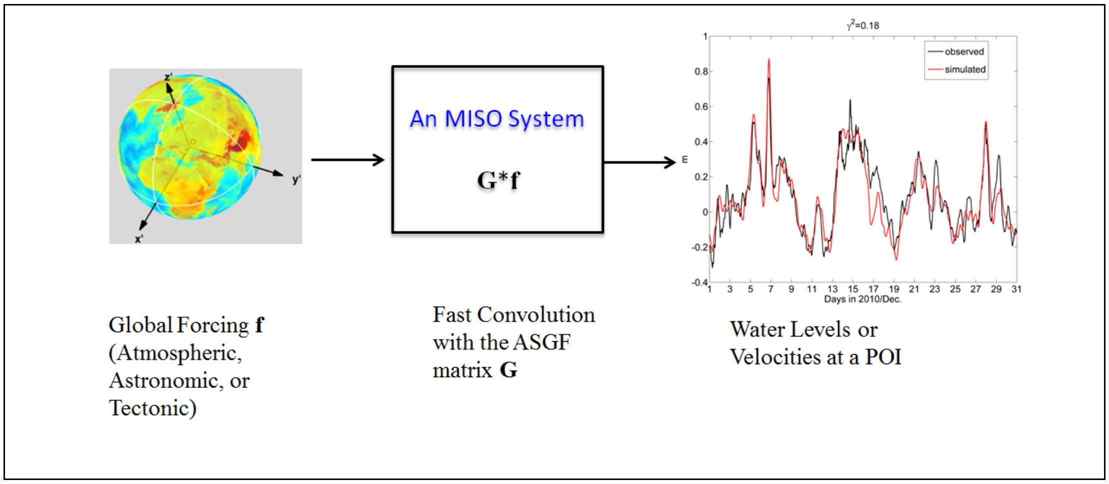

Figure 2-6. An MISO system with the ASGF as its kernel. A global forcing field can be atmospheric, astronomic or tectonic, defined on the entire or any part of the domain. A convolution of the ASGF matrix $\mathbf{G}$ with the forcing field can quickly yield the response.

The ASGF simplifies the expression of a storm surge model. It expresses sea surface elevations at a POI as a convolution of a matrix with a forcing field. This simplification opens a door to many other mathematical operations, such as singular value decompositions (SVD), fast Fourier transform (FFT) and liner regression analysis. These operations will make the storm surge modelling even faster and data assimilative. These points will be considered in a companion paper (Part II, Xu 2014).

2.1.7 Acknowledgement

This study was partially supported by le Ministère des Transports du Québec, and by the ACCASP program of Department of Fisheries and Oceans. This study also benefited from the collaborations with the OURANOS Consortium[7]. The free access to the MERRA data made by NASA is also greatly appreciated. The author also would like to gratefully acknowledge the supports from his own institute.

[7] http://www.ouranos.ca/

2.1.8 Appendix A: The ADI scheme in Matrices

The alternative directional implicit scheme (ADI) to model long waves in the ocean was first developed by Leendertse's (1967). This appendix is to present the ADI scheme in matrices and to show that the form of Eq. (2-9) still holds.

It is always possible to turn Eq. (2-1) first into a semi-discretized form as

$$\frac{d\mathbf{x}}{dt} = \mathbf{C}\mathbf{x} + \mathbf{D}\hat{\mathbf{f}}\,, \tag{2-27}$$

where $\mathbf{x}$ is the same as defined by Eq. (2-8), the matrices $\mathbf{C}$ and $\mathbf{D}$ holds spatial difference operators, and

$$\hat{\mathbf{f}} \equiv \begin{bmatrix} \boldsymbol{\eta}_{\mathbf{a}} & \boldsymbol{\tau}_{\mathbf{x}} & \boldsymbol{\tau}_{\mathbf{y}} \end{bmatrix}^{\mathrm{T}}. \tag{2-28}$$

To say it a semi-discretized form because only the space is discretized but the time still remains continuous. It is easy to calculate $\mathbf{C}$ since it is only a matter of assembling the spatial difference operators. Also $\mathbf{C}$ is highly sparse, hence it is feasible to store them in the computer RAM even for a fairly large size of the system, such as the one used for this study, which has 32,224,425 grid points, resulted from 5-minute discretizing of the global ocean, and its sparsity is on the orders of 10^{-7}.

Various numerical schemes arise from different ways to discretize the time derivative and from how to evaluate the state vector $\mathbf{x}$ on the RHS of Eq. (2-27). The way that the ADI does is this: it first splits the matrix $\mathbf{C}$ into two parts

$$\mathbf{C} = \mathbf{C}_{\mathbf{x}} + \mathbf{C}_{\mathbf{y}} \tag{2-29}$$

where $\mathbf{C}_{\mathbf{x}}$ only involves the x-directional spatial difference operators and $\mathbf{C}_{y}$ only involves the y-directional spatial difference operators. Then in discretizing the time it splits the time step into two halves such that

$$\frac{\mathbf{x}^{(k+1/2)} - \mathbf{x}^{(k)}}{\Delta t/2} = \mathbf{C}_{\mathbf{x}}\mathbf{x}^{(k+1/2)} + \mathbf{C}_{\mathbf{y}}\mathbf{x}^{(k)} + \mathbf{D}\hat{\mathbf{f}}^{(k)}, \tag{2-30}$$

$$\frac{\mathbf{x}^{(k+1)} - \mathbf{x}^{(k+1/2)}}{\Delta t/2} = \mathbf{C}_{\mathbf{x}}\mathbf{x}^{(k+1/2)} + \mathbf{C}_{\mathbf{y}}\mathbf{x}^{(k+1)} + \mathbf{D}\hat{\mathbf{f}}^{(k+1/2)}. \tag{2-31}$$

where $s = \Delta t / 2$. In the first half time step, the implicit scheme is applied to the x-direction only, and in the second half time step, the implicit scheme is applied to the y-direction only. This way, a solution in each half step only requires a tri-diagonal matrix algorithm, which is not costly. It is reasonable to assume that the external forcing does not change from the first half step to the second half, i.e., we can assume $\mathbf{f}^{(k+1/2)} = \mathbf{f}^{(k)}$. Then from Eqs. (2-30) and (2-33) we can have

$$(\mathbf{I} - \frac{\Delta t}{2}\mathbf{C}_\mathbf{x})\mathbf{x}^{(k+1/2)} = (\mathbf{I} + \frac{\Delta t}{2}\mathbf{C}_\mathbf{y})\mathbf{x}^{(k)} + \frac{\Delta t}{2}\mathbf{D}\hat{\mathbf{f}}^{(k)}, \tag{2-32}$$

$$(\mathbf{I} - \frac{\Delta t}{2}\mathbf{C}_\mathbf{y})\mathbf{x}^{(k+1)} = (\mathbf{I} + \frac{\Delta t}{2}\mathbf{C}_\mathbf{x})\mathbf{x}^{(k+1/2)} + \frac{\Delta t}{2}\mathbf{D}\hat{\mathbf{f}}^{(k)}. \tag{2-33}$$

Factorize $(\mathbf{I} - s\mathbf{C}_\mathbf{x})$ and $(\mathbf{I} - s\mathbf{C}_\mathbf{y})$ as follows

$$\mathbf{P_a}(\mathbf{I} - \frac{\Delta t}{2}\mathbf{C}_\mathbf{x}) = \mathbf{L_a}\mathbf{U_a} \tag{2-34}$$

$$\mathbf{P_b}(\mathbf{I} - \frac{\Delta t}{2}\mathbf{C}_\mathbf{y}) = \mathbf{L_b}\mathbf{U_b} \tag{2-35}$$

where $\mathbf{L_a}$ and $\mathbf{L_b}$ are lower triangle matrices, $\mathbf{U_a}$ and $\mathbf{U_b}$ are upper triangle matrices, and $\mathbf{P_a}$ and $\mathbf{P_b}$ are permutation matrices. [8] This decomposition is known as o the *lu*-decomposition (lower and upper triangle decomposition). Noticing that permutation matrices are orthogonal matrices, we have

$$(\mathbf{I} - \frac{\Delta t}{2}\mathbf{C}_\mathbf{x})^{-1} = \mathbf{U_a}^{-1}\mathbf{L_a}^{-1}\mathbf{P_a} \tag{2-36}$$

$$(\mathbf{I} - \frac{\Delta t}{2}\mathbf{C}_\mathbf{y})^{-1} = \mathbf{U_b}^{-1}\mathbf{L_b}^{-1}\mathbf{P_b} \tag{2-37}$$

The inverses of $\mathbf{L}$ and $\mathbf{U}$ are easy to carry out, since they are triangle matrices. To have this *lu*-decomposition done beforehand will help to speed up the model running.

Eqs. (2-32) and (2-33) can then be solved as

$$\mathbf{x}^{(k+1/2)} = \mathbf{U_a}^{-1}\mathbf{L_a}^{-1}\mathbf{R_a}\mathbf{x}^{(k)} + \frac{\Delta t}{2}\mathbf{U_a}^{-1}\mathbf{L_a}^{-1}\mathbf{P_a}\mathbf{D}\tilde{\mathbf{f}}^{(k)}, \tag{2-38}$$

[8] The factor matrices can be obtained by the Matlab command *lu*. For example, [La, Ua, Pa]=lu(I-sCx);.

$$\mathbf{x}^{(k+1)} \quad = \quad \mathbf{U_b}^{-1}\mathbf{L_b}^{-1}\mathbf{R_b}\mathbf{x}^{(k+1/2)} + \frac{\Delta t}{2}\mathbf{U_b}^{-1}\mathbf{L_b}^{-1}\mathbf{P_b}\mathbf{D}\tilde{\mathbf{f}}^{(k)}\,. \tag{2-39}$$

where

$$\mathbf{R_a} \equiv \mathbf{P_a}(\mathbf{I} + \frac{\Delta t}{2}\mathbf{C_y}) \tag{2-40}$$

$$\mathbf{R_b} \equiv \mathbf{P_b}(\mathbf{I} + \frac{\Delta t}{2}\mathbf{C_x}) \tag{2-41}$$

Merging the two half step solutions shown by (2-38) and (2-39) into one step solution

$$\mathbf{x}^{(k+1)} = \mathbf{U_b}^{-1}\mathbf{L_b}^{-1}(\mathbf{R_b}\mathbf{U_a}^{-1}\mathbf{L_a}^{-1}\mathbf{R_a}\mathbf{x}^{(k)} + \Delta t\ \mathbf{P_b}\mathbf{U_a}^{-1}\mathbf{L_a}^{-1}\mathbf{P_a}\mathbf{D}\hat{\mathbf{f}}^{(k)}) \tag{2-42}$$

Let

$$\mathbf{A} \equiv \mathbf{U_b}^{-1}\mathbf{L_b}^{-1}\mathbf{R_b}\mathbf{U_a}^{-1}\mathbf{L_a}^{-1}\mathbf{R_a} \tag{2-43}$$

$$\mathbf{f}^{(k)} \equiv \Delta t\ \mathbf{U_b}^{-1}\mathbf{L_b}^{-1}\mathbf{P_b}\mathbf{U_a}^{-1}\mathbf{L_a}^{-1}\mathbf{P_a}\mathbf{D}\hat{\mathbf{f}}^{(k)} \tag{2-44}$$

we finally arrive at

$$\mathbf{x}^{(k+1)} = \mathbf{A}\mathbf{x}^{(k)} + \mathbf{f}^{(k)} \tag{2-45}$$

which recovers the canonical form of Eq. (2-9). The ADI scheme is a two-step discretizing scheme. The above derivation should serve as an example on how to arrive at the canonical form if another type of discretizing scheme is used.

The matrix $\mathbf{A}$ in the above is given in its 6 factor matrices. We should not try to multiply out the product of these factor matrices when the system is of large size for two reasons: firstly it would take too long to carry out the multiplications and secondly the product matrix $\mathbf{A}$ would be too full to store in computer RAM. When it comes to multiplication with a column vector, such as, $\mathbf{A}\mathbf{x}^{(k)}$, we can perform the multiplications of the factor matrices with the column vector successively from the right to the left, i.e., $\mathbf{U_b}^{-1}(\mathbf{L_b}^{-1}(\mathbf{R_b}(\mathbf{U_a}^{-1}(\mathbf{L_a}^{-1}(\mathbf{R_a}\mathbf{x}^{(k)})))))$, each of the multiplications results in only a column vector.

The ADI scheme has two advantages: it is stable without restriction of the CFL condition and it conserves the total mechanical energy of the system. Leendertse (1967) and Wesseling

(2009) showed that the ADI method imposes no necessary stability condition for the time step for the linear systems similarly to Eq. (2-45), based on the Fourier stability analysis (von Newman stability analysis). Although the Fourier stability analysis does not tell a sufficient time step condition either to guarantee the stability, a test run of model Eq. (2-45) for 10 days shows that the model is stable with $\Delta t = 600$ seconds and a 5-minute gridded global ocean as the model domain with realistic bathymetry. In contrast, using the Sielecki's (1968) explicit-implicit scheme, the time step would be necessarily bounded with the CFL condition, which is 5 seconds for the same global model domain. Another advantage of the ADI scheme is its conservation of the total mechanical energy of the system. The total mechanical energy, which is the sum of the potential and kinetic energies domain wise, should be conserved in a frictionless environment. However, this physical law may be violated to various degrees by different numerical schemes. An unstable scheme will result in unbounded growth of the total energy. While a stable scheme has to necessarily keep the total energy upper bounded, it may cause the total energy to fluctuate around its initial value or to decay. That the total energy decays with the time, known as numerical dissipation, is not good either. A good numerical scheme should keep the fluctuation of total energy as little as possible. Shown in Figure 2-7 is a comparison of the total energy conservations by two schemes for an initial value problem, where an initial distribution sea surface is suddenly released in frictionless sea water body (Figure 2-8). The top panel of Figure 2-7 shows how the ADI scheme keeps the total mechanical energy almost constant as shown by the flat blue line. The panel also shows how the potential energy in green and the kinetic energy in red vary with time but their sum, the total energy show in blue, stay constant visibly. The middle panel shows the energy time series by Sielecki's scheme. The total energy does not appear as flat as the one in the top panel since it has noticeable fluctuations. The bottom panel contrasts the total energy variations by the two schemes in zoom view. The total energy by the ADI scheme stays visibly flat whereas the one by Sielecki's scheme appears to have a relatively large fluctuation. In fact, both schemes causes the total energies to fluctuate, but the fluctuation amplitude is 0.01% of the initial total energy with the ADI scheme, and 2.90% with Sielecki's scheme. For the linear dynamic system in question, actually there is a numerical scheme, known as Crank-Nicolson scheme, and can be proved to conserve the total energy perfectly (see Durran, 1999, page 158). However Crank-Nicolson is too expensive to use. The involved matrix inversion will not be as easy as inversions of the lower and upper triangle matrices involved in the ADI method. The ADI scheme balances the computational accuracy and efficiency nicely, and it is therefore adopted for this study.

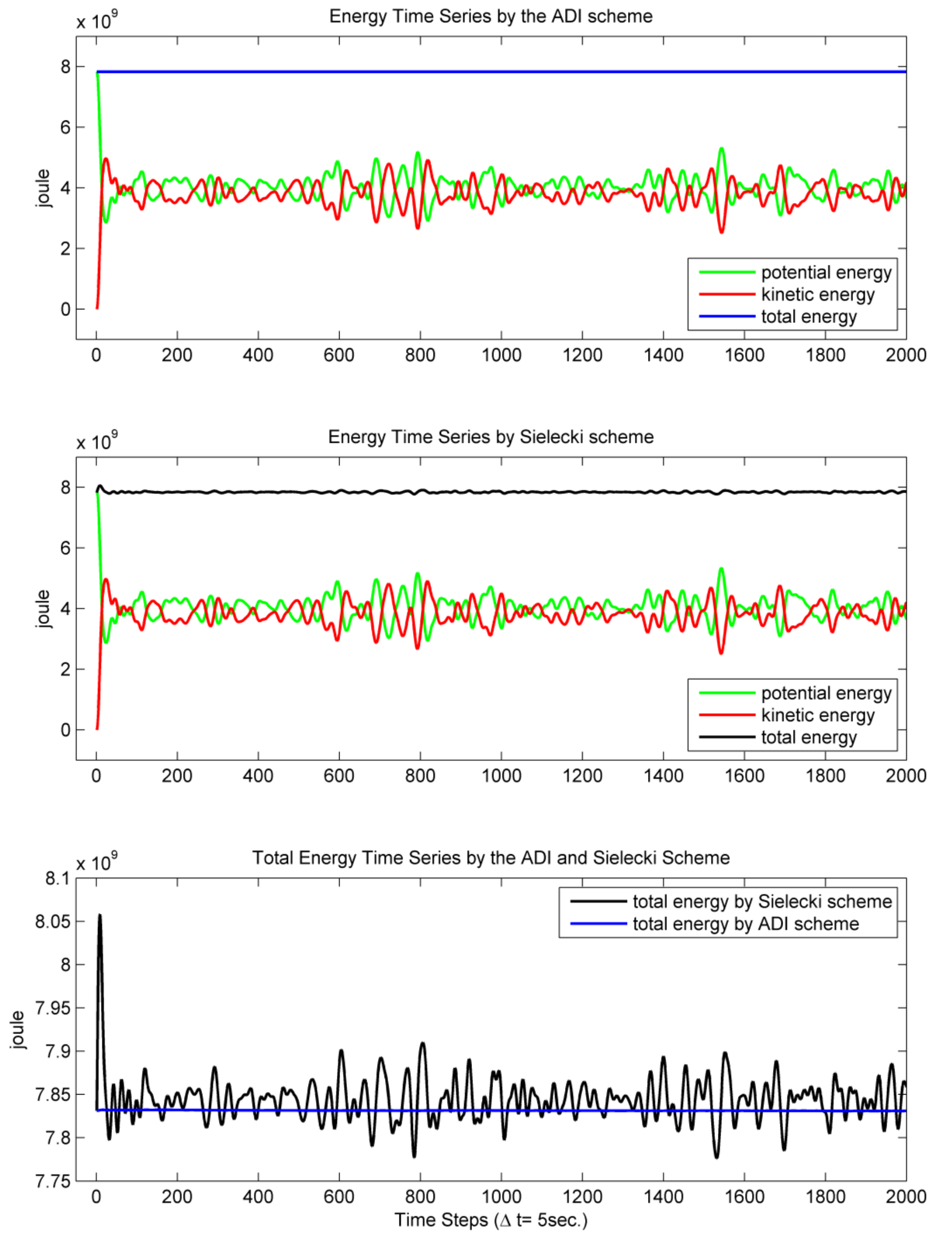

Figure 2-7 Comparison of conversation of the total energy by the ADI and Sielecki's schemes in an initial value problem. The top and middle panels show the variations of the potential and kinetic energies and the total energies with time for the ADI and Sielecki's schemes respectively. The bottom panel contrasts the fluctuations of the total energies by the schemes in a zoomed view. The ADI scheme conserves the total energy much better than the Sielecki's scheme.

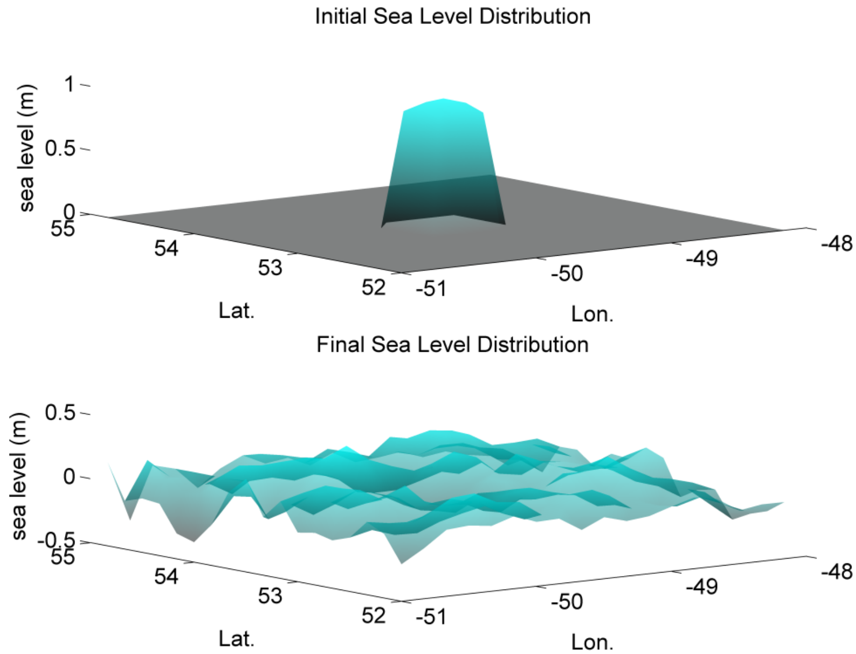

Figure 2-8 A relaxation experiment: top panel is the initial sea level distribution and the bottom panel is the distribution at time step of 2000 with $\Delta t = 5\sec$.

2.1.9 Appendix B: Algorithm to Compute the ASGF with the ADI scheme

The algorithm shown by Eqs. (2-13) and (2-14) needs to be adapted for the ADI scheme. The ADI scheme results in the matrix $\mathbf{A}$ composed of 6 factor matrices, as shown by Eq. (2-43). As commented above, we should not multiply out the product of the factor matrices. Also due to presence of inverses of the factor matrices, a left row vector multiplies with a right matrix becomes not possible. We need to do a matrix transpose first. Transpose both sides of Eqs. (2-13) and (2-14), we can have

$$\mathbf{c}_{j+1} = \mathbf{R_a}^{\mathbf{T}}(\mathbf{L_a}^{\mathbf{-T}}(\mathbf{U_a}^{\mathbf{-T}}(\mathbf{R_b}^{\mathbf{T}}(\mathbf{L_b}^{\mathbf{-T}}(\mathbf{U_b}^{\mathbf{-T}}\mathbf{c_j}))))), \qquad (\mathrm{j}=0,1,2,\cdots,\mathrm{j}_{max}) \quad (2\text{-}46)$$

$$\mathbf{c}_0(\mathrm{i}) = \begin{cases} 0, & \text{i for all the grid points except for the } nth \\ 1, & i = n. \end{cases} \quad (2\text{-}47)$$

where Eq. (Eq. 2-43) has been substituted in,

$$\mathbf{c} \quad \equiv \quad \mathbf{r}^{\mathbf{T}} \tag{2-48}$$

and $\mathbf{L_a}^{\text{-}\mathbf{T}}$, for example, is short for $(\mathbf{L_a}^{\mathbf{T}})^{-1}$. Once all the $\mathbf{c}_{j+1}$ (j=0,1,2,$\cdots$, j_{max}) are calculated, we can transpose them to make the row vectors $\mathbf{r}_{i+1}$ (i=0,1,2,$\cdots$,i_{max}) and stack them to make the ASGF matrices, $\mathbf{G_i}$ and $\mathbf{G_c}$ as shown by Eqs. (2-15) and (2-16).

2.1.10 Appendix C: Matlab Functions to Calculate the ASGF matrices of $\mathbf{G_i}$ and $\mathbf{G_c}$

This appendix gives two Matlab functions to calculate the $\mathbf{G_i}$ and $\mathbf{G_c}$ matrices defined by Eqs. (2-15) and (2-16). The function `ASGF_ini` in Table 2-1 calculates $\mathbf{G_i}$, whereas the function `ASGF_conv` in Table 2-2 calculates $\mathbf{G_c}$. These two functions assume that the dynamics matrix $\mathbf{A}$ has been made explicitly available. If the dynamics matrix $\mathbf{A}$ is given as a product of several factor matrices, some of which may involve inversions, the codes need to be modified according to the algorithm given in Appendix B.

The coding for `ASGF_ini` follows the algorithm shown by Eqs. (2-13), (2-14) and (2-15). However not all the row vectors $\mathbf{r}$ are recorded into the matrix $\mathbf{G}$. A decimating factor d is used to record only a subset of the row rectors. As explained in paragraph after Eq.(2-20), the Δt associated with the index i is set internally by the model of Eq. (2-9). It is a small value. Let us assume it is 5 seconds. For an initial value like tsunami problem, it may be sufficient to resolve the solutions in one minute. From 5 seconds to 1 minute, there is a factor 12 to decimate the row vectors before they are recorded into $\mathbf{G}$. Line 19 assumes this decimation. Other lines of the function should be self-evident.

The code for `ASGF_conv` is mostly the same as that for `ASGF_ini`. However there is an important difference. In `ASGF_conv`, what is recorded into the matrix $\mathbf{G}$ is not the row vectors themselves, but the sums of their subsets. The sums are needed because the atmospheric forcing vectors are usually given by a much larger time step than the time step required by the surge model. To give a simple example, let $k_{max} = 5$ in Eq. (2-12) and drop off the initial condition term, we have

$$\eta^{(k+1)} = \sum_{i=0}^{k} \mathbf{r}_i \mathbf{f}^{(k-i)}, \quad (k = 0, 1, 2, 3, 4, 5)\ . \qquad (2\text{-}49)$$

Expand it so that we can see it more concretely,

$$\begin{bmatrix} \eta^{(1)} \\ \eta^{(2)} \\ \eta^{(3)} \\ \eta^{(4)} \\ \eta^{(5)} \\ \eta^{(6)} \end{bmatrix} = \begin{bmatrix} \mathbf{r}_0 & & & & & \\ \mathbf{r}_1 & \mathbf{r}_0 & & & & \\ \mathbf{r}_2 & \mathbf{r}_1 & \mathbf{r}_0 & & & \\ \mathbf{r}_3 & \mathbf{r}_2 & \mathbf{r}_1 & \mathbf{r}_0 & & \\ \mathbf{r}_4 & \mathbf{r}_3 & \mathbf{r}_2 & \mathbf{r}_1 & \mathbf{r}_0 & \\ \mathbf{r}_5 & \mathbf{r}_4 & \mathbf{r}_3 & \mathbf{r}_2 & \mathbf{r}_1 & \mathbf{r}_0 \end{bmatrix} \begin{bmatrix} \mathbf{f}^{(0)} \\ \mathbf{f}^{(1)} \\ \mathbf{f}^{(2)} \\ \mathbf{f}^{(3)} \\ \mathbf{f}^{(4)} \\ \mathbf{f}^{(5)} \end{bmatrix} \qquad (2\text{-}50)$$

where the omitted elements in the upper triangle of the matrix are all zero. Assume that the forcing vector varies with every three time steps, i.e., $\mathbf{f}^{(0)} = \mathbf{f}^{(1)} = \mathbf{f}^{(2)}$ and $\mathbf{f}^{(3)} = \mathbf{f}^{(4)} = \mathbf{f}^{(5)}$. Also assume that we wish only to retain the solutions at every three steps too, then the above equation can be reduced to

$$\begin{bmatrix} \eta^{(3)} \\ \eta^{(6)} \end{bmatrix} = \begin{bmatrix} \mathbf{r}_0 + \mathbf{r}_1 + \mathbf{r}_2 & \mathbf{0} \\ \mathbf{r}_3 + \mathbf{r}_4 + \mathbf{r}_5 & \mathbf{r}_0 + \mathbf{r}_1 + \mathbf{r}_2 \end{bmatrix} \begin{bmatrix} \mathbf{f}^{(0)} \\ \mathbf{f}^{(3)} \end{bmatrix}\ . \qquad (2\text{-}51)$$

As we can see, because the forcing vector varies with every three time steps, we can have reduced a 6×6 matrix to a 2×2 matrix. The elements in the lower triangle of the reduced matrix are sums of every three row vectors, i.e., $\mathbf{r}_0 + \mathbf{r}_1 + \mathbf{r}_2$ and $\mathbf{r}_3 + \mathbf{r}_4 + \mathbf{r}_5$. That is how the sums of the row vectors come into play. In this simple example, the decimating factor *d* is 3. For a realistic case, let us assume Δt required by the surge model is 5 seconds whereas the atmospheric forcing vectors are given by hourly. From 5 seconds to 3600 seconds, there is a big factor of 720 to lump over the row vectors and to reduce the size of the matrix $\mathbf{G}$. In the function, the vector $\mathbf{g}$ holds the accumulation of the $\mathbf{r}$ vectors. The $\mathbf{g}$ is periodically (every *d* steps) recorded into the matrix $\mathbf{G}$ and then renewed to the current value of the $\mathbf{r}$ vector before it starts a new round of accumulation. The recording and the renewal is done in Line 29 and the accumulation is done in line 31. The last two optional inputs to the function are $\mathbf{B}$ and $\mathbf{L}$ which are introduced in Eqs. (2-7) and (2-22) respectively. If they are inputted, the vector $\mathbf{g}$ will be multiplied by $\mathbf{BL}$ before it is recorded into $\mathbf{G}$. This way, the columns of $\mathbf{G}$ can be reduced if $\mathbf{L}$ is a tall and thin matrix.

```
function G = ASGF_ini(A, n, imax, d)
% To calculate the ASGF matrix for the initial value problem.
%
% Inputs: A,  the dynamic matrix; it should be a square matrix.
%         n,  the nth grid point (POI, point of interest).
%      imax,  the max iteration number.
%         d,  an integer decimating factor (>=1) to record the
%             row-vectors of the powers of A into G.
%
% Output: G, the ASGF matrix for the POI.
%

N=size(A,2); r=zeros(1,N); r(n)=1; M=ceil(imax/d);
G=zeros(M,N);   % pre-allocate memory for G

m=0;
for i=1:imax+1
    r=r*A;
    if mod(i,d)==0
       m=m+1; G(m,:)=r;
    end
end
G=G(1:m,:);
end  % end of the function
```

Table 2-1. A Matlab function, `ASGF_ini`, to calculate the ASGF matrix $\mathbf{G_i}$ for the initial value problem.

```matlab
function G = ASGF_conv(A, n, imax, d, B, L)
% To calculate the ASGF matrix for the forced problem.
%
% Inputs: A,     the dynamic matrix; it should be a square
%                matrix.
%         n,     the nth grid point (POI, point of interest).
%         imax,  the max iteration number.
%         d,     an integer decimating factor (>=1) to record the
%                row-vectors of the powers of A into G.
%         B,     optional input, for mapping the external force
%                into the momentum to change the state vector of
%                the system.
%         L,     optional input, which interpret the forcing
%                field as given to the grid used by the dynamic
%                system.
% Output: G, the ASGF matrix for the POI.
%
N=size(A,2); r=zeros(1,N); r(n)=1; g=r; M=ceil(imax/d);

if nargin==5, BL=B;   N=size(BL,2); end
if nargin==6, BL=B*L; N=size(BL,2); end
G=zeros(M,N);   % pre-allocate memory for G

m=0;
for i=1:imax+1
    r=r*A;
    if mod(i,d)==0
       if nargin>=5, g=g*BL; end
       m=m+1; G(m,:)=g; g=r;
    else
       g=g+r;
    end
end
G=G(1:m,:);
end  % end of the function
```

Table 2-2 A Matlab function, `ASGF_conv`, to calculate the ASGF matrix $\mathbf{G}_c$ for the forced problem.

2.1.11 Appendix D: Convolution of Matrices, conv_F

In this paper, the rows of the matrix $\mathbf{G}$ are arranged with the time-indices, and its columns are arranged with the space-indices. Let us introduce another matrix, $\mathbf{F}$, with the same row and column arrangement, to hold the forcing vectors at different times

$$\mathbf{F} = \left[\mathbf{f}^{(0)}\ \mathbf{f}^{(1)} \cdots \mathbf{f}^{(\mathrm{k})} \cdots \mathbf{f}^{(\mathrm{k}_{max})}\ \right]^{\mathrm{T}} \qquad (\ 2\text{-}52)$$

Thus, the time-varying information of the forcing field is contained in the columns and the space-varying information is contained in the rows. To let $\mathbf{F}$ and $\mathbf{G}$ shear the same row and column arrangement allows us to extend the commutative property of convolution from vector operands to matrix operands. This is to say the following relation holds when both $\mathbf{F}$ and $\mathbf{G}$ are matrices,

$$\mathbf{G} * \mathbf{F} = \mathbf{F} * \mathbf{G}. \qquad (\ 2\text{-}53)$$

In many text books, this property is proved for the two scalar operands. It actually holds when the two operands are vector functions of time. A vector function of time becomes a matrix when it is discretized in time. The proof of this property for the matrix case is not difficult and nor lengthy, so let it be included here for convenience in reference.

With $\mathbf{F}$ introduced by Eq. (2-52), the convolution definition given by Eq. (2-18) **Error! Reference source not found.** can be re-expressed as

$$(\mathbf{G} * \mathbf{F})^{(k+1)} \equiv \sum_{i=0}^{k} \mathbf{G}(i+1,:)\mathbf{F}^{T}(:,k-i+1), \qquad (k = 0,1,2,\cdots,k_{max})\,. \qquad (\ 2\text{-}54)$$

The above can be further transformed as

$$(\mathbf{G} * \mathbf{F})^{(k+1)} = \sum_{m=0}^{k} \mathbf{G}(\mathrm{k}-\mathrm{m}+1,:)\mathbf{F}^{\mathrm{T}}(:,m+1) \qquad \text{let } m = k-i \qquad (\ 2\text{-}55)$$

$$= \sum_{m=0}^{k} \mathbf{F}(m+1,:)\mathbf{G}^{\mathrm{T}}(:,k-m+1) \qquad \text{exchange the positions of } \mathbf{G} \text{ and } \mathbf{F}^{\mathrm{T}} \text{ with their transposes} \qquad (\ 2\text{-}56)$$

$$= (\mathbf{F} * \mathbf{G})^{(k+1)} \qquad \text{according to the definition by Eq. (2-54).} \qquad (\ 2\text{-}57)$$

for any $k = 0, 1, 2, \cdots, k_{max}$. Thus, Eq. (2-53) is proved. One may also view Eq.(2-54) and Eq. (2-56) as the equivalent definitions of convolution. Note the result of the convolution as defined above is a vector when all when all the k's are taken.

With the matrix $\mathbf{F}$ as introduced above, Eq. (2-20) can be re-expressed as

$$\boldsymbol{\eta} = \mathbf{G} * \mathbf{F}. \qquad (2\text{-}58)$$

where the subscript 'c' of $\mathbf{G}$ has been dropped off. To give this formula a concrete look, let us assume, without loss of generality, that there are only two rows in $\mathbf{G}$ and three rows in $\mathbf{F}$, i.e., $\mathbf{G} = [\mathbf{r}_0; \mathbf{r}_1]$ and $\mathbf{F} = \left[\mathbf{f}^{(0)}\ \mathbf{f}^{(1)}\ \mathbf{f}^{(2)}\right]^{\mathrm{T}}$. For this simple case, according to the definition given in Eq. (2-55), we can write Eq. (2-58) as

$$\begin{bmatrix} \eta_1 \\ \eta_2 \\ \eta_3 \\ \eta_4 \end{bmatrix} = \begin{bmatrix} \mathbf{r}_0 \\ \mathbf{r}_1 \\ \boldsymbol{\theta} \\ \boldsymbol{\theta} \end{bmatrix} \mathbf{F}^{\mathrm{T}}(:,1) + \begin{bmatrix} \boldsymbol{\theta} \\ \mathbf{r}_0 \\ \mathbf{r}_1 \\ \boldsymbol{\theta} \end{bmatrix} \mathbf{F}^{\mathrm{T}}(:,2) + \begin{bmatrix} \boldsymbol{\theta} \\ \boldsymbol{\theta} \\ \mathbf{r}_0 \\ \mathbf{r}_1 \end{bmatrix} \mathbf{F}^{\mathrm{T}}(:,3) \qquad (2\text{-}59)$$

where η_1, η_2, η_3 and η_4 are four scalars of the convolution values at four times ($t = \Delta t, 2\Delta t, 3\Delta t, 4\Delta t$, with Δt being an hour, for example). The first term on the RHS represents a train of waves set into motion by the first instantaneous forcing vector, $\mathbf{F}^{\mathbf{T}}(:,1)$. The second term is another train of waves set into motion by the second instantaneous forcing vector, $\mathbf{F}^{\mathrm{T}}(:,2)$, and similarly is the third term. Once set into motion, these trains of waves become free waves since their associated instantaneous forces no longer exist. The total response is the sum of these free trains of waves.

Because this simple example assumes that there are only three successive forces and the wave set up by each force only lasts two time steps, the length of the total response is four time steps, as shown by the number of the elements of column vector on the LHS of Eq. (2-59). Generally speaking, the length of the response vector of convolution is given by the formula

$$L_R = L_G + L_F - 1 \qquad (2\text{-}60)$$

where L_R stands for the length of the response vector, L_G stands for the length of the convolution kernel (in terms of the number of rows of $\mathbf{G}$), L_F stands for the length of the forcing (in terms of the time steps of the forcing field).

Eq. (2-59) can be also written as

$$\begin{bmatrix} \eta_1 \\ \eta_2 \\ \eta_3 \\ \eta_4 \end{bmatrix} = \begin{bmatrix} \mathbf{F}(1,:) \\ \mathbf{F}(2,:) \\ \mathbf{F}(3,:) \\ \mathbf{0} \end{bmatrix} \mathbf{r}_0^{\mathrm{T}} + \begin{bmatrix} \mathbf{0} \\ \mathbf{F}(1,:) \\ \mathbf{F}(2,:) \\ \mathbf{F}(3,:) \end{bmatrix} \mathbf{r}_1^{\mathrm{T}} \qquad (\text{2-61})$$

which is an instance of the commutative property of convolution given in Eq. (2-53). Although Eq. (2-59) and Eq. (2-61) produce the same results, they differ in that the former has three terms where the latter has two terms. If we use a *for-loop* to perform matrix-vector multiplication in each term the *for-loop* will be shorter with Eq. (2-61) than with Eq. (2-59). In Matlab, the shorter a *for-loop* is, the better the computational efficiency will be. For this simple example, the lengths of the *for-loop* differ only by 1 trivially. However, in a real application, the difference can be very big! For the real application in this paper, the number of rows in $\mathbf{G}$ is 72 and the number of forcing vectors is 744 (hourly forcing vectors, for the whole months of December, $24 \times 31 = 744$). The length of the *for-loop* with Eq. (2-59) is 774, whereas the length with Eq. (2-61) is 72. Their difference is 702. If the number of the hourly forcing vectors covers a year, the difference in the length of the *for-loop* will be 8688, which is very big!

A Matlab function, `conv_FG`, is given in Table 2-3. It implements the convolution defined by Eq. (2-56). Matlab has a built-in function, called `conv`. However it cannot be applied to matrices. The function `conv_FG` takes in two matrices, $\mathbf{G}$ and $\mathbf{F}$, and yields a response vector $\mathbf{c}$. The function will verify if $\mathbf{G}$ is shorter than $\mathbf{F}$. If this is not case, it will swap $\mathbf{G}$ and $\mathbf{F}$ before proceeding for the calculation (lines 15 to 18). Line 20 specifies the length of the response vector according to Eq. (2-60). Line 21pre-allocates the computer memory to the response vector $\mathbf{c}$. Line 22 gives an index vector *i*, which is used in the *for-loop* to synchronize the waves produced by each instance of the external forcing “kicks”. The *for-loop* given in lines 24 to 27 performs the actual calculation of the convolution. Line 25 transposes the *mth* row of $\mathbf{G}$ to be used in the next line. Eq. (2-56) suggests that $\mathbf{G}$ should be transposed before a column of $\mathbf{G}^T$ is used. However, we do not have to transpose the entire matrix. We can transpose one row per time step. This is perhaps a more efficient approach when $\mathbf{G}$ is big, since the computer then does not need to create an internal copy of $\mathbf{G}^T$. Line 26 computes the multiplication of matrix $\mathbf{F}$ with the column vector $\mathbf{g}$, and adds the results to the right places in $\mathbf{c}$ as the loop progresses.

```matlab
function c=conv_FG(G,F)
% Convolution of two matrices, G and F.
% The length of G, in terms of the number of its rows,
% is assumed shorter than the length of F. If this is not case,
% G and F will be swapped first. The output c is a column vector
% whose length is equal to the sum of the lengths of G and F
% minus 1.

size_G=size(G);  size_F=size(F);

if size_G(2)~=size_F(2)
   error('G and F must have the same columns!')
end

if size_F(1)<size_G(1)
   tmp=F; F=G; G=tmp;  % to ensure F is longer.
   size_F=size(F); size_G=size(G);
end

p=size_F(1)+size_G(1)-1; % length of the convolution vector
c=zeros(p,1);            % pre-allocate memory
i=0:size_F(1)-1;

for m=1:size_G(1)
   g=G(m,:).';           % transpose of G(m,:)
   c(m+i)=c(m+i)+F*g;    % multiplication and addition
end

end                      % end of the function
```

Table 2-3 Matlab function conv_FG

2.1.12 References

Csanady, G. T. (1982). *Circulation in the coastal ocean* (Vol. 2). Springer.

Ding, Y.; Jia Y.; ASCE, M.; Wang, S. S. Y. & ASCE, F. (2004). Identification of Manning's Roughness Coefficients in Shallow Water Flows. *Journal of Hydraulic Engineering, ASCE*, June 2004.

Durran, D. R. (1999). *Numerical methods for wave equations in geophysical fluid dynamics* (No. 32). Springer.

Heaps, N. S. (1969). A two-dimensional numerical sea model. *Philosophical Transactions for the Royal Society of London. Series A, Mathematical and Physical Sciences*, 93-137.

Leendertse, J. J. (1967). *Aspects of a computational model for long-period water-wave propagation* (p. 165). Santa Monica, California: Rand Corporation.

Sielecki, A. (1968): An Energy-Conserving Difference Scheme for the storm surge equations Mon. Wea. Rev., 96, 150-156.

Tan, W. Y. (1992). *Shallow water hydrodynamics: mathematical Theory and numerical solution for a two-dimensional system of shallow-water equations*. Elsevier.

Wesseling, P. (2009). *Principles of computational fluid dynamics* (Vol. 29). Springer Science & Business.

Xu, Z. (2007). The all-source Green's function and its applications to tsunami problems. *Science of Tsunami Hazards*, *26*(1), 59.

Xu, Z. (2011). The all-source Green's function of linear shallow water dynamic system: Its numerical constructions and applications to tsunami problems. *The Tsunami Threat-Research and Technology*, *25*.

Xu, Z., and Song, Y. T. (2013). Combining the All-Source Green's Functions and the GPS-Derived Source Functions for Fast Tsunami Predictions—Illustrated by the March 2011 Japan Tsunami. *Journal of Atmospheric and Oceanic Technology*, *30*(7), 1542-1554.

Xu Z., J-P Savard and D. Lefaivre (2014) Data Assimilative Hindcast and Climatological Forecast of Storm Surges at Sept-Iles in the Estuary of Gulf of St. Lawrence. Submitted to the *Atmosphere-Ocean*.

2.2 The All-Source Green's Function (ASGF) and its Applications to Storm Surge Modelling. Part II: From the ASGF Convolution to Forcing Data Compression and a Regression Model

Zhigang Xu

Maurice Lamontagne Institute
Fisheries and Oceans Canada, Mont-Joli, Quebec

and

Institut des Sciences de la Mer
Université du Québec à Rimouski

(This section is adapted from a manuscript submitted to Ocean Dynamics on 2014/Oct/30 and accepted on 2015/Jan/19 subjected to revisions.)

2.2.0 Abstract

In Part I of this study, a traditional storm surge model boils down to a simple convolution of an ASGF matrix with an atmospheric forcing field. This paper further develops the ASGF convolution with the singular value decompositions (SVD) and fast Fourier transform and its inverse (fft/ifft). A very simple and efficient regression model is achieved at the end, which not only can make the storm surge simulations data assimilative, but also can make the simulations millions of times faster than the traditional modelling approach.

Keywords: ASGF Convolution, SVD, FFT/IFFT, Linear Regression, Storm Surges

2.2.1 Introduction

In Part I, Xu (2014) proposed a new method to model storm surges. The new method uses the all-source Green's function (ASGF). The ASGF comes as a matrix and can be pre-calculated from a storm surge model. Each column of the ASGF matrix is a Green's function corresponding to an impulse force at a grid point and there are as many such columns as the total number of model grid points. A traditional complicated storm surge model then boils down to a simple convolution,

$$\boldsymbol{\eta} = \mathbf{G} * \mathbf{f} \tag{2-62}$$

where $\mathbf{G}$ is the ASGF matrix and $\mathbf{f}$ is the atmospheric forcing field (cf. Eq. 2-20). With this ASGF convolution we can perform storm surge simulations for a point of interest (POI) thousands of times faster than with the traditional modelling approach. The fast speed does not compromise the quality of simulation. Rather, it should be better given that the ASGF convolution accounts for the influences and is free of artificial open water boundary effects. Most traditional storm surge models are regional and hence their solutions have to bear influences of artificial open water boundary conditions to various degrees. Part I showed a realistic test case where a whole month of hourly time series of $\boldsymbol{\eta}$ was simulated. It only took 45 seconds to finish the simulation, of which 33 seconds were used to retrieve the atmospheric forcing data from the disk; the ASGF convolution itself consumed only 12 seconds. The simulation accounted for 82% of the variance of the observation without any data assimilations.

The simplicity of the ASGF convolution opens a door to many other mathematical operations. This paper further develops the ASGF convolution with the singular value decompositions (SVD) and fast Fourier transform and its inverse (fft/ifft). As we will see, we can end up with a simple and very efficient regression model, which can make the storm surge simulations not only data assimilative, but also millions times faster than the traditional modelling approach.

2.2.2 Singular Value Decomposition (SVD) and Forcing Data Compression

The matrix $\mathbf{G}$ is short and wide for a realistic case. Its number of rows equals the number of time steps we want to record the row vectors $\mathbf{r}_i$ (cf. Eqs. 2-13 and 2-14). Its number of columns equals to the number of grid points where the atmospheric forcing vector is defined. For the realistic test case presented in Part I, $\mathbf{G}$ has 72 rows and 408,622 columns, which is indeed very short and wide.

The short and wide characteristic of $\mathbf{G}$ implies that there is a huge null space that can be squeezed out, for the sake of computational efficiency and for data assimilations as well. The singular value decomposition (SVD) is good for finding such a null space. Let us apply SVD to $\mathbf{G}$

$$\underset{72\times408622}{\mathbf{G}} = \underset{72\times72}{\mathbf{U}} \begin{bmatrix} \underset{72\times72}{\mathbf{S}} & \underset{72\times408550}{\mathbf{0}} \end{bmatrix} \begin{bmatrix} \underset{72\times408622}{\mathbf{V}^T} \\ \underset{408550\times408622}{\mathbf{V}_2{}^T} \end{bmatrix} \quad (2\text{-}63)$$

where $\mathbf{U}$ and $[\mathbf{V}\ \ \mathbf{V}_2]$ are unitary matrices (i.e., $\mathbf{U}^T\mathbf{U} = \mathbf{U}\mathbf{U}^T = \mathbf{I}$ and $[\mathbf{V}\ \mathbf{V}_2]^T[\mathbf{V}\ \mathbf{V}_2] = [\mathbf{V}\ \mathbf{V}_2][\mathbf{V}\ \mathbf{V}_2]^T = \mathbf{I}$, where each $\mathbf{I}$ is an identity matrix with its appropriate dimensions understood), $\mathbf{S}$ is a diagonal matrix with non-negative real numbers on the diagonal, known as the singular values of $\mathbf{G}$. Besides $\mathbf{S}$ in the middle is a zero matrix, which makes $\mathbf{V}_2$ contribute null to $\mathbf{G}$. The null space of $\mathbf{G}$ is found. It is spanned by the columns of $\mathbf{V}_2$.

The singular values of $\mathbf{G}$ are arranged in a descending order. They regulate the importance of the input modes, since the compressed forcing vector $\mathbf{V}^\mathbf{T}\mathbf{f}$ is multiplied by $\mathbf{S}$ as by Eq. (2-66). Shown in Figure 2-9 are singular values of $\mathbf{G}$ for Sept-Iles, a POI for the realistic test case chosen in Part I. Those values larger than 1 (there are 39 of them) will amplify the effects of the corresponding forcing components, whereas those less than 1 (there are 33 of them) will reduce the effects. The figure also annotates a ratio of the last singular value versus the first singular value, which is 0.0019 and means that significance of mode 72 is less than 0.2% as that of mode 1. In retrospect, this may justify the cut off at 72 hours in pre-calculation of the matrix $\mathbf{G}$.

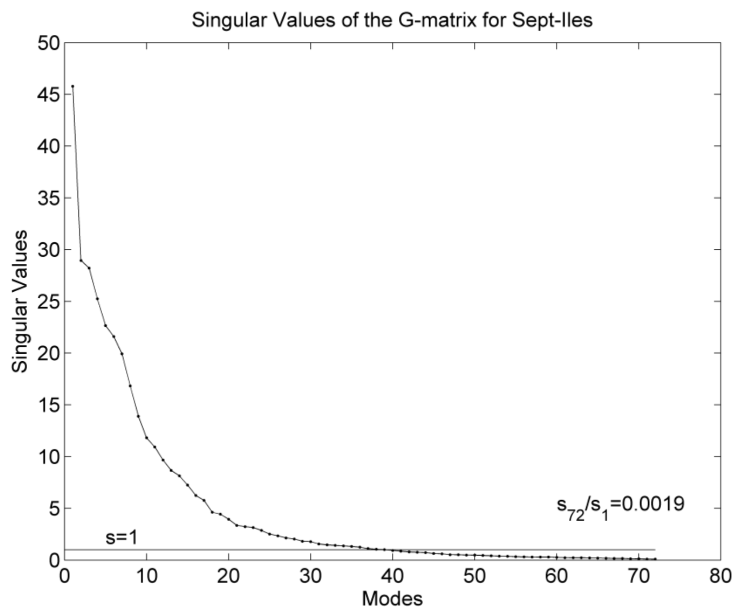

Figure **2-9** Singular values of the ASGF matrix, $\mathbf{G}$, at Sept-Iles.

Because $\mathbf{V}_2$ contributes null to $\mathbf{G}$, it can be squeezed out from the SVD decomposition. In general, when $\mathbf{G}$ has dimensions of $m \times n$ we can always decompose it as

$$\underset{m\times n}{\mathbf{G}} = \underset{m\times m}{\mathbf{U}} \; \underset{m\times m}{\mathbf{S}} \; \underset{m\times n}{\mathbf{V}^T} \qquad (2\text{-}64)$$

with $m < n$ (which is not required by the SVD itself, however is appropriate in this study). With the above SVD decomposition, Eq. (2-62) can be written as

$$\boldsymbol{\eta} = (\mathbf{USV}^T) * \mathbf{f} \qquad (2\text{-}65)$$

The following relation can be proved,

$$(\mathbf{USV}^T) * \mathbf{f} = (\mathbf{US}) * (\mathbf{V}^T\mathbf{f}) = \mathbf{U} * (\mathbf{SV}^T\mathbf{f}). \qquad (2\text{-}66)$$

In fact, following the convolution definition as of Eq. (2-18), we can prove the above relations by *parentheses:*

$$[(\mathbf{USV}^T) * \mathbf{f}]^{(k+1)} \equiv \sum_{i=0}^{k} (\mathbf{U}(i+1,:)\mathbf{SV}^T)\mathbf{f}^{(k-i)} \qquad (2\text{-}67)$$

$$= \quad \sum_{i=0}^{k} (\mathbf{U}(i+1,:)\mathbf{S})(\mathbf{V}^T \mathbf{f}^{(k-i)}) \equiv [(\mathbf{US}) * (\mathbf{V}^T \mathbf{f})]^{(k+1)} \qquad (2\text{-}68)$$

$$\overset{or}{=} \quad \sum_{i=0}^{k} \mathbf{U}(i+1,:)(\mathbf{SV}^T \mathbf{f}^{(k-i)}) \equiv [(\mathbf{U} * (\mathrm{S}\,\mathbf{V}^T \mathbf{f})]^{(k+1)} \qquad (2\text{-}69)$$

where $k = 0,1,2,\cdots$. Thus the relationship is proved.

Define

$$\underset{m\times 1}{\boldsymbol{\psi}} = \underset{m\times n}{\mathbf{V}^{\mathbf{T}}} \ \underset{n\times 1}{\mathbf{f}} \qquad (2\text{-}70)$$

The $\boldsymbol{\psi}$ is a compressed forcing vector. Its dimension is $m \times 1$. Take the above mentioned matrix $\mathbf{G}$ with dimensions of 72×408622 as example. This $\mathbf{G}$ matrix implies that forcing vector $\mathbf{f}$ has 408,622 elements. Now the compression can make it a much shorter one, with 72 elements only. The compression rate is 5675 times. This is a huge data compression and results in three benefits:

Firstly, the compression facilitates to store the forcing data. For example, the global MERRA atmospheric data from 1979 to 2013 occupies a 400 GB disk space. The compression reduces the size of this dataset to 72 MB per POI. If we have 1000 POIs, which is perhaps a quite large number practically, the total disk space to store the compressed forcing data is 70 GB. Nowadays, one can easily store a 70 GB dataset in a portable computer.

Secondly, the compression makes the retrieval of the forcing data from the disk files much faster. The disk data retrieval is often a bottle neck controlling the simulation speed. It was reported in Part I, to retrieve a month of hourly MERRA forcing data, it took 33 seconds whereas to compute the ASGF convolution itself only takes 12 seconds. Now with the compressed forcing, the time used for the disk data retrieval is 0.022 seconds and the time used to compute the ASGF convolution is 0.004 seconds. The speed of data retrieval is enhanced by more than 1500 times. The data retrieval enhancement will become even better when longer periods of data are retrieved. Of course, to compress the forcing data itself takes time. However, what really takes time for the compression is to retrieve the original forcing data from the disk. Once the forcing vector $\mathbf{f}$ is loaded into the computer RAM, it can be used for the compressions for all the POIs. Different POIs have different $\mathbf{V}$ matrices, but they all share the same $\mathbf{f}$ for compression.

The forcing data compression only needs to be performed once, but can benefit all the subsequent computations.

Thirdly, the compression makes the convolution much faster. With the compressed forcing vector, Eq. (2-65) can be simplified as

$$\boldsymbol{\eta} = (\mathbf{US}) * \boldsymbol{\psi} \overset{or}{=} \mathbf{U} * (\mathbf{S}\boldsymbol{\psi})\,. \tag{2-71}$$

The simplification means there are much less numbers to compute with. From 12 seconds to 0.004 seconds as mentioned above, the speed of the convolution computation is increased 3000 times.

Accounting for the time taken for the disk data retrievals and for the convolution computations together, it takes 45 seconds using Eq. (2-65) and 0.026 seconds using Eq. (2-71), the enhancement of the simulation speed is more than 1700 times. Recall from Part I that the 45 seconds with Eq. (2-62) was already 1,500 times faster than the traditional modelling approach; the total speed-up due to the combination of the ASGF and SVD is 1555×1700 times. This speed-up of millions of times makes long term simulations very easy. Table 2-4 shows that a 10 year long simulation of hourly storm surges can be finished in about 0.5 seconds.

```
t=(datenum(2000,1,1):1/24:datenum(2009,12,31,23,59,59)).';
tic
psi=POI.get_forcing_svd(t, 1, true);
z=conv_FG(US,psi);
toc
Elapsed time is 0.492306 seconds.
```

Table 2-4 The SVD compression of forcing data results in a very fast simulation of storm surges. The time elapsed in the simulation of a 10 year hourly storm surges at a POI is recorded. It takes only 0.49 seconds to finish the simulation.

2.2.3 From the ASGF Convolution to a Regression Model

Appendix A proves the following relation is true.

$$\mathbf{U} * (\mathbf{S}\boldsymbol{\psi}) = \begin{bmatrix} \mathbf{U}_1 * \boldsymbol{\psi}_1 & \mathbf{U}_2 * \boldsymbol{\psi}_2 & \cdots & \mathbf{U}_\mathbf{j} * \boldsymbol{\psi}_\mathbf{j} & \cdots & \mathbf{U}_\mathbf{m} * \boldsymbol{\psi}_\mathbf{m} \end{bmatrix} \mathbf{s} \tag{2-72}$$

Substituting this relation into Eq. (2-71), we have

$$\boldsymbol{\eta} = \begin{bmatrix} \mathbf{U}_1 * \boldsymbol{\psi}_1 & \mathbf{U}_2 * \boldsymbol{\psi}_2 & \cdots & \mathbf{U}_m * \boldsymbol{\psi}_m \end{bmatrix} \mathbf{s}\,. \tag{2-73}$$

Introducing a new matrix $\mathbf{C}$

$$\mathbf{C} = \left[\mathbf{U}_1 * \boldsymbol{\psi}_1 \quad \mathbf{U}_2 * \boldsymbol{\psi}_2 \quad \cdots \quad \mathbf{U}_m * \boldsymbol{\psi}_m\right] \tag{2-74}$$

we can express Eq. (2-73) as

$$\boldsymbol{\eta} = \mathbf{C}\,\mathbf{s} \tag{2-75}$$

Appendix A also discusses how to use the fast Fourier transfer (FFT) and its inverse (IFFT) to evaluate the $\mathbf{C}$ matrix quickly. The appendix also provides a Matlab function, `conv_FFT`, for the evaluation. To evaluate the $\mathbf{C}$ matrix with 10 years of hourly forcing field, it only takes 1 second.

By admitting an error term, $\boldsymbol{\varepsilon}$, which may consist of errors from the observations, the forcing data, and the model itself, we can cast the above equation to a regression model

$$\boldsymbol{\eta} = \mathbf{C}\,\mathbf{s} + \boldsymbol{\varepsilon} \tag{2-76}$$

where $\mathbf{s}$ should now be viewed as a vector of regression parameters. For the real case example, the $\mathbf{G}$ matrix has dimensions of 72×408622, which means there are 72 parameters in $\mathbf{s}$. They initially come from the surge model through the SVD of $\mathbf{G}$. Now they can be relaxed from the given values for best fit to the observations. If there are at least 72 observation points, denoted as $\boldsymbol{\eta}_o$, the least square fitting parameters, $\hat{\mathbf{s}}$, are given by

$$\hat{\mathbf{s}} = (\mathbf{C}^T\mathbf{C})^{-1}\mathbf{C}^T\boldsymbol{\eta}_o \tag{2-77}$$

and the least square fitted solution, $\hat{\boldsymbol{\eta}}$, is given by

$$\boldsymbol{\eta} = \mathbf{C}\hat{\mathbf{s}} \tag{2-78}$$

(e.g., Strang, 1986; Strang 2007; Seber and Lee 2003).

Part I of this study showed a simulation of storm surges at Sept-Iles for the whole month of December 2010. The simulation was performed without data assimilation. The γ^2 -value, which measures the misfits between the simulations and the observations (see Eq. 2-26 for its definition), is 0.18. Now let us see if the regression model Eq. (2-76) can further reduce the misfits. Shown in the top panel of Figure 2-10 is the simulation without data assimilation, which is copied from Figure 5 from Part I for an easy comparison. Shown on the bottom panel of Figure 2-10 is a simulation with data assimilation from regression analysis of Eqs. (2-76) and (2-78) . As we can see, the data assimilation greatly improves the fitting between the simulation (in red) and the observation (in black). The γ^2 value is reduced down to 0.05. This means that 95% of the observed variance is accounted for by the simulation.

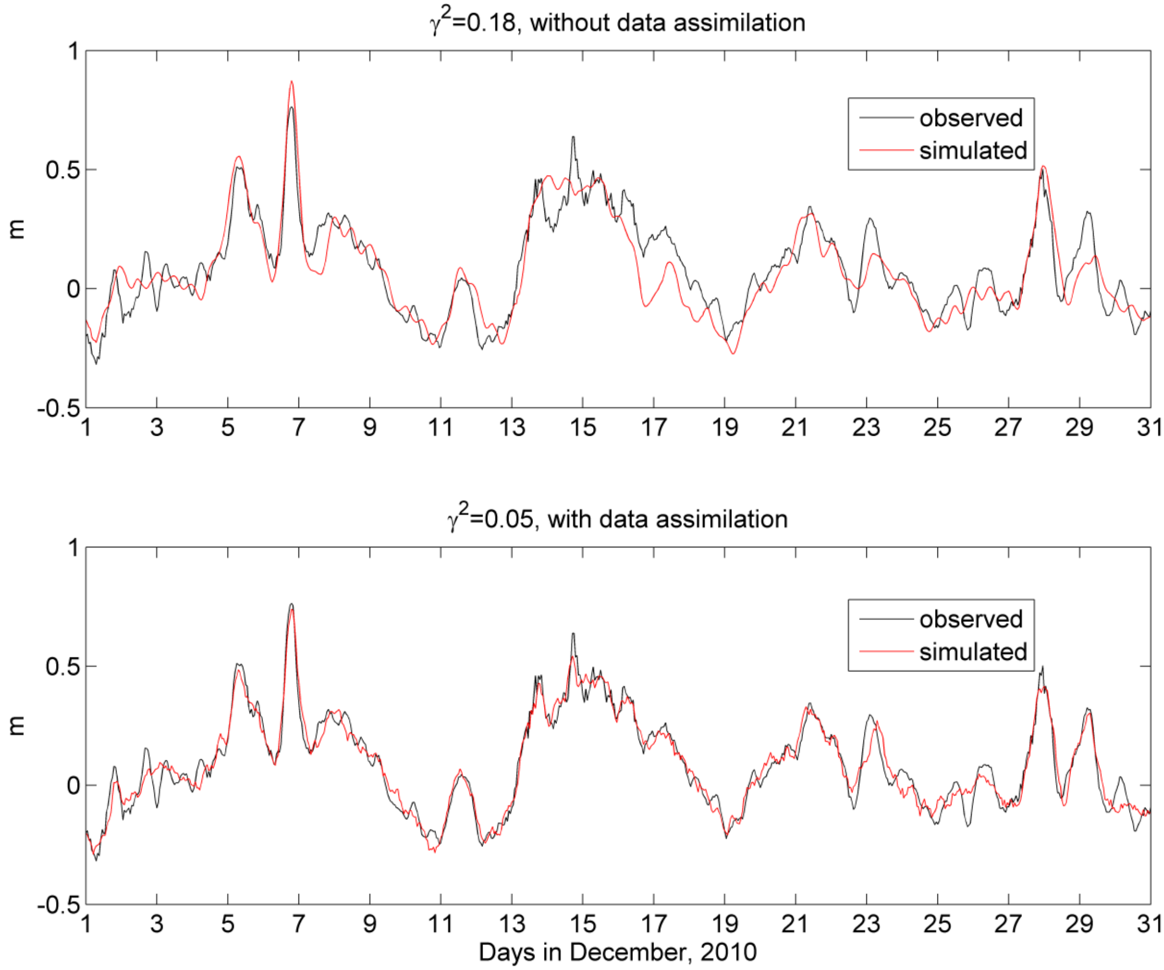

Figure 2-10 Comparisons of the simulations (in red) of storm surges against the observations (in black) at Sept-Iles for the month of December 2010. The simulation shown in the top panel is obtained without data assimilation, whereas the simulation in the bottom panel is obtained with data assimilation. The value of γ^2 shown in each panel measures the overall misfit between the observation and the simulation. There are 744 hourly data points in each time series.

2.2.4 Summary and Discussions

Starting with the ASGF convolution of Eq. (2-62), this paper proposed to apply the SVD decomposition to the ASGF matrix $\mathbf{G}$ so that a huge null space could be squeezed out and the forcing data greatly compressed. The forcing data compression not only results in small sizes of forcing data for storing and retrieving, but also speeds up computations. Through the SVD decomposition, Eq. (2-62) is simplified to Eq. (271). Eq. (2-62) can already speed up storm surge simulations 1,550 times compared with the traditional modelling approach. Now Eq. (2-71) can further speed up by another factor of 1,700. Therefore with Eq. (2-71), the simulations can proceed millions of times faster than the traditional method.

The application of SVD further leads to data assimilation. The singular vales can be moved from the middle of the three factor matrices to the right, making it possible to relax the singular values that are being given by the surge model to those which are best adjusted by the observations. Eq. (2-71) is further cast to a regression model as of Eq. (2-76). The power of the regression model to best fit between the simulations and the observations is well demonstrated. The whole month of hourly storm surges in December 2010 at Sept-Iles were simulated in Part I without data assimilation and the γ^2 value, which measures the overall misfits, was 0.18. Now with the data assimilation by Eq. (2-76), the γ^2 is reduced to 0.05.

Whether 95% of the variances of the observed de-tided signals should indeed all be attributed to atmospheric forcing is another question and is perhaps worthy of further investigation. The main point of this paper is to boil down the traditional complicated storm surge modelling to a very simple regression model that can easily conduct various regression analyses. The method demonstrated in this paper is not the only method. For example, a weighting matrix could be multiplied to both sides of Eq. (2-76) to let the large data have greater weighting when it comes to determining the least square solutions. Large data are perhaps more likely caused by storms than small ones. There could be three $\mathbf{C}$ matrices in Eq. (2-76), and three sets of $\mathbf{s}$ regression parameter vectors accordingly, one for the air pressure forcing and the other two for the two wind stress components. As it is written in Eq. (2-76), the three forcing components have been all fabricated into the same $\mathbf{C}$. Given that the forcing data from an atmospheric model contain errors, it may be worthwhile to apply the regression model simulations of tides. The tide generating forcing can be very accurately calculated. This way, the regression analyses will be free of the forcing errors, which may help us understand better the characteristics of the responses at a POI. Explorations along these lines will be reported in the future.

Due to its extremely fast simulation speed and data assimilative capability, the ASGF regression model of Eq. (2-76) provides an effective tool for a long term hindcast and forecast. With the observations and realistic atmospheric forcing in the past, the hindcast can yield the best estimated model parameter vector $\hat{\boldsymbol{\varepsilon}}$. With the best estimated $\hat{\boldsymbol{\varepsilon}}$ and with a set of climate model solutions for the future that can be used as the atmospheric forcing, we can *climatologically forecast* the storm surges. Xu et al (2014) has taken this approach and produced storm surges at Sept-Iles for the next one hundred years, which can provide a database for further statistical analysis, such as extreme value analysis.

2.2.5 Acknowledgement

This study was partially supported by le Ministère des Transports du Québec, and by the ACCASP program of Department of Fisheries and Oceans. This study also benefited from the collaborations with the OURANOS Consortium[9]. The free access to the MERRA data made by NASA is also greatly appreciated. The author also would like to gratefully acknowledge the supports from his own institute.

2.2.6 Appendix A: Columnwise Convolutions of Two Matrices, conv_FFT

The following relationship is true and can be proved from the convolution definition given by Eq. (2-18) in Part I.

$$\mathbf{U} * (\mathbf{S}\boldsymbol{\psi}) = \begin{bmatrix} \mathbf{U}_1 * \boldsymbol{\psi}_1 & \mathbf{U}_2 * \boldsymbol{\psi}_2 & \cdots & \mathbf{U}_\mathbf{m} * \boldsymbol{\psi}_\mathbf{m} \end{bmatrix} \mathbf{s} \tag{2-79}$$

where $\mathbf{s} = [s_1\ s_2\ \cdots s_m]^T$, $\mathbf{U_j}$ is the *jth* column of $\mathbf{U}$, and $\boldsymbol{\psi}_\mathbf{j} = [\psi_j^{(0)}\ \psi_j^{(1)} \cdots \psi_j^{(k_{max})}]^T$ is a column vector consisting of the time series of ψ_j , with $j = 1, 2, \cdots, m$.

To prove it, let us assume for simplicity but without loss of generality that $\mathbf{U}$ is of dimensions 2×2 , and so is $\mathbf{S}$

$$\mathbf{U} = \begin{bmatrix} u_{11} & u_{12} \\ u_{21} & u_{22} \end{bmatrix}, \quad \mathbf{S} = \begin{bmatrix} s_1 & 0 \\ 0 & s_2 \end{bmatrix} \tag{2-80}$$

and that the forcing field consists of only two instantaneous vectors, $\boldsymbol{\psi}^{(0)}$ and $\boldsymbol{\psi}^{(1)}$,

$$\boldsymbol{\psi}^{(0)} = \begin{bmatrix} \psi_1^{(0)} \\ \psi_2^{(0)} \end{bmatrix}, \quad \boldsymbol{\psi}^{(1)} = \begin{bmatrix} \psi_1^{(1)} \\ \psi_2^{(1)} \end{bmatrix} \tag{2-81}$$

[9] http://www.ouranos.ca/

In this simple case,

$$\mathbf{U}*(\mathbf{S}\boldsymbol{\psi}) = \begin{bmatrix} u_{11} & u_{12} & 0 & 0 \\ u_{21} & u_{22} & u_{11} & u_{12} \\ 0 & 0 & u_{21} & u_{22} \end{bmatrix} \begin{bmatrix} s_1\psi_1^{(0)} \\ s_2\psi_2^{(0)} \\ s_1\psi_1^{(1)} \\ s_2\psi_2^{(1)} \end{bmatrix} \tag{2-82}$$

$$= \begin{bmatrix} u_{11} & 0 \\ u_{21} & u_{11} \\ 0 & u_{21} \end{bmatrix} \begin{bmatrix} \psi_1^{(0)} \\ \psi_1^{(1)} \end{bmatrix} s_1 + \begin{bmatrix} u_{12} & 0 \\ u_{22} & u_{12} \\ 0 & u_{22} \end{bmatrix} \begin{bmatrix} \psi_2^{(0)} \\ \psi_2^{(1)} \end{bmatrix} s_2 \tag{2-83}$$

$$= \mathbf{U}_1 * \boldsymbol{\psi}_1\ s_1 + \mathbf{U}_2 * \boldsymbol{\psi}_2\ s_2 \tag{2-84}$$

$$= \begin{bmatrix} \mathbf{U}_1 * \boldsymbol{\psi}_1 & \mathbf{U}_2 * \boldsymbol{\psi}_2 \end{bmatrix} \mathbf{s} \tag{2-85}$$

where $\mathbf{U_1}$ and $\mathbf{U_2}$ stand for the first and second columns of $\mathbf{U}$, $\boldsymbol{\psi}_1$ and $\boldsymbol{\psi}_2$ are defined by

$$\boldsymbol{\psi}_1 = \begin{bmatrix} \psi_1^{(0)} \\ \psi_1^{(1)} \end{bmatrix}, \quad \boldsymbol{\psi}_2 = \begin{bmatrix} \psi_2^{(0)} \\ \psi_2^{(1)} \end{bmatrix}, \quad \mathbf{s} = \begin{bmatrix} s_1 \\ s_2 \end{bmatrix}. \tag{2-86}$$

They are vectors in time whereas those defined in Eq. (2-81)**Error! Reference source not found.** are vectors in space. The same procedure revealed by this simple example can be used to prove the general relationship as of Eq. (2-79) **Error! Reference source not found.** by the mathematical induction method.

Let

$$\mathbf{C} = \begin{bmatrix} \mathbf{U}_1 * \boldsymbol{\psi}_1 & \mathbf{U}_2 * \boldsymbol{\psi}_2 & \cdots & \mathbf{U_m} * \boldsymbol{\psi}_\mathbf{m} \end{bmatrix}, \tag{2-87}$$

which can be fast computed through the convolution theory. According to theory (or called the convolution rule, e.g., Strang 2007), a convolution of two vectors, $\mathbf{f}$ and $\mathbf{g}$, can be computed through FFT and IFFT (fast Fourier transform and its inverse),

$$\mathbf{f} * \mathbf{g} = \mathrm{ifft}(\hat{\mathbf{f}} .* \mathbf{g}) \tag{2-88}$$

where $\hat{\mathbf{f}} = \text{fft}(\mathbf{f})$ and $\mathbf{g} = \text{fft}(\mathbf{g})$, and the operator "dot star, $.*$" means pair wise multiplications. Necessary zeros will have to padded to $\mathbf{f}$ and $\mathbf{g}$ beforehand according to the convolution length rule expressed in Eq. (60) in Part I.

Applying the convolution theory to the column wise convolutions in Eq. (2-74), we can have

$$\mathbf{C} = \text{ifft}(\hat{\mathbf{U}} \ .* \ \hat{\mathbf{\Psi}}) \tag{2-89}$$

where $\hat{\mathbf{U}} = \text{fft}(\mathbf{U})$ and $\hat{\mathbf{\Psi}} = \text{fft}(\mathbf{\Psi})$ and

$$\mathbf{U} = \begin{bmatrix} \mathbf{U_1} & \mathbf{U}_2 & \cdots & \mathbf{U_m} \end{bmatrix} \tag{2-90}$$

$$\mathbf{\Psi} = \begin{bmatrix} \boldsymbol{\psi}_\mathbf{1} & \boldsymbol{\psi}_2 & \cdots & \boldsymbol{\psi}_\mathbf{m} \end{bmatrix} \tag{2-91}$$

The Matlab function, `conv_FFT`, presented below computes the convolution through FFT/IFFT. It takes in two matrices and outputs a matrix too. The output matrix is a columnwise convolution of the two input matrices. However there is an optional logical input, `sumcol`. It is defaulted as *false*. When it is input as *true*, the output matrix will be summed over its columns and the resultant column vector will be output. The two input matrices are named $\mathbf{F}$ and $\mathbf{G}$, which is inherited from `conv_FG` presented in Table 3 of Appendix D in Part I (Section 2.1.11). The function will first validate if the two input matrices have the same number of columns. If not, it will give an error message through lines 9 to 11. Padding rows of zeros to $\mathbf{F}$ and $\mathbf{G}$ according to the convolution length is necessary to prevent unwanted folding back in FFT/IFFT (Strang, 2007) and to make element-wise multiplications possible. Padding zeros is carried out in lines 14 to 18. Two FFTs are performed in lines 21 and 22, and element-wise multiplication of the results of FFTs is performed in line 25. Line 28 performs the summation over the columns if it is intended. Line 32 performs the IFFT of the result before it is output. Note that the summation over the columns should be performed before the IFFT, so that when the summation is indeed carried out, the IFFT only needs to be performed for one column. When the summation over the columns is performed, the output of this function is the same as `conv_FG`.

```
1)    function C=conv_FFT(G, F, sumcol)
2)    % Convolution of two matrices using fft/ifft.
```

```
% The convolution is performed column-wisely and the results is
% output as the C matrix

if nargin<3, sumcol=false; end

size_G=size(G); size_F=size(F);
if size_G(2)~=size_F(2)
   error('G and F must have the same columns!')
end

% padding zeros
p=size_G(1)+size_F(1)-1;          % length of the convolution
Z=zeros(p-size_G(1), size_G(2));
G=[G;Z];
Z=zeros(p-size_F(1), size_F(2));
F=[F;Z];

% fft
G=fft(G);
F=fft(F);

% element-wise multiplications
C=G.*F;

if sumcol
   C=sum(C,2);
end

% inverse fft
C=ifft(C);
```

Table 2-5 Matlab function of conv_FFT

2.2.7 References

Seber, G. A., and Lee, A. J. (2012). Linear regression analysis (Vol. 936). John Wiley & Sons.

Strang, G. (2007). *Computational science and engineering* (pp. 283-288). Wellesley: Wellesley-Cambridge Press.

Strang, G., and Aarikka, K. (1986). *Introduction to applied mathematics* (Vol. 16). Wellesley, MA: Wellesley-Cambridge Press.

Xu Z. (2014) The All-Source Green's Function (ASGF) and its Applications to Storm Surge Modelling. Part I: From the Governing Equations to the ASGF Convolution. Submitted to *Ocean Dynamics*.

Xu Z., Savard J-P and Lefaivre D. (2014) Data Assimilative Hindcast and Climatological Forecast of Storm Surges at Sept-Iles in the Estuary of Gulf of St. Lawrence. Submitted to the *Atmosphere-Ocean*.

2.3 Data Assimilative Hindcast and Climatological Forecast of Storm Surges at Sept-Iles with an ASGF Regression Model

Zhigang Xu[1*], Jean-Pierre Savard[2] and Denis Lefaivre[1]

[1]Maurice Lamontagne Institute
Fisheries and Oceans Canada, Mont-Joli, Quebec

and

Institut des Sciences de la Mer
Université du Québec à Rimouski, Québec

[2]Ouranos Consortium, Montreal, Quebec, Canada

[*]Corresponding Author: zhigang.xu@dfo-mpo.gc.ca

(This section is adapted from a manuscript submitted to Atmosphere-Ocean on 2014/Nov/15 and accepted on 2015/Jan/09 subjected to revisions.)

2.3.1 Abstract

We demonstrate that long term climate model solutions can be very efficiently converted to a value database of future storm surge time series for points of interest (POIs). We use the All-Source Green's Function (ASGF) regression model for the conversion. Not only being data assimilative, the ASGF regression model can also simulate storm surges at a POI millions of times faster than the traditional modelling approach. For the demonstration, we take the tidal gauge at Sept-Iles in the Gulf of St. Lawrence as the POI. We first use the ASGF regression model to assimilate 32 years of the tidal gauge data, producing a continuous hindcast of storm surges and a set of best estimated regression parameters. We then use the ASGF regression model with the best estimated parameters to convert a Canadian Regional Climate Model solution (CRCM/AHJ) to an hourly time series of storm surges from 1961 to 2100. We then apply the Gumbel's extreme value analysis (EVA) to the time series as a whole and tri-decadal piecewise as well. The tri-decadal piecewise approach is intended to investigate if there are any

progressive shortening of storm surge return periods due to future climate change. However, the investigation does not reveal so. We also demonstrate how to correct for bias due to the forcing field at the EVA level.

Keywords: All-Source Green's Function (ASGF), ASGF Regression Model, Storm Surges, Climatological Forcing Field

2.3.2 Introduction

Storm surges are a source of coastal hazards. They are closely related with climate change. How to quantitatively assess impact of climate change on storm surges is a challenge, simply because there is no future water level time series available for statistics. On the other hand, storm containing climate model solutions have recently become more and more available. For example, the Canadian Regional Climate Model[10] has made a suite of solutions available, with a spatial resolution of about 0.4 degree and a temporal resolution of 3-hourly, spanning from 1961 to 2100. It is highly desirable therefore to make a good use of these climate model solutions by converting them *hydrodynamically* to storm surge time series for some points of interest. Such a conversion would usually require running a storm surge model. However a storm surge model can only run at a time step typically in order of seconds, either for the sake of stability or accuracy of solution. It would be hard to run a model for over a hundred years with such a small time step.

However, there is a very efficient tool we can use. Xu (2014a,b) proposed a new method to model storm surges. Without compromising quality of modelling, the new method is millions of times faster than the traditional modelling approach (within the linear dynamics frame). Also the new method is data assimilative, and free of influences of artificial open water boundaries. What supports this tremendous enhancement of modelling efficiency is the All-Source Green's Function (ASGF), which is a pre-calculated matrix to connect a point of interest (POI) and the rest of the world ocean. Once it is calculated, it can be repeatedly used to fast produce the storm surge time series at the POI. It was first proposed to instantaneously predict tsunami arrivals at

[10] http://www.cccma.ec.gc.ca/data/crcm423/crcm423.shtml

some POIs in terms of both time and wave amplitudes (Xu, 2007; 2011; Xu and Song 2013). With an ASGF matrix, a traditional storm surge model can be simplified as a convolution of the matrix with an atmospheric forcing field. Further applied with the singular value decomposition (SVD) and fast Fourier transform and its inverse (fft/ifft), the ASGF convolution can boil down to a simple and very efficient regression model. As reported in Xu (2014b), a simulation of 10 year hourly storm surges at a POI can now be finished in 0.5 seconds!

Because of its tremendously fast speed and its data assimilative capability, the ASGF regression model can provide us a good tool to convert long term climate model solutions to storm surge time series in the future. Obtained time series can serve as a database for further statistics studies. This way, we can feasibly convert an ensemble of climate model solutions to an ensemble of storm surge time series, and thereby we can bring the assessment of the risks due to future storm surges to the same footing as the assessment of future climate changes.

In this paper, we focus on a case study to demonstrate how we can use the ASGF regression model to generate future storm surge time series at a POI and how we can use it statistically. Our procedure consists of two parts: hindcast of past storm surges observed at a POI and forecast of future storm surges at the same place. The hindcast will give us a set of model parameters that are best estimated with the data. The estimated parameters then can be used for the forecast with a climate forcing field. We choose Sept-Iles as our POI, where there are multiple decades of tidal gauge data available for a hindcast.

For the hindcast, we choose MERRA[11] data to provide the forcing field to drive the surge model. The acronym MERRA stands for **M**odern-**E**ra **R**etrospective **A**nalysis for **R**esearch and **A**pplications. It is produced by NASA, and meant to provide the science and applications communities with a state-of-the-art global dataset. It uses the NASA global data assimilation system and a variety of global observing systems. Its temporal resolution is hourly and spatial resolution is 0.50 degrees in latitude and 0.67 degrees in longitude. It spans from 1979 to present and has a global coverage. For the forecast, we choose one of the solutions, the AHJ solution, produced by Canadian Regional Cclimate Model (CRCM)[12] to provide the forcing field (Music and Caya 2007). This forcing field will be referred to as the CRCM/AHJ forcing field hereafter. It has a spatial resolution of about 0.4 degree and a temporal resolution of 3-hourly, spanning a

[11] http://gmao.gsfc.nasa.gov/merra/

[12] http://www.cccma.ec.gc.ca/data/crcm.shtml

period from 1961 to 2100. It is a regional dataset, covering the Arctic, the North American continent and its adjacent seas (see Figure 2-14).

Bernier and Thompson (2006) hindcast storm surges from 1960 to 1999 for the northwest Atlantic sea including the Gulf of St. Lawrence with a non-linear regional model. The forcing field they used is six hourly winds from AES40 dataset (Swail and Cox 2000) and inferred air pressures from the winds. Their modelling approach is traditional, which allows them to have a domain wise solution and to further derive spatial maps of the sizes of storm surges with a definite return period. Such spatial maps are nice since they present the spatial structures of the variables in question.

Our ASGF approach is a POI approach, which is not designed to produce domain wise model solutions and spatial maps derived afterwards. The ASGF method is built upon an assumption that we actually have only a few points, certainly not all the grid points, where model solutions are of interest. The strengths of the ASGF method as mentioned above are all derived from this assumption. Also, the ASGF method works for linear dynamics. However, the linear dynamics often provides the first order approximations. Besides, the data assimilative capability of the method may quite much compensate the missing nonlinearity effects.

2.3.3 The ASGF Regression Model

Starting with a global storm surge model, Xu (2014a) derived the all source Green's function (ASGF) and then used the convolution of the ASGF matrix with a global forcing field to express sea surface elevations at a POI. Applying the singular value decomposition (SVD) and the fast Fourier transform and its inverse (FFT/IFFT) to the ASGF matrix, Xu (2014b) showed that the convolution could further boil down to a very simple linear relation:

$$\boldsymbol{\eta} = \mathbf{Cs} \qquad (2\text{-}92)$$

where $\boldsymbol{\eta}$ is a vector consisting of time series of the sea surface elevations at a POI, $\mathbf{C}$ is a matrix consisting of the columnwise convolutions of the ASGF matrix with an atmospheric forcing field, and $\mathbf{s}$ is a vector of parameters, which are given by the singular values of the ASGF matrix.

Xu (2014b) reported that using Eq. (2-92) to model storm surges at a POI is millions of times faster than the traditional modelling method. Not only does it enhance the modelling speed enormously, Eq. (2-92) also opens an easy way for data assimilation. Simply by admitting an error term, Eq. (2-92) becomes

$$\boldsymbol{\eta} = \mathbf{C}\mathbf{s} + \boldsymbol{\varepsilon} \tag{2-93}$$

where $\boldsymbol{\varepsilon}$ is an error vector consisting of the errors in the observations of the forcing field and of the model itself. The parameter vector $\mathbf{s}$ can now be relaxed from the given values to be determined by the least square fitting between the model and the observations. Xu (2014a, b) derived Eqs. (2-92) and (2-93) in details. Eq. (2-93) will be referred as the ASGF regression model from here on.

Denote $\boldsymbol{\eta}_{\mathrm{o}}$ as the observations, we can estimate $\mathbf{s}$ by minimizing $\boldsymbol{\varepsilon}^{\mathrm{T}}\boldsymbol{\varepsilon}$ (the so-called least square fitting technique). The estimated parameter vector, $\hat{\mathbf{s}}$, is

$$\hat{\mathbf{s}} = (\mathbf{C}^{\mathrm{T}}\mathbf{C})^{-1}\mathbf{C}^{\mathrm{T}}\boldsymbol{\eta}_{\mathrm{o}} \tag{2-94}$$

(e.g., Strang, 1986; Strang 2007; Seber and Lee 2003). The observation data are assimilated into the model parameter vector $\hat{\mathbf{s}}$. The least square fitted solution, $\hat{\boldsymbol{\eta}}$, or to say, the data assimilative model solution, is given by

$$\hat{\boldsymbol{\eta}} = \mathbf{C}\,\hat{\mathbf{s}}. \tag{2-95}$$

Solution given by Eq. (2-92) is non-data assimilative whereas the one given by Eq. (2-95) is data assimilative. Figure 2-11, adapted from Xu (2014b), compares both types of solutions against the same observations, which are the de-tided sea surface elevations. The top panel is the comparison for the non-data assimilative solution and the bottom panel shows the comparison for the data assimilative solution. As we can see, the non-data assimilative solution agrees with the observations well whereas the assimilative simulations perform even better. The γ^2 indicated in the titles of the panels measures the overall misfits between the simulations and the observations. It is defined as

$$\gamma^2 = \frac{\text{sum of squares of misfits}}{\text{sum of squares of observations}} \quad . \qquad (2\text{-}96)$$

The smaller this value is, the better the fit between the simulations and the observations. The γ^2 value for the non-assimilative solutions is 0.18, which means that 82% of the observed variance is explained by the solutions. The γ^2 value for the assimilative solutions is 0.05; in other words, 95% of the observed variance is explained by the assimilative solutions. Thus, Figure 2-11 well illustrates the power of the ASGF regression model. We will use it for a long term hindcast and forecast.

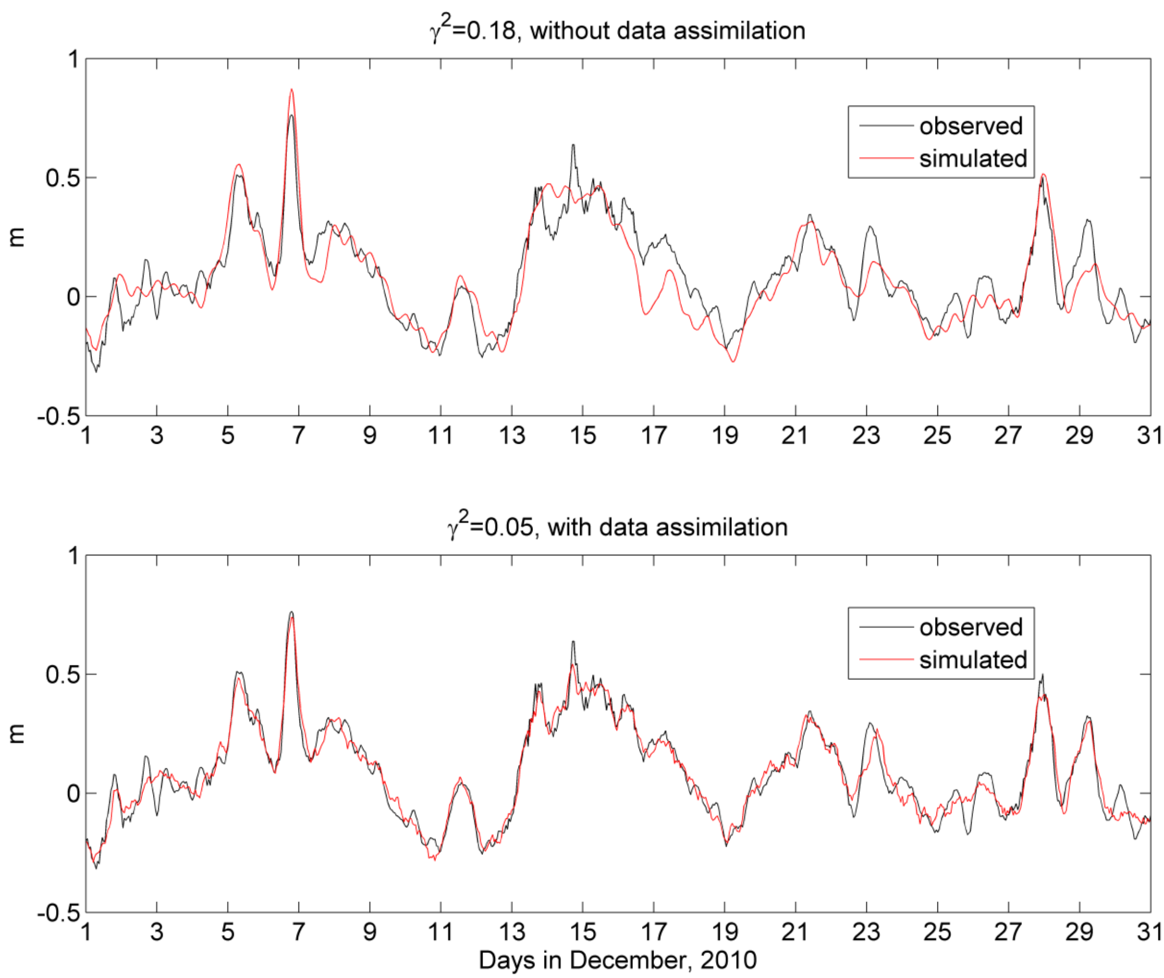

Figure 2-11. Comparisons of non-data assimilative solution (top) and data assimilative solution (bottom) with the observations with the observations at Sept-Iles. The observations are sea surface elevations after removal of tides. The γ^2 values indicated in the panel titles are the ratios of the

misfit variance over the observed variance. The smaller this value is, the better the agreement is between the simulations and the observations (after Xu 2014b).

2.3.4 Data Assimilative Hindcast with the MERRA Forcing Field

The forcing field used for the short term test case shown above is the MERRA data. We will use this forcing field also for the long term hindcast. This forcing dataset is preferable because it is highly realistic and has hourly temporal resolution (which is high compared with other similar products). It also covers the entire globe, which suits the ASGF approach. At any hour, the MERRA forcing field gives a vector of 408,622 elements consisting of the points of air pressures and wind stresses over the global ocean. Shown in Figure 2-12 are the results of the hindcast of storm surges at Sept-Iles in three different ways. The simulations are shown in red, and the observations are shown in black. The period of the hindcast is from 1979/07/30 to 2011/12/31.

The top panel of the figure shows the simulations without data assimilation. Shown in the middle panel are the data assimilative simulations with all the data weighted equally. The third panel shows the results from the weighted least square fitting, with the surge data weighted ten times more than the non-surge data. The surge data are those that are outside the yellow band (outside of $\pm 35cm$). They are more likely caused by storms in the air than those within; not all de-tided signals can be attributed to atmospheric forcing. There are 240,903 hourly points in the observations, of which 9,318 points are outside the yellow band. For simplicity in wording only, we refer to those outside the yellow band as surge data or simply surges, and refer to those within the band as non-surge data.

The misfit measurement γ^2 is indicated in each panel with two values, the first value is for all the misfits whereas the second one is for the misfits of the surge data. The first value of γ^2 indicated in the top panel is 0.38 whereas the second value is 0.12. This means that the simulations and the observations agree much better for the surge data than for all the data. The middle panel of the figure shows the results of data assimilation where all the data points are weighted equally. The data assimilation improves the fit, but the improvement is mostly absorbed by the majority of the non-surge data; the first value of γ^2 is dropped from 0.38 to 0.32 whereas the second value remains the same to the second decimal place. We wish to improve

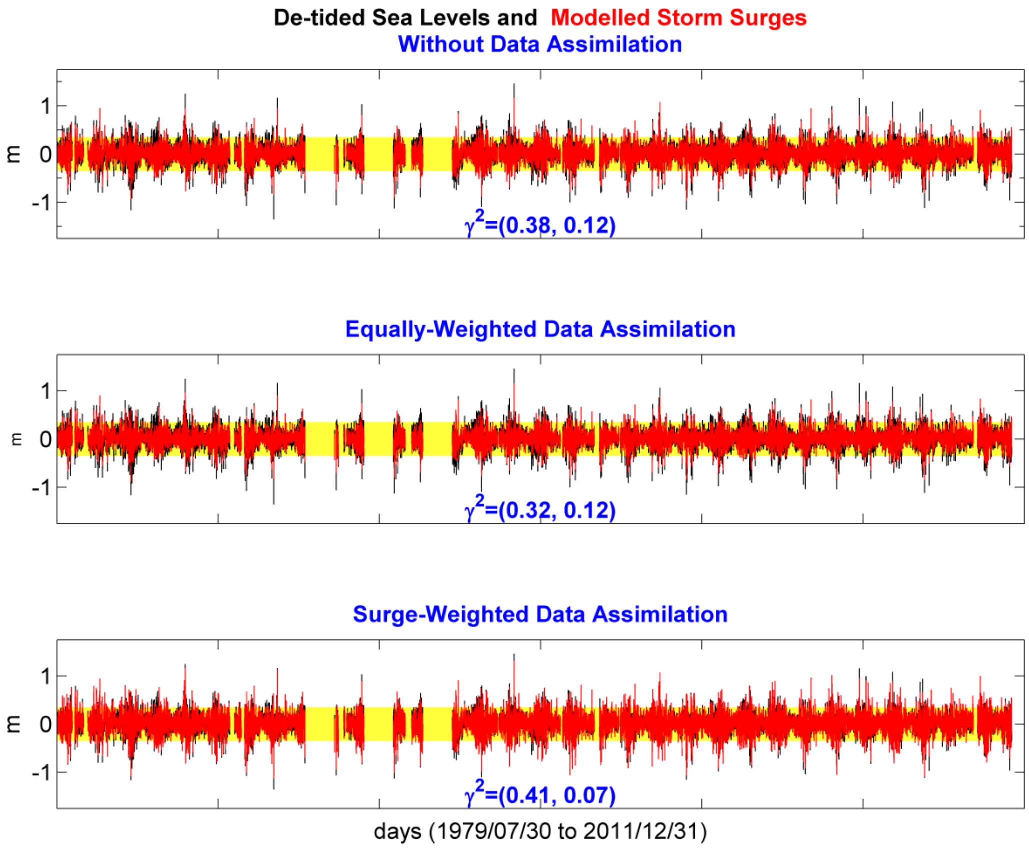

Figure 2-12. Long term simulations of storm surges without data assimilation (top), with equally weight data assimilation (middle) and with surge-weighted data assimilation (bottom). The simulations are shown in red and the observations are shown in black with data gaps. The data outside the yellow band are larger than 35cm in their absolute values, and are referred to as surge data. The simulations are continuous but are not shown at the data gaps.

the fit particularly for the surges, whereas the ordinary oscillations are not much of our concern. Thus, we exercised a weighted least square fitting, by replacing the matrix $\mathbf{C}$ with $\mathbf{WC}$ where $\mathbf{W}$ is a diagonal matrix to weight the surge data 10 times more than the non-surge data. The result of this surge-weighted data assimilation is shown in the third panel. The agreement between the simulations and the surge data is improved significantly. The γ^2 value is dropped from 0.12 down to 0.07. The improvement comes at the cost of increase of the γ^2 for all the misfits, the majority (96%) of which are of the non-surge data. This is a trade-off that we can accept since we care much more for the surge data than for the non-surge data.

What if we reserve half of the data from the data assimilation? Can the model be trained with the first half of data to well predict for the next half? Figure 2-13 shows the results of this investigation. The first half of the observations (about 16 years of hourly data) is assimilated with the weighting scheme mentioned above. The red curve is for the assimilative simulations, with a black curve behind for the observations. The green curve is the predictions for the second half period (about 16 years of hourly data too) by the model trained with only the first half of the observations. The γ^2 value for the data assimilation half is 0.08 and that for the prediction half is 0.07, both are satisfactory. Shown in the middle and bottom panels of the figure are two zoomed views of the assimilation half and of the prediction half respectively. The results of this investigation are encouraging. It makes sense to use the trained surge model to predict the future surges with some climate model solutions as the forcing fields.

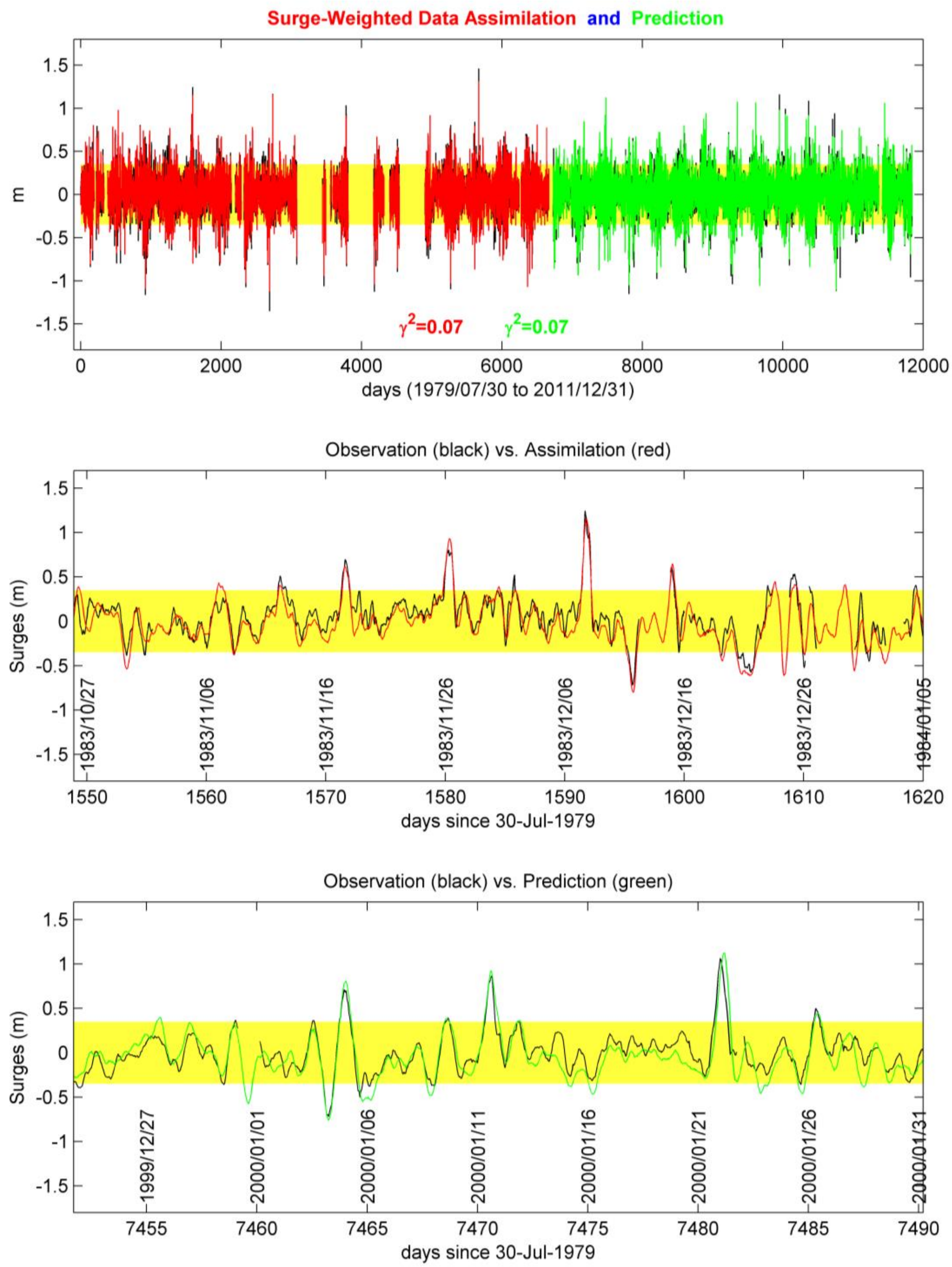

Figure 2-13. Top panel: half data assimilation and half predictions: the assimilative solution is shown in red and the prediction is shown in green against the observations in black. The misfit measurements for the assimilation and for the prediction are shown by the γ^2 values in red and in green respectively. Middle and bottom panels: two zoom views of the top panel.

2.3.5 Climatological Forecast of Storm Surges with CRCM/AHJ Forcing Field

By climatological forecast, we mean to produce storm surges for the future with climate model solutions as a forcing field. The climate is a stochastic process. Solutions output by a climate model run are just one of many possible realizations of the stochastic process. Climate model solutions are not constrained by observations even though the model run starts from the past. We should not expect a one-to-one correspondence between the climate model solutions and the real events in the past therefore. The storm surges driven by the climate model solutions will be stochastic too. They should not be expected to correspond to the past real events either. The value of having stochastic storm surges is that they can provide a basis for statistics. The more stochastic storm surges we can produce, the more robust statistics we can draw.

For this study, we will use the CRCM/AHJ climate model solution to provide a forcing field. The CRMC/AHJ is a regional climate model solution. Its regional coverage is outlined in Figure 2-14. Its three hourly forcing field will be interpolated to hourly since the All-Source Green's Function (the matrix $\mathbf{G}$ in Eq. 2-104) is hourly. The forcing field spans from 1961/Jan/01 00:00:00 to 2100/Nov/30 21:00:00. There are almost 140 years of hourly storm surges to generate. With the ASGF method, it takes less than 8 seconds to generate it on a PC.

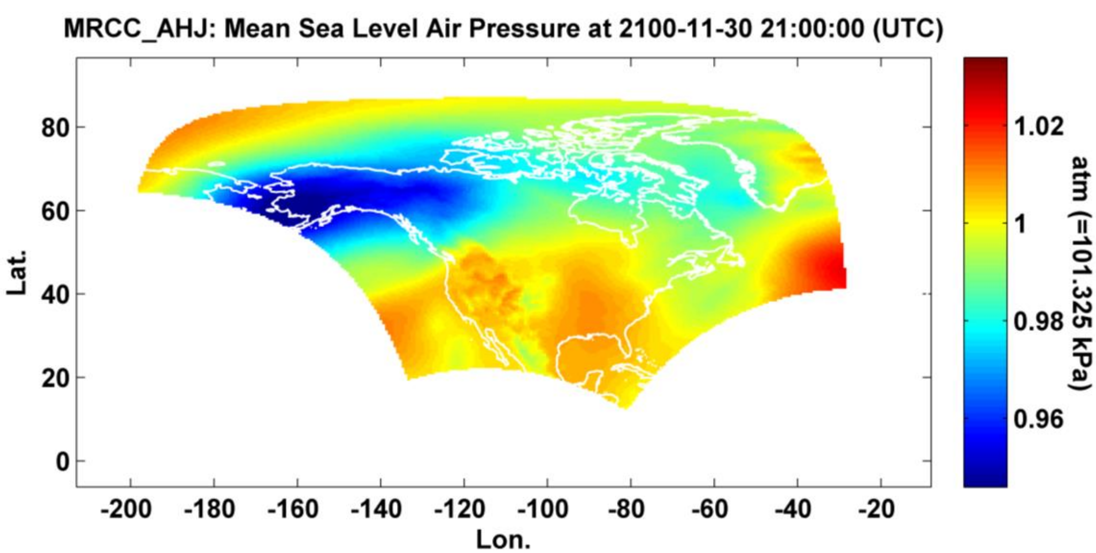

Figure 2-14 The CRCM/AHJ is a regional climate model solution. Shown above is a snapshot the mean sea level air pressures at 2100/Nov/30 21:00:00 UTC.

To calculate storm surges for the future, we use Eq. (2-92) with the matrix $\mathbf{C}$ calculated with the CRCM/AHJ forcing field (cf. Eq. 2-74) and with the $\mathbf{s}$ replaced by the $\hat{\mathbf{s}}$ obtained from the surge-weighted assimilation of the 32 years observations (cf. the third panel of Figure 2-12). The forcing field is regional where the ASGF matrix is prepared for the global ocean. This means we have to assign zero values for the forcing field outside of the regional domain. We also subtract a standard air pressure (101.325kPa) from the air pressure within the regional domain to avoid a huge imbalance of the air pressures within the domain and outside. To subtract a constant value from the air pressure field will not change the surge dynamics at all.

Shown in the bottom panel of Figure 2-15 is the time series of the storm surges driven by CRCM/AHJ. For reference, we have also shown the observations and realistic simulations with the MERRA forcing field in the same time line in the top and the middle panels respectively. From the figure, we may see that the CRCM/AHJ driven storm surges are much stronger than the realistic ones, if we can compare the bottom panel with the top panel or middle panel for the same period. This indicates the CRCM/AHJ forcing is too strong and will result in a systematic bias in the simulated storm surges. We will correct this bias in the next section.

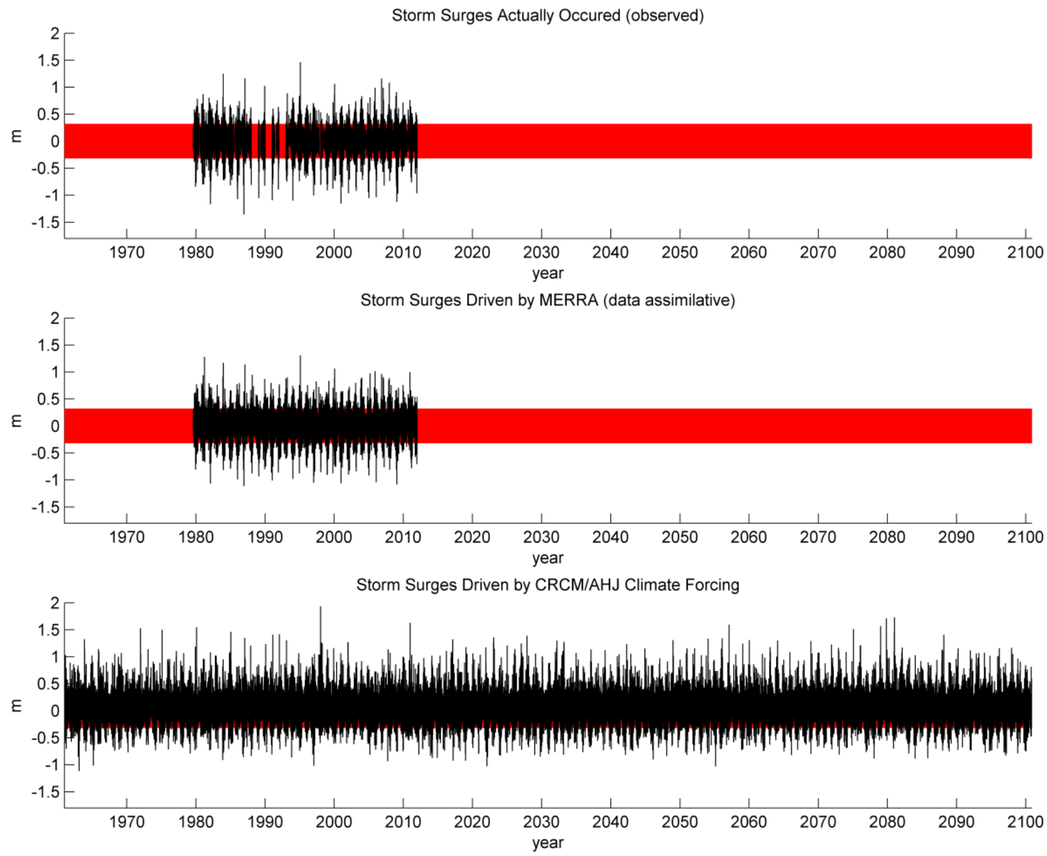

Figure 2-15 Time series of storm surges at Sept-Iles. The top panel is observed, the middle panel is driven by MERRA force field and the bottom panel is driven by CRMC/AHJ forcing field. The data points outside the red band are larger than 35cm in absolute values.

2.3.6 Extreme Value Analysis of the Future Storm Surges

The time series as shown in the bottom panel of Figure 2-15 should have some statistical values. One may explore them in many ways. The statistics we are going to explore in this section is to apply the Gumbel's extreme value analysis (EVA) to the simulated time series. According to Gumbel (1954, 1958), the return periods of the annual maxima of the storm surges should obey a straight line distribution on a double-logarithm scale. Shown on the left panel of Figure 2-16 are such straights lines, along with the experimental data and confidence zones, in black and blue colors respectively for the observed and simulated annual maxima from 1979 to 2011.

As we can see, the EVA results in blue show a systematic bias from those in black. This means that the CRCM/AHJ forcing field is too strong compared to the reality. We need to correct for this bias. The correction can be done by first finding out the difference in the slopes and in the intercepts between the blue and black lines. We can then adjust the line, the data points, and the confidence zone in blue by applying the differences. Shown on the right panel of the figure are the results after the correction. As we can expect, the line and the confidence zone in blue are now coincident with those in black. The two sets of the data points are not necessary coincident one to another, but they all distribute along the straight lines.

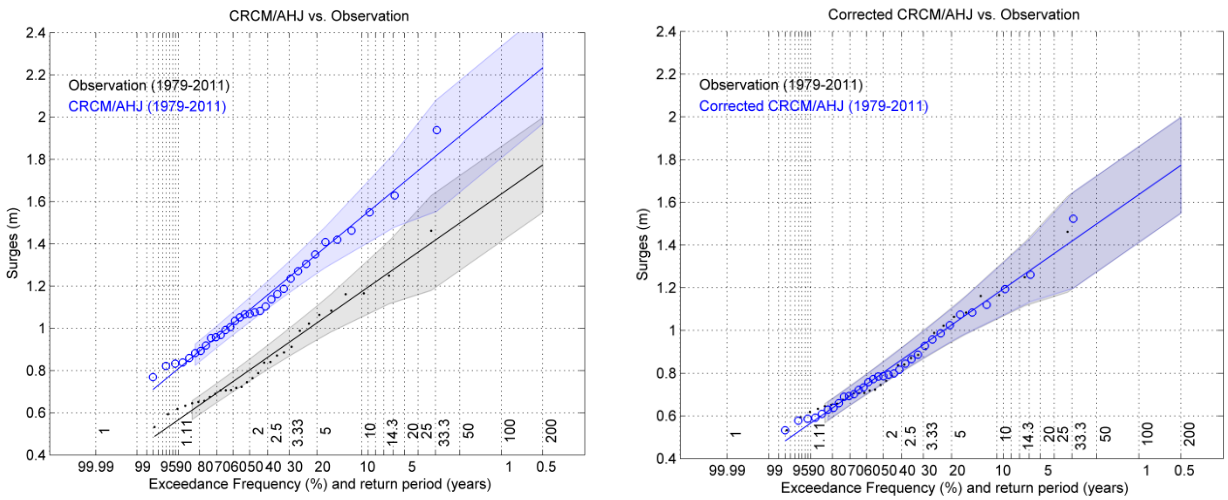

Figure 2-16. On the left: the EVA results from the simulated annual maxima (blue) and from the observed annual maxima (black). The dots are the experiment data, and the straight lines are the least square fitted lines. The shaded zones are 67% confidence zones. The results in blue are systematically biased from those in black. On the right: the data and lines in blue are corrected for the biases.

Shown in Figure 2-17 are the results from applying the EVA to the 140 year hourly time series as whole after the correction for the CMCR/AHJ forcing bias. An obvious benefit from having such a long time series is that the Gumbel's line is constrained by more data points, especially at the top end. There are data points beyond 32 years return period to control the line. Consequently, the confidence zone in light blue becomes somewhat narrower than that in gray. Another feature may be worthy to note is that the straight line in blue is less steep than the line in black. The two lines intersect at about at the coordinates of (5, 1), which means that the model simulation gives longer return period than the observation for storm surges larger than 1m. However their associated confidence zones still overlap each other.

Shown in Figure 2-18 are results of applying EVA to tri-decadal pieces of the time series from 2012 to 2100. Shown on the left panels are the results without the correction for the CRCM/AHJ bias whereas on the right panels are the results with the correction. The EVA results from the past observation (1979-2011) are superimposed on each panel for comparison. This tri-decadal piecewise approach attempts to investigate if there is a progressive shortening in the return periods of storm surges, which is what we may all be concerned with the impact of climate change. However, by comparing the blues against the blacks on the right panels, we do not see a progressive shortening of the return periods for the same sizes of the storm surges. The bottom right panel of Figure 2-18 for the period of 2073-2100 shows almost the same picture as the panel on the right of Figure 2-16 for the period of 1979-2011.

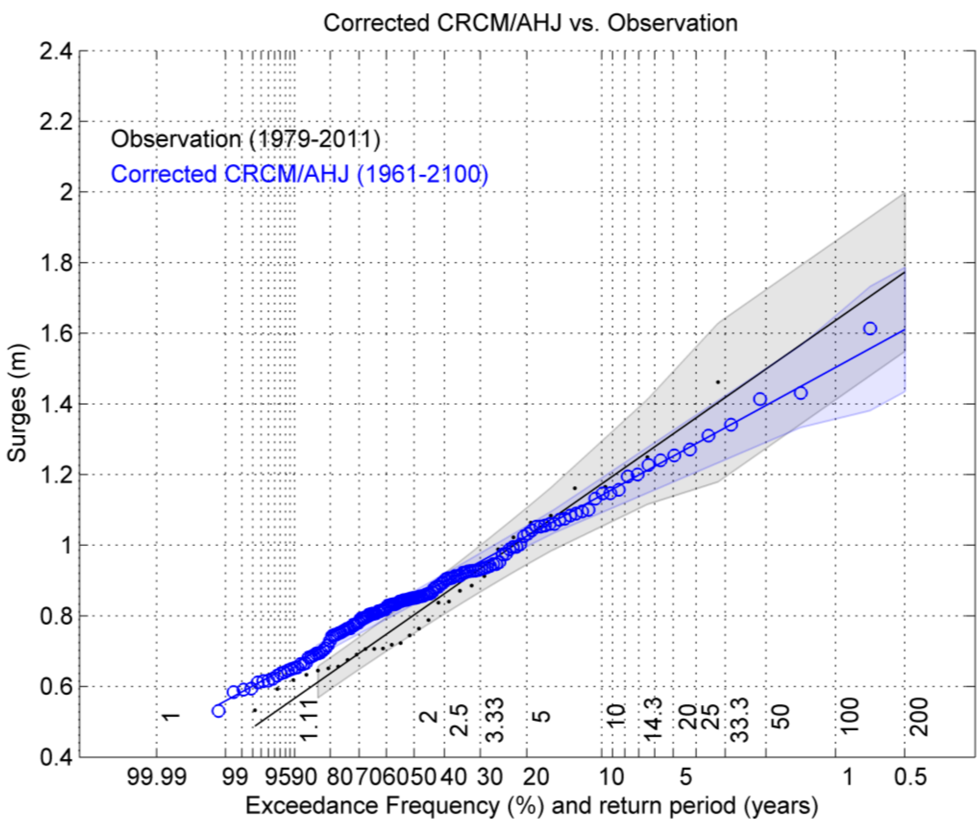

Figure 2-17 Shown in blue are the simulated annual maxima from 1961 to 2100 and the best fitted Gumbel's straight line and associated 67% confidence zone. Shown in black are the counterparts from the observed annual maxima from 1979-2011.

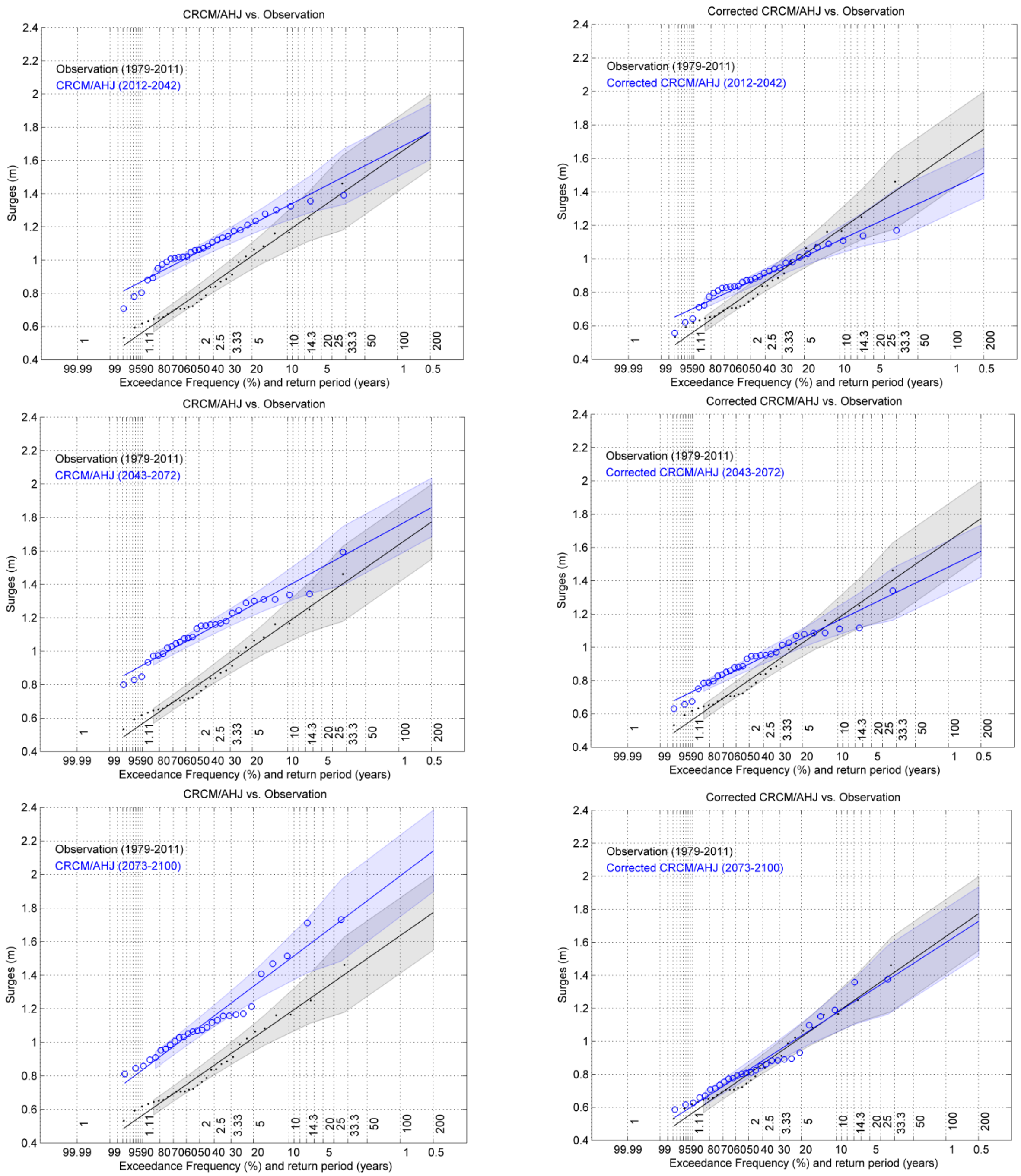

Figure 2-18 Results of EVA applied tri-decadal pieces of the CRCM/AHJ driven storm surges.

2.3.7 Summary and Discussions

We have demonstrated that the ASGF regression model can be used as a very efficient tool to hydrodynamically convert the available climate model solutions to a database of future storm surges. The ASGF regression model is derived from a traditional storm surge model but can produce simulations millions of times faster than the latter. It can easily assimilate observed data into simulations. Weighted data assimilations can be also easily exercised.

For the demonstration, we used the ASGF regression model derived for Sept-Iles to first assimilate 32 years (1979-2011) of detided data with large data (>0.35m) weighted more than smaller ones. The large data are more likely driven by the storms in the air than the smaller ones. The data assimilation produces a continuous hindcast of storm surges at Sept-Iles. It also yields the best estimated regression model parameters, which can be used for a climatological prediction into the future. For the climatological prediction, we used the CRCM/AHJ climate model solution to provide a forcing field from 1961 to 2100. With the best estimated regression parameters and with the CRCM/AHJ forcing field, the ASGF regression model produces a 140 year hourly time series of storm surges in a few seconds.

The produced time series can be used for further statistical studies. We subjected the time series to the Gumbel's EVA. The simulated time series has a portion that is overlapped by the observation time series (see Figure 2-15). This makes possible to see if the simulation driven by CRCM/AHJ is statistically biased from the reality. We indeed found that there is a bias and corrected for it (see Figure 2-16 and Figure 2-18). We applied the EVA to the 140 year long time series as a whole as well as to its tri-decadal pieces. The tri-decadal approach is an attempt to investigate if there is any progressive shortening of the return periods of the storm surges. However the investigation does not reveal so.

We do not wish to interpret the above EVA results as a general conclusion here, since they are based on only one of many possible climate forcing fields. The main point of this study is to demonstrate that the ASGF regression model as of Eq. (2-93) can be used as a very efficient tool to convert a long term climate model solution to the same length of storm surge time series at a POI. The procedure shown by the demonstration can be repeated for other POIs and with other climate forcing fields. As more climate model solutions are collected for this purpose, the larger database of future storm surges we can establish, and more robust statistics can be drawn upon. In fact, a project is currently underway to apply the same procedure to the permanent tidal gauges operated by the Canadian Hydrographic Service.

2.3.8 Acknowledgement

This study was partially supported by le Ministère des Transports du Québec, and by the ACCASP program of Fisheries and Oceans Canada. The free accesses to the MERRA and CRCM/AHJ data made available by NASA and Ouranos respectively are also greatly appreciated. The authors would also like to acknowledge the supports from our institutes. Our thanks also go to Mr. Michel Beaulieu for his assistantship.

2.3.9 References

Bernier, N. B., & Thompson, K. R. (2006). Predicting the frequency of storm surges and extreme sea levels in the northwest Atlantic. *Journal of Geophysical Research: Oceans (1978–2012)*, *111*(C10).

Gumbel, E. J., & Lieblein, J. (1954). *Statistical theory of extreme values and some practical applications: a series of lectures* (Vol. 33). Washington: US Government Printing Office.

Gumbel, E. J. (1958). Statistics of extremes, 1958. *Columbia Univ. press, New York*.

Music, B., & Caya, D. (2007). Evaluation of the hydrological cycle over the Mississippi River basin as simulated by the Canadian Regional Climate Model (CRCM). *Journal of Hydrometeorology*, *8*(5), 969-988.

Seber, G. A., and Lee, A. J. (2003). Linear regression analysis. Hoboken.

Strang, G. (2007). *Computational science and engineering* (pp. 283-288). Wellesley: Wellesley-Cambridge Press.

Strang, G., and Aarikka, K. (1986). *Introduction to applied mathematics* (Vol. 16). Wellesley, MA: Wellesley-Cambridge Press.

Swail, V. R., and A. T. Cox (2000), On the use of NCEP-NCAR reanalysis surface marine wind fields for a long-term North Atlantic wave hindcast, J. Atmos. Ocean Tech., 17, 532–545.

Xu, Z. (2007). The all-source Green's function and its applications to tsunami problems. *Science of Tsunami Hazards*, *26*(1), 59.

Xu, Z. (2011). The all-source Green's function of linear shallow water dynamic system: Its numerical constructions and applications to tsunami problems. *The Tsunami Threat-Research and Technology*, *25*.

Xu Z. (2014a) The All-Source Green's Function (ASGF) and its Applications to Storm Surge Modelling. Part I: From the Governing Equations to the ASGF Convolution. Submitted to *Ocean Dynamics*.

Xu Z. (2014b) The All-Source Green's Function (ASGF) and its Applications to Storm Surge Modelling. Part II: From the ASGF Convolution to Forcing Data Compression and to A Regression Model. Submitted to *Ocean Dynamics*.

Xu, Z., and Song, Y. T. (2013). Combining the All-Source Green's Functions and the GPS-Derived Source Functions for Fast Tsunami Predictions—Illustrated by the March 2011 Japan Tsunami. *Journal of Atmospheric and Oceanic Technology*, *30*(7), 1542-1554.